

1 A search for sparticles in zero lepton final states

2 Russell W. Smith

3 Submitted in partial fulfillment of the

4 requirements for the degree of

5 Doctor of Philosophy

6 in the Graduate School of Arts and Sciences

7 COLUMBIA UNIVERSITY

8 2016

9

© 2016

10

Russell W. Smith

11

All rights reserved

12

## ABSTRACT

13

A search for sparticles in zero lepton final states

14

Russell W. Smith

15 TODO : Here's where your abstract will eventually go. The above text is all in the  
16 center, but the abstract itself should be written as a regular paragraph on the page,  
17 and it should not have indentation. Just replace this text.



---

*Contents*

19	<b>Contents</b>	i
20	<b>1 Introduction</b>	1
21	<b>2 The Standard Model</b>	5
22	2.1 Overview	5
23	2.2 Field Content	6
24	2.3 Deficiencies of the Standard Model	15
25	<b>3 Supersymmetry</b>	21
26	3.1 Supersymmetric theories : from space to superspace	21
27	3.2 Minimally Supersymmetric Standard Model	24
28	3.3 Phenomenology	30
29	3.4 How SUSY solves the problems with the SM	33
30	3.5 Conclusions	35
31	<b>4 The Large Hadron Collider</b>	37
32	4.1 Basics of Accelerator Physics	37
33	4.2 Accelerator Complex	39
34	4.3 Large Hadron Collider	41
35	4.4 Dataset Delivered by the LHC	43
36	<b>5 The ATLAS detector</b>	49

37	5.1	Magnets	50
38	5.2	Inner Detector	52
39	5.3	Calorimetry	56
40	5.4	Muon Spectrometer	61
41	5.5	Trigger System	66
42	<b>6</b>	<b>Object Reconstruction</b>	<b>73</b>
43	6.1	Primitive Object Reconstruction	73
44	6.2	Physics Object Reconstruction and Quality Identification	79
45	<b>7</b>	<b>Recursive Jigsaw Reconstruction</b>	<b>105</b>
46	7.1	Razor variables	105
47	7.2	SuperRazor variables	105
48	7.3	Recursive Jigsaw Reconstruction	105
49	7.4	Variables used in the search for zero lepton SUSY	106
50	<b>8</b>	<b>Table of Contents Title</b>	<b>107</b>
51	<b>9</b>	<b>A search for supersymmetric particles in zero lepton final states with the Recursive Jigsaw Technique</b>	<b>109</b>
53	9.1	Object reconstruction	109
54	9.2	Signal regions	110
55	9.3	Background estimation	110
56	<b>10</b>	<b>Results</b>	<b>111</b>
57	10.1	Statistical Analysis	111
58	10.2	Signal Region distributions	111
59	10.3	Pull Plots	111
60	10.4	Systematic Uncertainties	111
61	10.5	Exclusion plots	111

62	<b>Conclusion</b>	<b>113</b>
63	10.6 New Section	113
64	<b>Bibliography</b>	<b>115</b>
65	<b>Quantum Field Theory and Symmetries</b>	<b>125</b>
66	Quantum Field Theory	125
67	Symmetries	126
68	Local symmetries	128



---

*Acknowledgements*



---

*Dedication*



71

## Chapter 1

---

72

### *Introduction*

73 Particle physics is a remarkably successful field of scientific inquiry. The ability to  
 74 precisely predict the properties of a exceedingly wide range of physical phenomena,  
 75 such as the description of the cosmic microwave background [1, 2], the understanding  
 76 of the anomalous magnetic dipole moment of the electron [3, 4], and the measurement  
 77 of the number of weakly-interacting neutrino flavors [5] is truly amazing.

78 The theory that has allowed this range of predictions is the *Standard Model*  
 79 of particle physics (SM). The Standard Model combines the electroweak theory of  
 80 Glashow, Weinberg, and Salam [6–8] with the theory of the strong interactions, as  
 81 first envisioned by Gell-Mann and Zweig [9, 10]. This quantum field theory (QFT)  
 82 contains a tiny number of particles, whose interactions describe phenomena up to at  
 83 least the TeV scale. These particles are manifestations of the fields of the Standard  
 84 Model, after application of the Higgs Mechanism. The particle content of the SM  
 85 consists only of the six quarks, the six leptons, the four gauge bosons, and the scalar  
 86 Higgs boson.

87 Despite its impressive range of described phenomena, the Standard Model has  
 88 some theoretical and experimental deficiencies. The SM contains 26 free parameters  
 89 <sup>1</sup>. It would be more theoretically pleasing to understand these free parameters in  
 90 terms of a more fundamental theory. The major theoretical concern of the Standard  
 91 Model, as it pertains to this thesis, is the *hierarchy problem*[11–15]. The light mass

---

<sup>1</sup>This is the Standard Model corrected to include neutrino masses. These parameters are the fermion masses (6 leptons, 6 quarks), CKM and PMNS mixing angles (8 angles, 2 CP-violating phases), W/Z/Higgs masses (3), the Higgs field expectation value, and the couplings of the strong, weak, and electromagnetic forces (3  $\alpha_{force}$  ).

of the Higgs boson (125 GeV) should be quadratically dependent on the scale of UV physics, due to the quantum corrections from high-energy physics processes. The most perplexing experimental issue is the existence of *dark matter*, as demonstrated by galactic rotation curves [16–22]. This data has shown that there exists additional matter which has not yet been seen interacting with the particles of the Standard Model. There is no particle in the SM which can act as a candidate for dark matter.

Both of these major issues, as well as numerous others, can be solved by the introduction of *supersymmetry* (SUSY) [15, 23–35]. In supersymmetric theories, each SM particles has a so-called *superpartner*, or sparticle partner, differing from given SM particle by 1/2 in spin. These theories solve the hierarchy problem, since the quantum corrections induced from the superpartners exactly cancel those induced by the SM particles. In addition, these theories are usually constructed assuming *R*–parity, which can be thought of as the “charge” of supersymmetry, with SM particles having  $R = 1$  and sparticles having  $R = -1$ . In collider experiments, since the incoming SM particles have total  $R = 1$ , the resulting sparticles are produced in pairs. This produces a rich phenomenology, which is characterized by significant hadronic activity and large missing transverse energy ( $E_T^{\text{miss}}$ ), which provide significant discrimination against SM backgrounds [36].

Despite the power of searches for supersymmetry where  $E_T^{\text{miss}}$  is a primary discriminating variable, there has been significant interest in the use of other variables to discriminate against SM backgrounds. These include searches employing variables such as  $\alpha T$ ,  $M_{T,2}$ , and the razor variables ( $M_R, R^2$ ) [37–47]. In this thesis, we will present the first search for supersymmetry using the novel Recursive Jigsaw Reconstruction (RJR) technique. RJR can be considered the conceptual successor of the razor variables. We impose a particular final state “decay tree” on an events, which roughly corresponds to a simplified Feynmann diagram in decays containing weakly-interacting particles. We account for the missing degrees of freedom associated

119 to the weakly-interacting particles by a series of simplifying assumptions, which allow  
120 us to calculate our variables of interest at each step in the decay tree. This allows an  
121 unprecedented understanding of the internal structure of the decay and the ability to  
122 construct additional variables to reject Standard Model backgrounds.

123 This thesis details a search for the superpartners of the gluon and quarks, the  
124 gluino and squarks, in final states with zero leptons, with  $13.3 \text{ fb}^{-1}$  of data using the  
125 ATLAS detector. We organize the thesis as follows. The theoretical foundations of  
126 the Standard Model and supersymmetry are described in Chapters 2 and 3. The  
127 Large Hadron Collider and the ATLAS detector are presented in Chapters 4 and 5.  
128 Chapter 5 provides a detailed description of Recursive Jigsaw Reconstruction and a  
129 description of the variables used for the particular search presented in this thesis.  
130 Chapter 6 presents the details of the analysis, including details of the dataset, object  
131 reconstruction, and selections used. In Chapter 7, the final results are presented;  
132 since there is no evidence of a supersymmetric signal in the analysis, we present the  
133 final exclusion curves in simplified supersymmetric models.



134

## Chapter 2

---

135

### *The Standard Model*

## 136 2.1 Overview

137 A Standard Model is another name for a theory of the internal symmetry group  
138  $SU(3)_C \otimes SU(2)_L \otimes U(1)_Y$ , with its associated set of parameters. 139 The Standard  
140 Model refers specifically to a Standard Model with the proper parameters to describe  
141 the universe. The SM is the culmination of years of work in both theoretical and  
142 experimental particle physics. 143 **TODO: cite** In this thesis, we take the view that  
144 theorists construct a model with the field content and symmetries as inputs, and  
145 write down the most general Lagrangian consistent with those symmetries. Assuming  
146 this model is compatible with nature (in particular, the predictions of the model are  
147 consistent with previous experiments), experimentalists are responsible measuring the  
parameters of this model. This will be applicable for this chapter and the following  
one.

148 Additional theoretical background is in [10.6](#). The philosophy and notations are  
149 inspired by [\[48, 49\]](#).

<sub>150</sub> **2.2 Field Content**

The Standard Model field content is

$$\begin{aligned} \text{Fermions} &: Q_L(3, 2)_{+1/3}, U_R(3, 1)_{+4/3}, D_R(3, 1)_{-2/3}, L_L(1, 2)_{-1}, E_R(1, 1)_{-2} \\ \text{Scalar (Higgs)} &: \phi(1, 2)_{+1} \\ \text{Vector Fields} &: G^\mu(8, 1)_0, W^\mu(1, 3)_0, B^\mu(1, 1)_0 \end{aligned} \tag{2.1}$$

<sub>151</sub> where the  $(A, B)_Y$  notation represents the irreducible representation under  $SU(3)$   
<sub>152</sub> and  $SU(2)$ , with  $Y$  being the electroweak hypercharge. Each of these fermion fields  
<sub>153</sub> has an additional index, representing the three generation of fermions.

<sub>154</sub> We observed that  $Q_L$ ,  $U_R$ , and  $D_R$  are triplets under  $SU(3)_C$ ; these are the *quark*  
<sub>155</sub> fields. The *color* group,  $SU(3)_C$  is mediated by the *gluon* field  $G^\mu(8, 1)_0$ , which has  
<sub>156</sub> 8 degrees of freedom. The fermion fields  $L_L(1, 2)_{-1}$  and  $E_R(1, 1)_{-2}$  are singlets under  
<sub>157</sub>  $SU(3)_C$ ; we call them the *lepton* fields.

<sub>158</sub> Next, we note the “left-handed” (“right-handed”) fermion fields, denoted by  $L$  ( $R$ )  
<sub>159</sub> subscript, The left-handed fields form doublets under  $SU(2)_L$ . These are mediated  
<sub>160</sub> by the three degrees of freedom of the “W” fields  $W^\mu(1, 3)_0$ . These fields only act  
<sub>161</sub> on the left-handed particles of the Standard Model. This is the reflection of the  
<sub>162</sub> “chirality” of the Standard Model; the left-handed and right-handed particles are  
<sub>163</sub> treated differently by the electroweak forces. The right-handed fields,  $U_R$ ,  $D_R$ , and  
<sub>164</sub>  $E_R$ , are singlets under  $SU(2)_L$ .

<sub>165</sub> The  $U(1)_Y$  symmetry is associated to the  $B^\mu(1, 1)_0$  boson with one degree of  
<sub>166</sub> freedom. The charge  $Y$  is known as the electroweak hypercharge.

<sub>167</sub> To better understand the phenomenology of the Standard Model, let us investigate  
<sub>168</sub> each of the *sectors* of the Standard Model separately.

169 **Electroweak sector**

The electroweak sector refers to the  $SU(2)_L \otimes U(1)_Y$  portion of the Standard Model gauge group. Following our philosophy of writing all gauge-invariant and renormalizable terms, the electroweak Lagrangian can be written as

$$\mathcal{L} = W_a^{\mu\nu}W_a^\mu + B^{\mu\nu}B_{\mu\nu} + (D^\mu\phi)^\dagger D_\mu\phi - \mu^2\phi^\dagger\phi - \lambda(\phi^\dagger\phi)^2. \quad (2.2)$$

where  $W_a^{\mu\nu}$  are the three ( $a = 1, 2, 3$ ) gauge bosons associated to the  $SU(2)_L$  gauge group,  $B^{\mu\nu}$  is the one gauge boson of the  $U(1)_Y$  gauge group, and  $\phi$  is the complex Higgs multiplet. The covariant derivative  $D^\mu$  is given by

$$D^\mu = \partial^\mu + \frac{ig}{2}W_a^\mu\sigma_a + \frac{ig'}{2}B^\mu \quad (2.3)$$

where  $i\sigma_a$  are the Pauli matrices times the imaginary constant, which are the generators for  $SU(2)_L$ , and  $g$  and  $g'$  are the  $SU(2)_L$  and  $U(1)_Y$  coupling constants, respectively. The field strength tensors  $W_a^{\mu\nu}$  and  $B^{\mu\nu}$  are given by the commutator of the covariant derivative associated to each field

$$B^{\mu\nu} = \partial^\mu B^\nu - \partial^\nu B^\mu \quad (2.4)$$

$$W_a^{\mu\nu} = \partial^\mu W_a^\nu - \partial^\nu W_a^\mu - g\epsilon_{abc}W_a^\mu W_b^\nu, \quad i = 1, 2, 3$$

170

171 The terms in the Lagrangian 2.2 proportional to  $\mu^2$  and  $\lambda$  make up the “Higgs  
172 potential” [50]. As normal (see Appendix 10.6), we restrict  $\lambda > 0$  to guarantee our  
173 potential is bounded from below, and we also require  $\mu^2 < 0$ , which gives us the  
174 standard “sombrero” potential shown in 2.1.

This potential has infinitely many minima at  $\langle \phi \rangle = \sqrt{2m/\lambda}$ ; the ground state is *spontaneously* broken by the choice of ground state, which induces a vacuum expectation value (VEV). Without loss of generality, we can choose the Higgs field  $\phi$  to point in

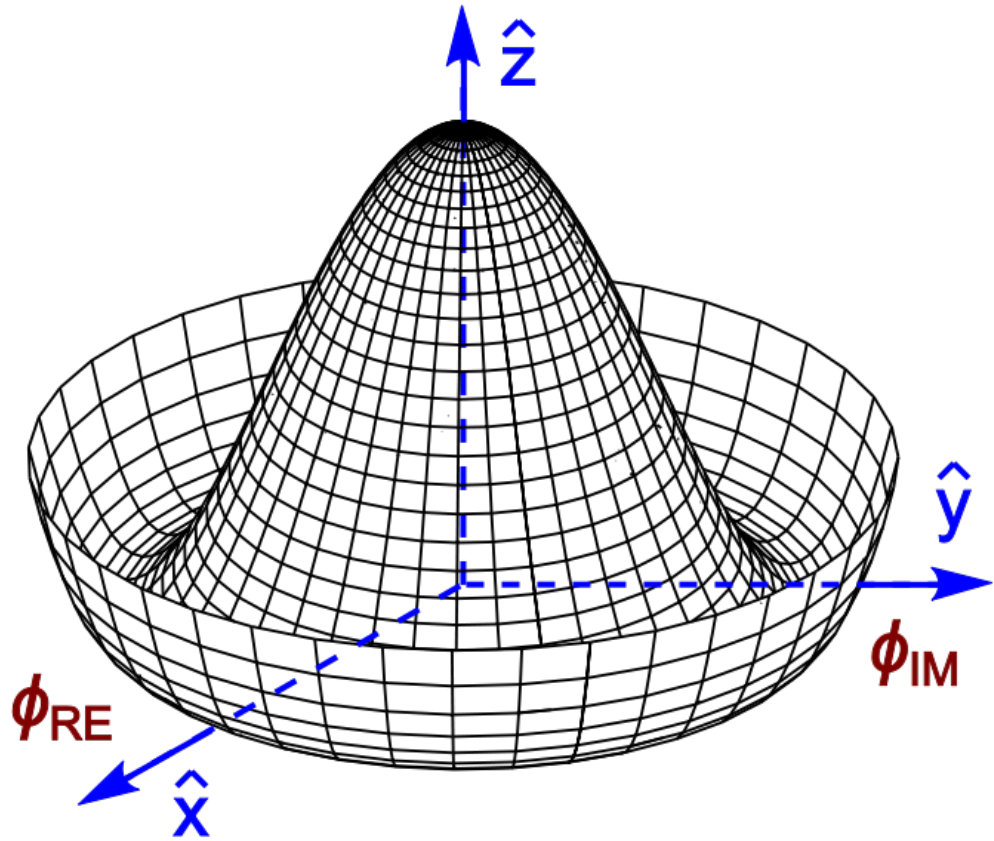


Figure 2.1: Sombrero potential

the real direction, and write the Higgs field  $\phi$  in the following form :

$$\phi = \frac{1}{\sqrt{2}} \exp\left(\frac{i}{v} \sigma_a \theta_a\right) \begin{pmatrix} 0 \\ v + h(x) \end{pmatrix}. \quad (2.5)$$

We choose a gauge to rotate away the dependence on  $\theta_a$ , such that we can write simply

$$\phi = \frac{1}{\sqrt{2}} \begin{pmatrix} 0 \\ v + h(x) \end{pmatrix}. \quad (2.6)$$

Now, we can see how the masses of the vector bosons are generated from the application of the Higgs mechanism. We plug Eq.2.6 back into the electroweak Lagrangian, and only showing the relevant mass terms in the vacuum state where

$h(x) = 0$  see that (dropping the Lorentz indices) :

$$\begin{aligned}\mathcal{L}_M &= \frac{1}{8} \left| \begin{pmatrix} gW_3 + g'B & g(W_1 - iW_2) \\ g(W_1 + iW_2) & -gW_3 + g'B \end{pmatrix} \begin{pmatrix} 0 \\ v \end{pmatrix} \right|^2 \\ &= \frac{g^2 v^2}{8} \left[ W_1^2 + W_2^2 + \left( \frac{g'}{g} B - W_3 \right)^2 \right]\end{aligned}\quad (2.7)$$

Defining the *Weinberg* angle  $\tan(\theta_W) = g'/g$  and the following *physical* fields :

$$\begin{aligned}W^\pm &= \frac{1}{\sqrt{2}}(W_1 \mp iW_2) \\ Z^0 &= \cos \theta_W W_3 - \sin \theta_W B \\ A^0 &= \sin \theta_W W_3 + \cos \theta_W B\end{aligned}\quad (2.8)$$

we can write the piece of the Lagrangian associated to the vector boson masses as

$$\mathcal{L}_{M_V} = \frac{1}{4}g^2 v^2 W^+ W^- + \frac{1}{8}(g^2 + g'^2)v^2 Z^0 Z^0. \quad (2.9)$$

and we have the following values of the masses for the vector bosons :

$$\begin{aligned}m_W^2 &= \frac{1}{4}v^2 g^2 \\ m_Z^2 &= \frac{1}{4}v^2(g^2 + g'^2) \\ m_A^2 &= 0\end{aligned}\quad (2.10)$$

175 We thus see how the Higgs mechanism gives rise to the masses of the  $W^\pm$  and  $Z$   
 176 boson in the Standard Model; the mass of the photon is zero, as expected. The  
 177  $SU(2)_L \otimes U(1)_Y$  symmetry of the initially massless  $W_{1,2,3}$  and  $B$  fields is broken to  
 178 the  $U(1)_{EM}$ . Of the four degrees of freedom in the complex Higgs doublet, three are  
 179 “eaten” when we give mass to the  $W^\pm$  and  $Z_0$ , while the other degree of freedom is  
 180 the Higgs particle, as found in 2012 by the ATLAS and CMS collaborations [51, 52].

## 181 Quantum Chromodynamics

Quantum chromodynamics (or the theory of the *strong* force) characterizes the behavior of *colored* particles, collectively known as *partons*. The partons of the

Standard Model are the (fermionic) quarks, and the (bosonic) gluons. The strong force is governed by  $SU(3)_C$ , an unbroken symmetry in the Standard Model, which implies the gluon remains massless. Defining the covariant derivative for QCD as

$$D^\mu = \partial^\mu + ig_s G_a^\mu L_a, a = 1, \dots, 8 \quad (2.11)$$

where  $L_a$  are the generators of  $SU(3)_C$ , and  $g_s$  is the coupling constant of the strong force. The QCD Lagrangian then is given by

$$\mathcal{L}_{\text{QCD}} = i\bar{\psi}_f D_\mu \gamma^\mu \psi_f - \frac{1}{4} G_{a,\mu\nu} G_a^{\mu\nu} \quad (2.12)$$

where the summation over  $f$  is for quarks *families*, and  $G_a^{\mu\nu}$  is the gluon field strength tensor, given by

$$G_a^{\mu\nu} = \partial^\mu G_a^\nu - \partial^\nu G_a^\mu - g_s f^{abc} G_b^\mu G_c^\nu, a, b, c = 1, \dots, 8 \quad (2.13)$$

182 where  $f^{abc}$  are the structure constants of  $SU(3)_C$ , which are analogous to  $\epsilon_{abc}$  for  
 183  $SU(2)_L$ . The kinetic term for the quarks is contained in the standard  $\partial_\mu$  term, while  
 184 the field strength term contains the interactions between the quarks and gluons, as  
 185 well as the gluon self-interactions.

186 Written down in this simple form, the QCD Lagrangian does not seem much  
 187 different from the QED Lagrangian, with the proper adjustments for the different  
 188 group structures. The gluon is massless, like the photon, so one could naïvely expect  
 189 an infinite range force, and it pays to understand why this is not the case. The  
 190 reason for this fundamental difference is the gluon self-interactions arising in the  
 191 field strength tensor term of the Lagrangian. This leads to the phenomena of *color*  
 192 *confinement*, which describes how one only observes color-neutral particles alone in  
 193 nature. In contrast to the electromagnetic force, particles which interact via the  
 194 strong force experience a *greater* force as the distance between the particles increases.  
 195 At long distances, the potential is given by  $V(r) = -kr$ . At some point, it is more  
 196 energetically favorable to create additional partons out of the vacuum than continue

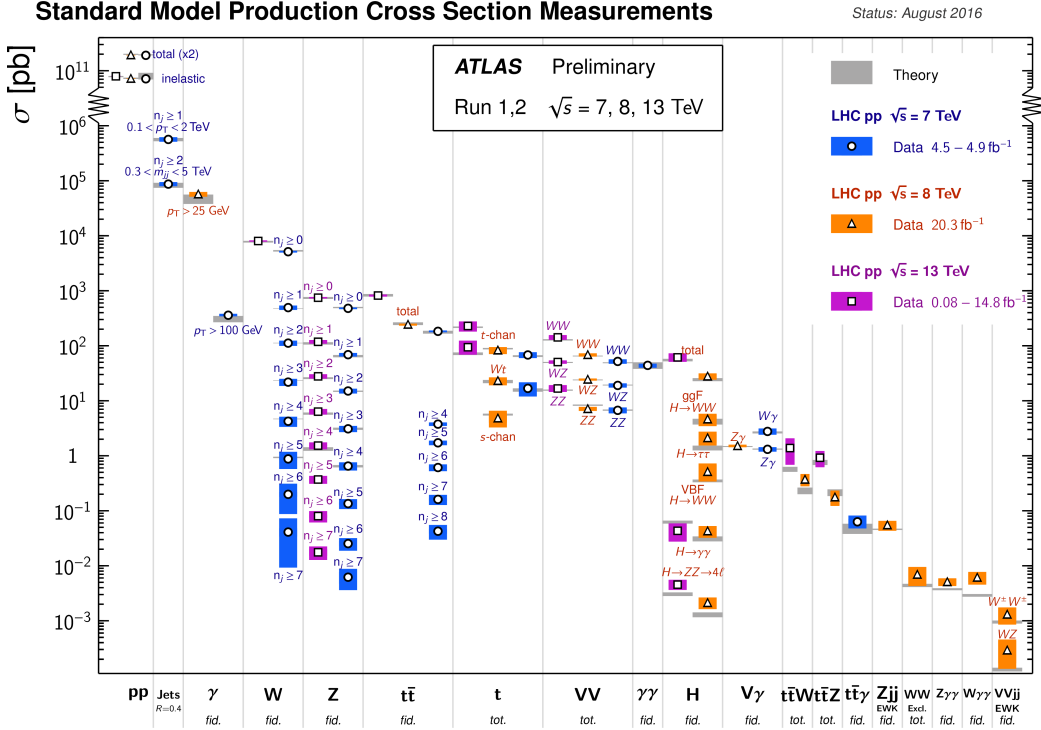


Figure 2.2: Cross-sections of various Standard Model processes

197 pulling apart the existing partons, and the colored particles undergo *fragmentation*.  
198 This leads to *hadronization*. Bare quarks and gluons are actually observed as sprays  
199 of hadrons (primarily kaons and pions); these sprays are known as *jets*, which are  
200 what are observed by experiments.

201 It is important to recognize the importance of understanding these QCD inter-  
202 actions in high-energy hadron colliders such as the LHC. Since protons are hadrons,  
203 proton-proton collisions such as those produced by the LHC are primarily governed by  
204 the processes of QCD. In particular, by far the most frequent process observed in LHC  
205 experiments is dijet production from gluon-gluon interactions (see Fig.2.2). These  
206 gluons that interact are part of the *sea* particles inside the proton; the simple  $p = uud$   
207 model does not apply. The main *valence*  $uud$  quarks are constantly interacting via  
208 gluons, which can themselves radiate gluons or split into quarks, and so on. A more  
209 useful understanding is given by the colloquially-known *bag* model [53, 54], where the  
210 proton is seen as a “bag” of (in principle) infinitely many partons, each with energy

211  $E < \sqrt{s} = 6.5$  TeV. One then collides this (proton) bag with another, and views the  
212 products of this very complicated collision, where calculations include many loops in  
213 nonperturbative QCD calculations.

214 Fortunately, we are generally saved by the QCD factorization theorems [55]. This  
215 allows one to understand the hard (i.e. short distance or high energy)  $2 \rightarrow 2$  parton  
216 process using the tools of perturbative QCD, while making series of approximations  
217 known as a *parton shower* model to understand the additional corrections from  
218 nonperturbative QCD. We will discuss the reconstruction of jets by experiments in  
219 Ch.5.

## 220 Fermions

221 We will now look more closely at the fermions in the Standard Model [56].

222 As noted earlier in Sec.2.2, the fermions of the Standard Model can be first  
223 distinguished between those that interact via the strong force (quarks) and those  
224 which do not (leptons).

There are six leptons in the Standard Model, which can be placed into three  
*generations*.

$$\begin{pmatrix} e \\ \nu_e \end{pmatrix}, \begin{pmatrix} \mu \\ \nu_\mu \end{pmatrix}, \begin{pmatrix} \tau \\ \nu_\tau \end{pmatrix} \quad (2.14)$$

225 There is the electron ( $e$ ), muon ( $\mu$ ), and tau ( $\tau$ ), each of which has an associated  
226 neutrino ( $\nu_e, \nu_\mu, \nu_\tau$ ). Each of the so-called charged (“electron-like”) leptons has  
227 electromagnetic charge  $-1$ , while the neutrinos all have  $q_{EM} = 0$ .

228 Often in an experimental context, lepton is used to denote the stable electron  
229 and metastable muon, due to their striking experimental signatures. Taus are often  
230 treated separately, due to their much shorter lifetime of  $\tau_\tau \sim 10^{-13}s$ ; these decay  
231 through hadrons or the other leptons, so often physics analyses at the LHC treat  
232 them as jets or leptons, as will be done in this thesis.

233 As the neutrinos are electrically neutral, nearly massless, and only interact via the  
 234 weak force, it is quite difficult to observe them directly. Since LHC experiments rely  
 235 overwhelmingly on electromagnetic interactions to observe particles, the presence of  
 236 neutrinos is not observed directly. Neutrinos are instead observed by the conservation  
 237 of four-momentum in the plane transverse to the proton-proton collisions, known as  
 238 *missing transverse energy*.

There are six quarks in the Standard Model : up, down, charm, strange, top, and bottom. Quarks are similar organized into three generations :

$$\begin{pmatrix} u \\ d \end{pmatrix}, \begin{pmatrix} c \\ s \end{pmatrix}, \begin{pmatrix} t \\ b \end{pmatrix} \quad (2.15)$$

239 where we speak of “up-like” quarks and “down-like” quarks.

240 Each up-like quark has charge  $q_{up} = 2/3$ , while the down-like quarks have  $q_{down} =$   
 241  $-1/3$ . At the high energies of the LHC, one often makes the distinction between  
 242 the light quarks ( $u, d, c, s$ ), the bottom quark, and top quark. In general, due to  
 243 the hadronization process described above, the light quarks, with masses  $m_q < \sim$   
 244  $1.5 GeV$  are indistinguishable by LHC experiments. Their hadronic decay products  
 245 generally have long lifetimes and they are reconstructed as jets.<sup>1</sup>. The bottom quark  
 246 hadronizes primarily through the  $B$ -mesons, which generally travels a short distance  
 247 before decaying to other hadrons. This allows one to distinguish decays via  $b$ -quarks  
 248 from other jets; this procedure is known as *b-tagging* and will be discussed more in  
 249 Ch.5. Due to its large mass, the top quark decays before it can hadronize; there  
 250 are no bound states associated to the top quark. The top is of particular interest at  
 251 the LHC; it has a striking signature through its most common decay mode  $t \rightarrow Wb$ .  
 252 Decays via tops, especially  $t\bar{t}$  are frequently an important signal decay mode, or an  
 253 important background process.

---

<sup>1</sup>In some contexts, charm quarks are also treated as a separate category, although it is quite difficult to distinguish charm quarks from the other light quarks.

## Standard Model Interactions (Forces Mediated by Gauge Bosons)



Figure 2.3: The interactions of the Standard Model

### 254 Interactions in the Standard Model

255 We briefly overview the entirety of the fundamental interactions of the Standard  
256 Model; these can also be found in [2.3](#).

257 The electromagnetic force, mediated by the photon, interacts with via a three-  
258 point coupling all charged particles in the Standard Model. The photon thus interacts  
259 with all the quarks, the charged leptons, and the charged  $W^\pm$  bosons.

260 The weak force is mediated by three particles : the  $W^\pm$  and the  $Z^0$ . The  $Z^0$  can  
261 interacts with all fermions via a three-point coupling. A real  $Z_0$  can thus decay to

262 a fermion-antifermion pair of all SM fermions except the top quark, due to its large  
263 mass. The  $W^\pm$  has two important three-point interactions with fermions. First, the  
264  $W^\pm$  can interact with an up-like quark and a down-like quark; an important example  
265 in LHC experiments is  $t \rightarrow Wb$ . The coupling constants for these interactions are  
266 encoded in the unitary matrix known as the Cabibbo–Kobayashi–Maskawa (CKM)  
267 matrix [57, 58], and are generally known as flavor-changing interactions. Secondly,  
268 the  $W^\pm$  interacts with a charged lepton and its corresponding neutrino. In this case,  
269 the unitary matrix that corresponds to CKM matrix for quarks is the identity matrix,  
270 which forbids (fundamental) vertices such as  $\mu \rightarrow We$ . For leptons, instead this is  
271 a two-step process :  $\mu \rightarrow \nu_m u W \rightarrow \nu_m u \bar{\nu}_e e$ . Finally, there are the self-interactions  
272 of the weak gauge bosons. There is a three-point and four-point interaction; all  
273 combinations are allowed which conserve electric charge.

274 The strong force is mediated by the gluon, which as discussed above also carries  
275 the strong color charge. There is the fundamental three-point interaction, where a  
276 quark radiates a gluon. Additionally, there are the three-point and four-point gluon-  
277 only interactions.

## 278 2.3 Deficiencies of the Standard Model

279 At this point, it is quite easy to simply rest on our laurels. This relatively simple  
280 theory is capable of explaining a very wide range of phenomena, which ultimately  
281 break down only to combinations of nine diagrams shown in Fig.2.3. Unfortunately,  
282 there are some unexplained problems with the Standard Model. We cannot go  
283 through all of the potential issues in this thesis, but we will motivate the primary  
284 issues which naturally lead one to *supersymmetry*, as we will see in Ch.3.

The Standard Model has many free parameters; see Table 2.1. In general, we prefer models with less free parameters. A great example of this fact, and the primary

$m_e$	Electron mass	511 keV
$m_\mu$	Muon mass	105.7 MeV
$m_\tau$	Tau mass	1.78 GeV
$m_u$	Up quark mass	1.9 MeV ( $m_{\bar{MS}} = 2\text{GeV}$ )
$m_d$	Down quark mass	4.4 MeV ( $m_{\bar{MS}} = 2\text{GeV}$ )
$m_s$	Strange quark mass	87 MeV ( $m_{\bar{MS}} = 2\text{GeV}$ )
$m_c$	Charm quark mass	1.32 GeV ( $m_{\bar{MS}} = m_c$ )
$m_b$	Bottom quark mass	4.24 GeV ( $m_{\bar{MS}} = m_b$ )
$m_t$	Top quark mass	172.7 GeV (on-shell renormalization)
$\theta_{12}$ CKM	12-mixing angle	13.1°
$\theta_{23}$ CKM	23-mixing angle	2.4°
$\theta_{13}$ CKM	13-mixing angle	0.2°
$\delta$ CKM	CP-violating Phase	0.995
$g'$	U(1) gauge coupling	0.357 ( $m_{\bar{MS}} = m_Z$ )
$g$	SU(2) gauge coupling	0.652 ( $m_{\bar{MS}} = m_Z$ )
$g_s$	SU(3) gauge coupling	1.221 ( $m_{\bar{MS}} = m_Z$ )
$\theta_{QCD}$	QCD vacuum angle	~0
VEV	Higgs vacuum expectation value	246 GeV
$m_H$	Higgs mass	125 GeV

Table 2.1: Parameters of the Standard Model. For values dependent on the renormalization scheme, we use a combination of the on-shell normalization scheme [59–62] and modified minimal subtraction scheme with  $m_{\bar{MS}}$  as indicated in the table[63]

experimental evidence for EWSB, is the relationship between the couplings of the weak force and the masses of the gauge bosons of the weak force :

$$\rho \equiv \frac{m_W^2}{m_Z^2 \cos^2 \theta_W} \stackrel{?}{=} 1 \quad (2.16)$$

where ? indicates that this is a testable prediction of the Standard Model (in particular, that the gauge bosons gain mass through EWSB). This relationship has been measured within experimental and theoretical predictions. We would like to produce additional such relationships, which would exist if the Standard Model is a low-energy approximation of some other theory.

An additional issue is the lack of *gauge coupling unification*. The couplings of any quantum field theory “run” as a function of the distance scales (or inversely, energy scales) of the theory. The idea is closely related to the unification of the

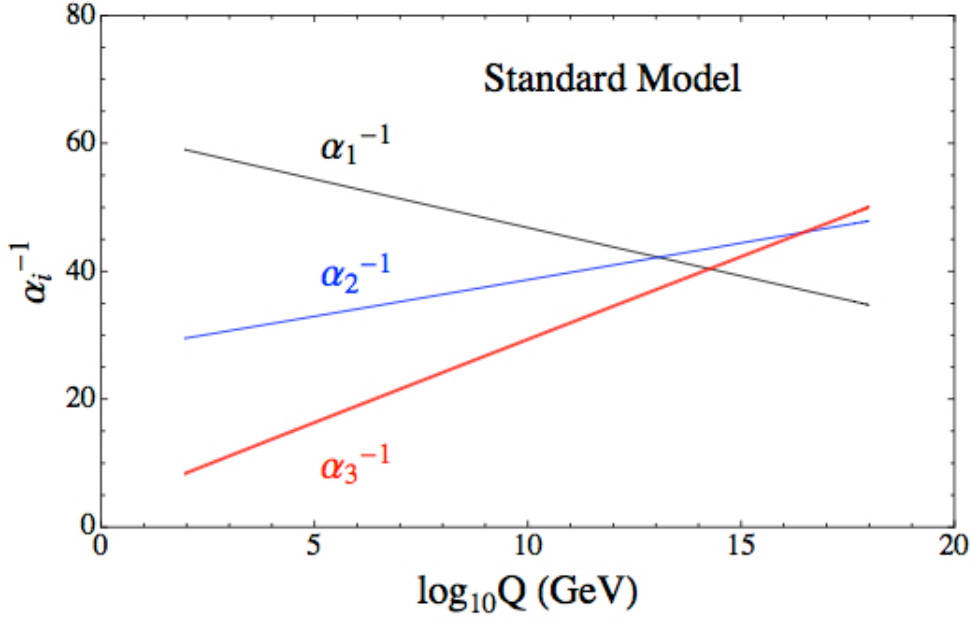


Figure 2.4: The running of Standard Model gauge couplings. The Standard Model couplings do not unify at high energies, which indicates it cannot completely describe nature through the Planck scale.

293 electromagnetic and weak forces at the so-called *electroweak scale* of  $O(100 \text{ GeV})$ .  
 294 One would hope this behavior was repeated between the electroweak forces and the  
 295 strong force at some suitable energy scale. The Standard Model does automatically  
 296 not exhibit this behavior, as we can see in Fig.2.4.

The most significant problem with the Standard Model is the *hierarchy problem*. In its most straightforward incarnation, the Higgs scalar field is subject to quantum corrections through loop diagrams, as shown in Fig.2.5. For demonstration, we use the contributions from the top quark, since the top quark has the largest Higgs Yukawa coupling due to its large mass. In general, we should expect these corrections to be quadratically dependent on the scale of the ultraviolet physics,  $\Lambda$ . Briefly assume there is no new physics before the Planck scale of gravity,  $\Lambda_{\text{Planck}} = 10^{19} \text{ GeV}$ . In this case, we expect the corrections to the Higgs mass like

$$\delta m_H^2 \approx \left( \frac{m_t}{8\pi^2 \langle \phi \rangle_{VEV}} \right)^2 \Lambda_{\text{Planck}}^2. \quad (2.17)$$

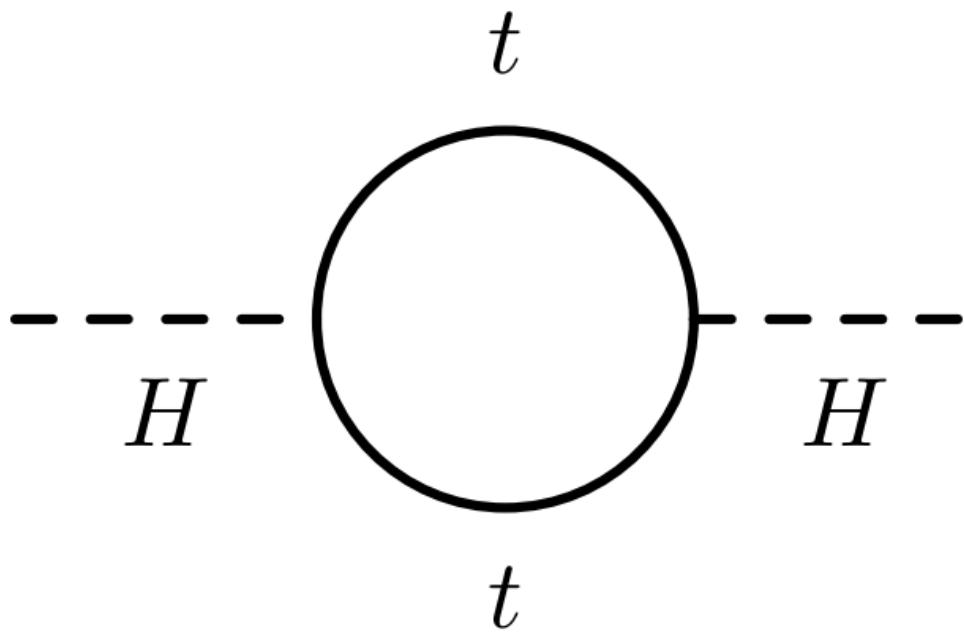


Figure 2.5: The dominant quantum loop correction to the Higgs mass in the Standard Model.

297 To achieve the miraculous cancellation required to get the observed Higgs mass of  
 298 125 GeV, one needs to then set the bare Higgs mass  $m_0$ , our input to the Standard  
 299 Model Lagrangian, itself to a *precise* value  $\sim 10^{19}$  GeV. This extraordinary level of  
 300 parameter finetuning is quite undesirable, and within the framework of the Standard  
 301 Model, there is little that can be done to alleviate this issue.

302 An additional concern, of a different nature, is the lack of a *dark matter* candidate  
 303 in the Standard Model. Dark matter was discovered by observing galactic rotation  
 304 curves, which showed that much of the matter that interacted gravitationally was  
 305 invisible to our (electromagnetic) telescopes [16–22]. The postulation of the existence  
 306 of dark matter, which interacts at least through gravity, allows one to understand  
 307 these galactic rotation curves. Unfortunately, no particle in the Standard Model could  
 308 possibly be the dark matter particle. The only candidate truly worth another look is  
 309 the neutrino, but it has been shown that the neutrino content of the universe is simply  
 310 too small to explain the galactic rotation curves [22, 64]. The experimental evidence

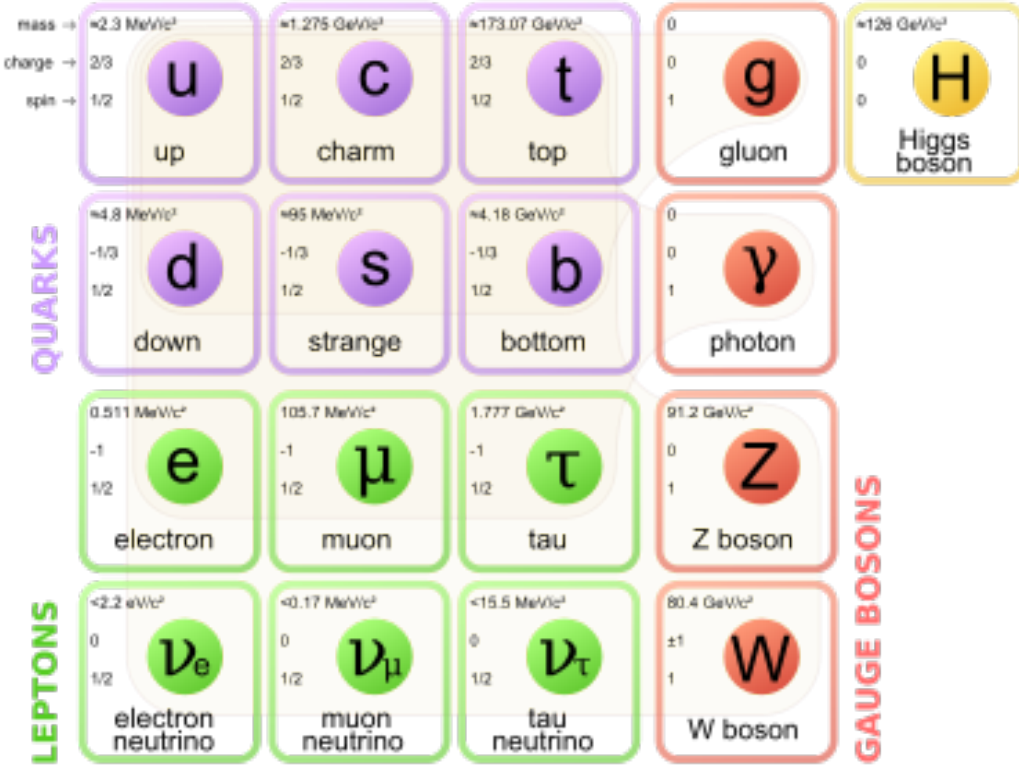


Figure 2.6: Particles of the Standard Model

311 from the galactic rotations curves thus show there *must* be additional physics beyond  
 312 the Standard Model, which is yet to be understood.

313 In the next chapter, we will see how these problems can be alleviated by the theory  
 314 of supersymmetry.



*Supersymmetry*

317 This chapter will introduce supersymmetry (SUSY) [15, 23–35]. We will begin by  
 318 introducing the concept of a *superspace*, and discuss some general ingredients of  
 319 supersymmetric theories. This will include a discussion of how the problems with the  
 320 Standard Model described in Ch.2 are naturally fixed by these theories.

321 The next step is to discuss the particle content of the *Minimally Supersymmetric*  
 322 *Standard Model* (MSSM). As its name implies, this theory contains the minimal  
 323 additional particle content to make Standard Model supersymmetric. We then discuss  
 324 the important phenomenological consequences of this theory, especially as it would  
 325 be observed in experiments at the LHC.

326 **3.1 Supersymmetric theories : from space to  
 327 superspace**

328 **Coleman-Mandula “no-go” theorem**

329 We begin the theoretical motivation for supersymmetry by citing the “no-go” theorem  
 330 of Coleman and Mandula [65]. This theorem forbids *spin-charge unification*; it  
 331 states that all quantum field theories which contain nontrivial interactions must be  
 332 a direct product of the Poincaré group of Lorentz symmetries, the internal product  
 333 from of gauge symmetries, and the discrete symmetries of parity, charge conjugation,  
 334 and time reversal. The assumptions which go into building the Coleman-Mandula

theorem are quite restrictive, but there is one unique way out, which has become known as *supersymmetry* [26, 66]. In particular, we must introduce a *spinorial* group generator  $Q$ . Alternatively, and equivalently, this can be viewed as the addition of anti-commuting coordinates; space plus these new anti-commuting coordinates is then called *superspace* [67]. We will not investiage this view in detail, but it is also a quite intuitive and beautiful way to construct supersymmetry[15].

## 341 Supersymmetry transformations

342 A *supersymmetric* transformation  $Q$  transforms a bosonic state into a fermionic state,  
 343 and vice versa :

$$Q |\text{Fermion}\rangle = |\text{Boson}\rangle \quad (3.1)$$

$$Q |\text{Boson}\rangle = |\text{Fermion}\rangle \quad (3.2)$$

To ensure this relation holds,  $Q$  must be an anticommuting spinor. Additionally, since spinors are inherently complex,  $Q^\dagger$  must also be a generator of the supersymmetry transformation. Since  $Q$  and  $Q^\dagger$  are spinor objects (with  $s = 1/2$ ), we can see that supersymmetry must be a spacetime symmetry. The Haag-Lopuszanski-Sohnius extension [66] of the Coleman-Mandula theorem [65] is quite restrictive about the forms of such a symmetry. Here, we simply write the (anti-) commutation relations [15] :

$$Q_\alpha, Q_{\dot{\alpha}}^\dagger = -2\sigma_{\alpha\dot{\alpha}\mu} P_\mu \quad (3.3)$$

$$Q_\alpha, Q_{\dot{\beta}} = Q_{\dot{\alpha}}^\dagger, Q_{\dot{\beta}}^\dagger = 0 \quad (3.4)$$

$$[P^\mu, Q_\alpha] = [P^\mu, Q_{\dot{\alpha}}^\dagger] = 0 \quad (3.5)$$

<sup>344</sup> **Supermultiplets**

<sup>345</sup> In a supersymmetric theory, we organize single-particle states into irreducible  
<sup>346</sup> representations of the supersymmetric algebra which are known as *supermultiplets*.  
<sup>347</sup> Each supermultiplet contains a fermion state  $|F\rangle$  and a boson state  $|B\rangle$ ; these two  
<sup>348</sup> states are the known as *superpartners*. These are related by some combination of  
<sup>349</sup>  $Q$  and  $Q^\dagger$ , up to a spacetime transformation.  $Q$  and  $Q^\dagger$  commute with the mass-  
<sup>350</sup> squared operator  $-P^2$  and the operators corresponding to the gauge transformations  
<sup>351</sup> [15]; in particular, the gauge interactions of the Standard Model. In an unbroken  
<sup>352</sup> supersymmetric theory, this means the states  $|F\rangle$  and  $|B\rangle$  have exactly the same mass,  
<sup>353</sup> electromagnetic charge, electroweak isospin, and color charges. One can also prove  
<sup>354</sup> [15] that each supermultiplet contains the exact same number of bosonic ( $n_B$ ) and  
<sup>355</sup> fermion ( $n_F$ ) degrees of freedom. We now explore the possible types of supermultiples  
<sup>356</sup> one can find in a renormalizable supersymmetric theory.

<sup>357</sup> Since each supermultiplet must contain a fermion state, the simplest type of  
<sup>358</sup> supermultiplet contains a single Weyl fermion state ( $n_F = 2$ ) which is paired with  
<sup>359</sup>  $n_B = 2$  scalar bosonic degrees of freedom. This is most conveniently constructed as  
<sup>360</sup> single complex scalar field. We call this construction a *scalar supermultiplet* or *chiral*  
<sup>361</sup> *supermultiplet*. The second name is indicative; only chiral supermultiplets can contain  
<sup>362</sup> fermions whose right-handed and left-handed components transform differently under  
<sup>363</sup> the gauge interactions (as of course happens in the Standard Model).

<sup>364</sup> The second type of supermultiplet we construct is known as a *gauge* supermul-  
<sup>365</sup> tiplet. We take a spin-1 gauge boson (which must be massless due to the gauge  
<sup>366</sup> symmetry, so  $n_B = 2$ ) and pair this with a single massless Weyl spinor<sup>1</sup>. The gauge  
<sup>367</sup> bosons transform as the adjoint representation of the their respective gauge groups;  
<sup>368</sup> their fermionic partners, which are known as gauginos, must also. In particular,  
<sup>369</sup> the left-handed and right-handed components of the gaugino fermions have the same

---

<sup>1</sup>Choosing an  $s = 3/2$  massless fermion leads to nonrenormalizable interactions.

370 gauge transformation properties.

371 Excluding gravity, this is the entire list of supermultiplets which can participate  
372 in renormalizable interactions in what is known as  $N = 1$  supersymmetry. This  
373 means there is only one copy of the supersymmetry generators  $Q$  and  $Q^\dagger$ . This is  
374 essentially the only “easy” phenomenological choice, since it is the only choice in four  
375 dimensions which allows for the chiral fermions and parity violations built into the  
376 Standard Model, and we will not look further into  $N > 1$  supersymmetry in this thesis.

377 The primary goal, after understanding the possible structures of the multiplets  
378 above, is to fit the Standard Model particles into a multiplet, and therefore make  
379 predictions about their supersymmetric partners. We explore this in the next section.

## 380 3.2 Minimally Supersymmetric Standard Model

381 To construct what is known as the MSSM [susyPrimer , 68–71], we need a few  
382 ingredients and assumptions. First, we match the Standard Model particles with  
383 their corresponding superpartners of the MSSM. We will also introduce the naming  
384 of the superpartners (also known as *sparticles*). We discuss a very common additional  
385 restraint imposed on the MSSM, known as  $R$ –parity. We also discuss the concept of  
386 soft supersymmetry breaking and how it manifests itself in the MSSM.

### 387 Chiral supermultiplets

388 The first thing we deduce is directly from Sec.?? . The bosonic superpartners  
389 associated to the quarks and leptons *must* be spin 0, since the quarks and leptons must  
390 be arranged in a chiral supermultiplet. This is essentially the note above, since the  
391 chiral supermultiplet is the only one which can distinguish between the left-handed  
392 and right-handed components of the Standard Model particles. The superpartners of  
393 the quarks and leptons are known as *squarks* and *sleptons*, or *sfermions* in aggregate.

394 (for ‘‘scalar quarks’’, ‘‘scalar leptons’’, and ‘‘scalar fermion’’<sup>2</sup>). The ‘‘s-’’ prefix  
 395 can also be added to the individual quarks i.e. *selectron*, *sneutrino*, and *stop*. The  
 396 notation is to add a  $\sim$  over the corresponding Standard Model particle i.e.  $\tilde{e}$ , the  
 397 selectron is the superpartner of the electron. The two-component Weyl spinors of the  
 398 Standard Model must each have their own (complex scalar) partner i.e.  $e_L, e_R$  have  
 399 two distinct partners :  $\tilde{e}_L, \tilde{e}_R$ . As noted above, the gauge interactions of any of the  
 400 sfermions are identical to those of their Standard Model partners.

Due to the scalar nature of the Higgs, it must obviously lie in a chiral supermultiplet. To avoid gauge anomalies and ensure the correct Yukawa couplings to the quarks and leptons[15], we must add additional Higgs bosons to any supersymmetric theory. In the MSSM, we have two chiral supermultiplets. The SM (SUSY) parts of the multiplets are denoted  $H_u(\tilde{H}_u)$  and  $H_d(\tilde{H}_d)$ . Writing out  $H_u$  and  $H_d$  explicitly:

$$H_u = \begin{pmatrix} H_u^+ \\ H_u^0 \end{pmatrix} \quad (3.6)$$

$$H_d = \begin{pmatrix} H_d^0 \\ H_d^- \end{pmatrix} \quad (3.7)$$

(3.8)

401 we see that  $H_u$  looks very similar to the SM Higgs with  $Y = 1$ , and  $H_d$  is symmetric  
 402 to this with  $+ \rightarrow -$ , with  $Y = -1$ . The SM Higgs boson,  $h_0$ , is a linear superposition  
 403 of the neutral components of these two doublets. The SUSY parts of the Higgs  
 404 multiplets,  $\tilde{H}_u$  and  $\tilde{H}_d$ , are each left-handed Weyl spinors. For generic spin-1/2  
 405 sparticles, we add the ‘‘-ino’’ suffix. We then call the partners of the two Higgs  
 406 collectively the *Higgsinos*.

---

<sup>2</sup>The last one should probably have bigger scare quotes.

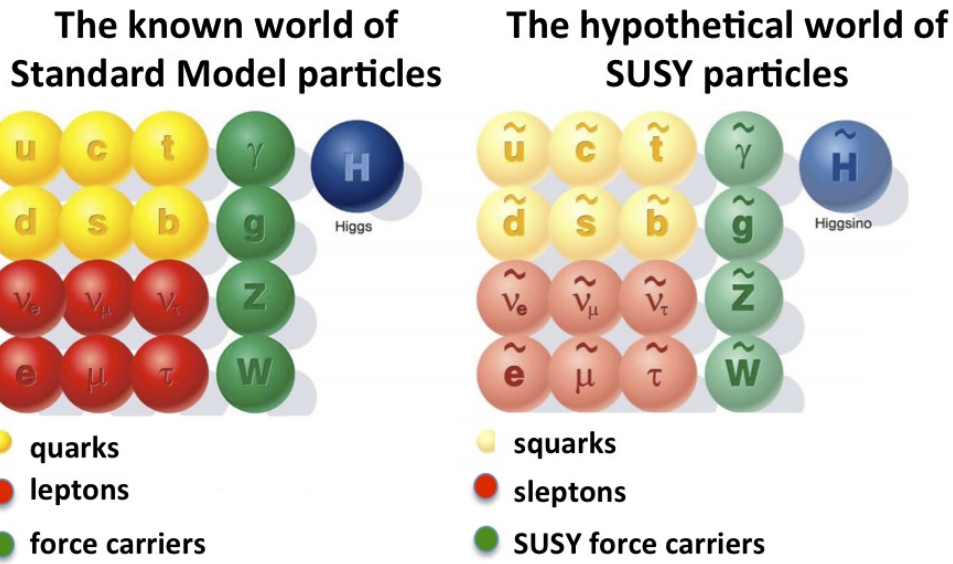


Figure 3.1: Particles of the MSSM

## 407 Gauge supermultiplets

408 The superpartners of the gauge bosons must all be in gauge supermultiplets since  
 409 they contain a spin-1 particle. Collectively, we refer to the superpartners of the  
 410 gauge bosons as the gauginos.

411 The first gauge supermultiplet contains the gluon, and its superpartner, which is  
 412 known as the *gluino*, denoted  $\tilde{g}$ . The gluon is of course the SM mediator of  $SU(3)_C$ ;  
 413 the gluino is also a colored particle, subject to  $SU(3)_C$ . From the SM before EWSB,  
 414 we have the four gauge bosons of the electroweak symmetry group  $SU(2)_L \otimes U(1)_Y$  :  
 415  $W^{1,2,3}$  and  $B^0$ . The superpartners of these particles are thus the *winos*  $W^{\tilde{1},\tilde{2},\tilde{3}}$  and  
 416 *bino*  $\tilde{B}^0$ , where each is placed in another gauge supermultiplet with its corresponding  
 417 SM particle. After EWSB, without breaking supersymmetry, we would also have the  
 418 zino  $\tilde{Z}^0$  and photino  $\tilde{\gamma}$ .

419 The entire particle content of the MSSM can be seen in Fig.3.1.

420 At this point, it's important to take a step back. Where are these particles?  
 421 As stated above, supersymmetric theories require that the masses and all quantum



Figure 3.2: This Feynmann diagram shows how proton decay is induced in the MSSM, if one does not impose  $R$ -parity.

422 numbers of the SM particle and its corresponding sparticle are the same. Of course,  
 423 we have not observed a selectron, squark, or wino. The answer, as it often is, is that  
 424 supersymmetry is *broken* by the vacuum state of nature [15].

425  **$R$ -parity**

This section is a quick aside to the general story.  $R$  – *parity* refers to an additional discrete symmetry which is often imposed on supersymmetric models. For a given particle state, we define

$$R = (-1)^{3(B-L)+2s} \quad (3.9)$$

426 where  $B, L$  is the baryon (lepton) number and  $s$  is the spin. The imposition of  
 427 this symmetry forbids certain terms from the MSSM Lagrangian that would violate  
 428 baryon and/or lepton number. This is required in order to prevent proton decay, as  
 429 shown in Fig.3.2<sup>3</sup>. .

430 In supersymmetric models, this is a  $\mathbb{Z}_2$  symmetry, where SM particles have  $R = 1$   
 431 and sparticles have  $R = -1$ . We will take  $R$  – *parity* as part of the definition of  
 432 the MSSM. We will discuss later the *drastic* consequences of this symmetry on SUSY  
 433 phenomenology

---

<sup>3</sup>Proton decay can actually be prevented by allowing only one of the four potential R-parity violating terms to survive.

434 **Soft supersymmetry breaking**

The fundamental idea of *soft* supersymmetry breaking[15, 34, 35, 72, 73] is that we would like to break supersymmetry without reintroducing the quadratic divergences we discussed at the end of Chapter 2. We write the Lagrangian in a form :

$$\mathcal{L}_{\text{MSSM}} = \mathcal{L}_{\text{SUSY}} + \mathcal{L}_{\text{soft}} \quad (3.10)$$

435 In this sense, the symmetry breaking is “soft”, since we have separated out the  
 436 completely symmetric terms from those soft terms which will not allow the quadratic  
 437 divergences to the Higgs mass.

438 The explicitly allowed terms in the soft-breaking Lagrangian are [35].

- 439 • Mass terms for the scalar components of the chiral supermultipletss  
 440 • Mass terms for the Weyl spinor components of the gauge supermultipletss  
 441 • Trilinear couplings of scalar components of chiral supermultiplets

In particular, using the field content described above for the MSSM, the softly-broken portion of the MSSM Lagrangian can be written

$$\mathcal{L}_{\text{soft}} = -\frac{1}{2} \left( M_3 \tilde{g} \tilde{g} + M_2 \tilde{W} \tilde{W} + M_1 \tilde{B} \tilde{B} + c.c. \right) \quad (3.11)$$

$$- \left( \tilde{u} a_u \tilde{Q} H_u - \tilde{d} a_d \tilde{Q} H_d - \tilde{e} a_e \tilde{L} H_d + c.c. \right) \quad (3.12)$$

$$- \tilde{Q}^\dagger m_Q^2 \tilde{Q} - \tilde{L}^\dagger m_L^2 \tilde{L} - \tilde{u} m_u^2 \tilde{u}^\dagger - \tilde{d} m_d^2 \tilde{d}^\dagger - \tilde{e} m_e^2 \tilde{e}^\dagger \quad (3.13)$$

$$- m_{H_u}^2 H_u^* H_u - m_{H_d}^2 H_d^* H_d - (b H_u H_d + cc). \quad (3.14)$$

442 where we have introduced the following notations :

443 1.  $M_3, M_2, M_1$  are the gluino, wino, and bino masses.

444 2.  $a_u, a_d, a_e$  are complex  $3 \times 3$  matrices in family space.

445 3.  $m_Q^2, m_u^2, m_d^2, m_L^2, m_e^2$  are hermitian  $3 \times 3$  matrices in family space.

446 4.  $m_{H_u}^2, m_{H_d}^2, b$  are the SUSY-breaking contributions to the Higgs potential.

447 We have written matrix terms without any sort of additional notational decoration  
 448 to indicate their matrix nature, and we now show why. The first term 1 are  
 449 straightforward; these are just the straightforward mass terms for these fields. There  
 450 are strong constraints on the off-diagonal terms for the matrices of 2 [74, 75]; for  
 451 simplicity, we will assume that each  $a_i, i = u, d, e$  is proportional to the Yukawa  
 452 coupling matrix :  $a_i = A_{i0}y_i$ . The matrices in ?? can be similarly constrained by  
 453 experiments [68, 75–82] Finally, we assume that the elements 4 contributing to the  
 454 Higgs potential as well as all of the 1 terms must be real, which limits the possible  
 455 CP-violating interactions to those of the Standard Model. We thus only consider  
 456 flavor-blind, CP-conserving interactions within the MSSM.

The important mixing for mass and gauge interaction eigenstates in the MSSM occurs within electroweak sector, in a process akin to EWSB in the Standard Model. The neutral portions of the Higgsinos doublets and the neutral gauginos ( $\tilde{H}_u^0, \tilde{H}_d^0, \tilde{B}^0, \tilde{W}^0$ ) of the gauge interaction basis mix to form what are known as the *neutralinos* of mass basis :

$$M_{\tilde{\chi}} = \begin{pmatrix} M_1 & 0 & -c_\beta s_W m_Z & s_\beta s_W m_Z \\ 0 & M_2 & c_\beta c_W m_Z & -s_\beta c_W m_Z \\ -c_\beta s_W m_Z & c_\beta c_W m_Z & 0 & -\mu \\ s_\beta s_W m_Z & -s_\beta c_W m_Z & -\mu & 0 \end{pmatrix} \quad (3.15)$$

457 where  $s(c)$  are the sine and cosine of angles related to EWSB, which introduced  
 458 masses to the gauginos and higgsinos. Diagonalization of this matrix gives the four  
 459 neutralino mass states, listed without loss of generality in order of increasing mass :  
 460  $\tilde{\chi}_{1,2,3,4}^0$ .

461 The neutralinos, especially the lightest neutralino  $\tilde{\chi}_1^0$ , are important ingredients  
 462 in SUSY phenomenology.

463     The same process can be done for the electrically charged gauginos with  
464     the charged portions of the Higgsino doublets along with the charged winos  
465      $(\tilde{H}_u^+, \tilde{H}_d^+, \tilde{W}^+, \tilde{W}^-)$ . This leads to the *charginos*, again in order of increasing mass  
466     :  $\tilde{\chi}_{1,2}^\pm$ .

467     

### 3.3 Phenomenology

468     We are finally at the point where we can discuss the phenomenology of the MSSM,  
469     in particular as it manifests itself at the energy scales of the LHC.

470     As noted above in Sec.3.2, the assumption of *R*–parity has important conse-  
471     quences for MSSM phenomenology. The SM particles have  $R = 1$ , while the sparticles  
472     all have  $R = -1$ . Simply, this is the “charge” of supersymmetry. Since the particles of  
473     LHC collisions ( $pp$ ) have total incoming  $R = 1$ , we must expect that all sparticles will  
474     be produced in *pairs*. An additional consequence of this symmetry is the fact that the  
475     lightest supersymmetric particle (LSP) is *stable*. Off each branch of the Feynmann  
476     diagram shown in Fig., we have  $R = -1$ , and this can only decay to another sparticle  
477     and a SM particle. Once we reach the lightest sparticle in the decay, it is absolutely  
478     stable. This leads to the common signature  $E_T^{\text{miss}}$  for a generic SUSY signal.

479     For this thesis, we will be presenting an inclusive search for squarks and gluinos  
480     with zero leptons in the final state. This is a very interesting decay channel<sup>4</sup>, due  
481     to the high cross-sections of  $\tilde{g}\tilde{g}$  and  $\tilde{q}\tilde{q}$  decays, as can be seen in Fig.?? [83]. This  
482     is a direct consequence of the fact that these are the colored particles of the MSSM.  
483     Since the sparticles interact with the gauge groups of the SM in the same way as their  
484     SM partners, the colored sparticles, the squarks and gluinos, are produced and decay  
485     as governed by the color group  $SU(3)_C$  with the strong coupling  $g_S$ . The digluino  
486     production is particularly copious, due to color factor corresponding to the color octet

---

<sup>4</sup>Prior to Run1, probably the most *most* interesting SUSY decay channel.

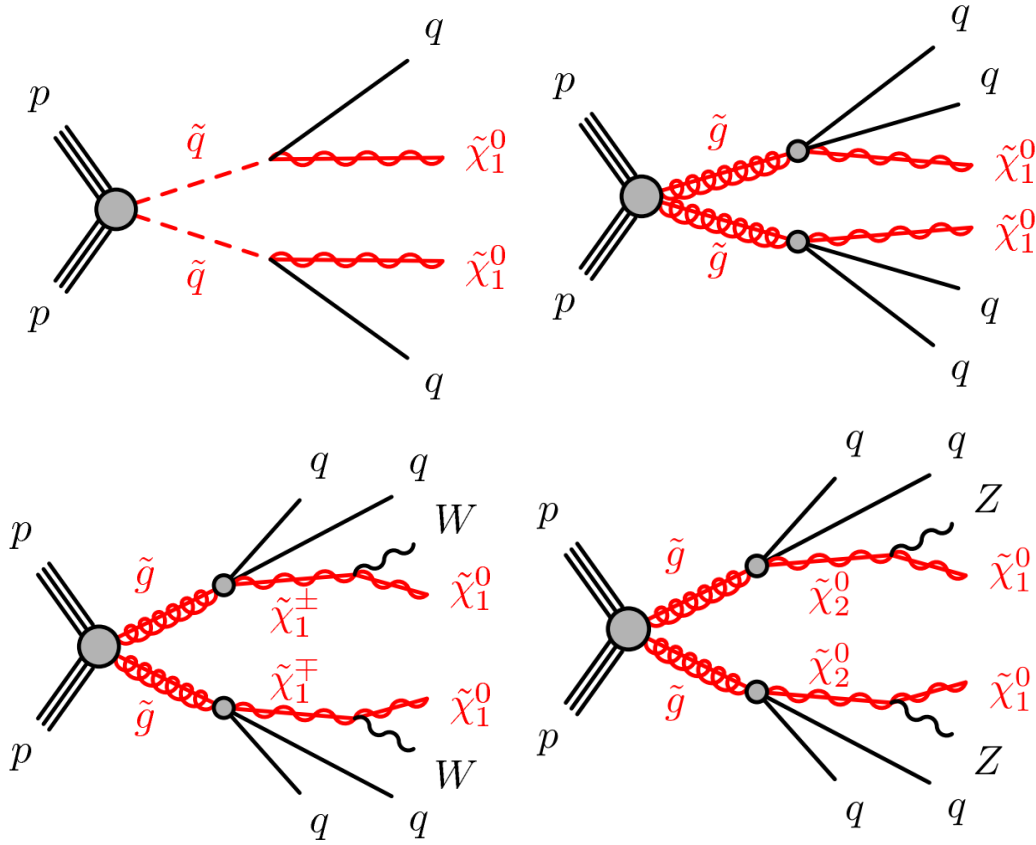


Figure 3.3: SUSY signals considered in this thesis

487 of  $SU(3)C$ .

488 In the case of disquark production, the most common decay mode of the squark in  
 489 the MSSM is a decay directly to the LSP plus a single SM quark [15]. This means the  
 490 basic search strategy of disquark production is two jets from the final state quarks,  
 491 plus missing transverse energy for the LSPs. There are also cascade decays, the most  
 492 common of which, and the only one considered in this thesis, is  $\tilde{q} \rightarrow q\chi_1^\pm \rightarrow qW^\pm\chi_1^0$ .

493 For digluino production, the most common decay is  $\tilde{g} \rightarrow g\tilde{q}$ , due to the large  
 494  $g_S$  coupling. The squark then decays as listed above. In this case, we generically  
 495 search for four jets and missing transverse energy from the LSPs. We can also have  
 496 the squark decay in association with a  $W^\pm$  or  $Z^0$ ; in this thesis, we are interested in  
 497 those cases where this vector boson goes hadronically.

498 In the context of experimental searches for SUSY, we often consider *simplified*

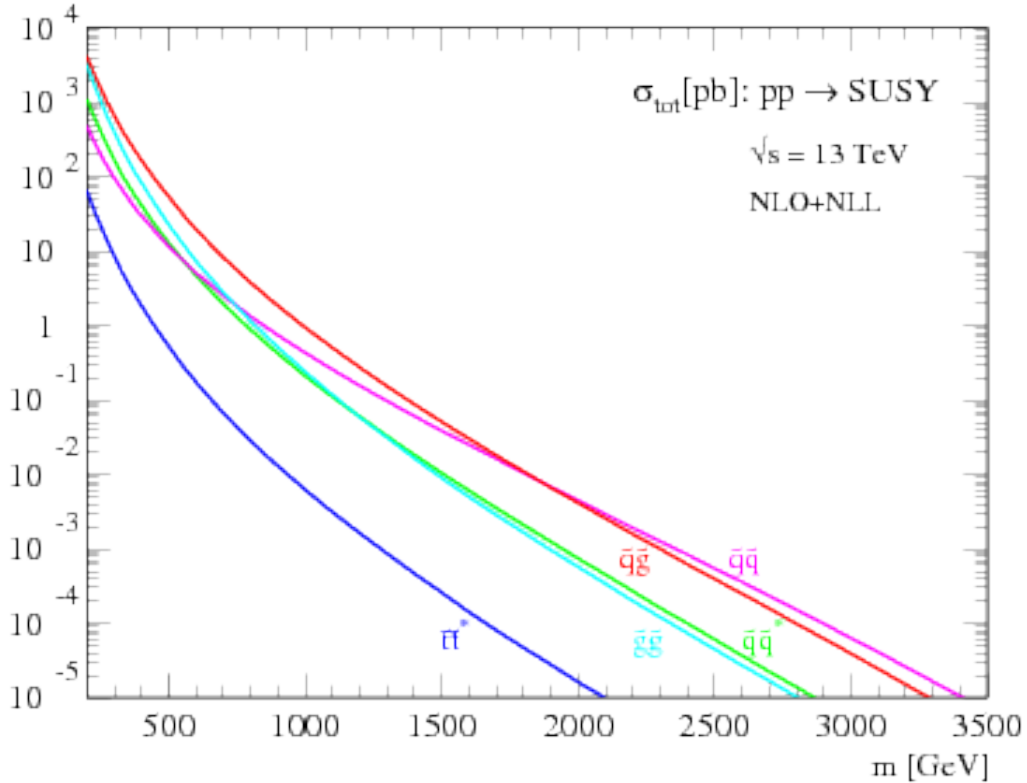


Figure 3.4: SUSY production cross-sections as a function of sparticle mass at  $\sqrt{s} = 13$  TeV.

499 *models*. These models make certain assumptions which allow easy comparisons of  
 500 results by theorists and rival experimentalists. In the context of this thesis, the  
 501 simplified models will make assumptions about the branching ratios described in the  
 502 preceding paragraphs. In particular, we will often choose a model where the decay of  
 503 interest occurs with 100% branching ratio. This is entirely for ease of interpretation  
 504 by other physicists<sup>5</sup>, but it is important to recognize that these are more a useful  
 505 comparison tool, especially with limits, than a strict statement about the potential  
 506 masses of sought-after beyond the Standard Model particle.

---

<sup>5</sup>In the author's opinion, this often leads to more confusion than comprehension. We will revisit the shortcomings of simplified models in the Conclusion to this thesis.

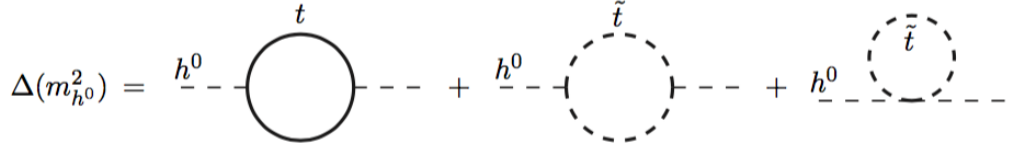


Figure 3.5: Loop diagrams correct the Higgs mass in the MSSM

## 507 3.4 How SUSY solves the problems with the SM

508 We now return to the issues with the Standard Model as described in Ch.2 to see  
 509 how these issues are solved by supersymmetry.

### 510 Quadratic divergences to the Higgs mass

The quadratic divergences induced by the loop corrections to the Higgs mass, for example from the top Yukawa coupling, goes as

$$\delta m_H^2 \approx \left( \frac{m_t}{8\pi^2 \langle \phi \rangle_{VEV}} \right)^2 \Lambda_{Planck}^2. \quad (3.16)$$

511 The miraculous thing about SUSY is each of these terms *automatically* comes  
 512 with a term which exactly cancels this contribution[15]. The fermions and bosons  
 513 have opposite signs in this loop diagram to all orders in perturbation theory, which  
 514 completely solves the hierarchy problem. This is the most well-motivated reason for  
 515 supersymmetry.

### 516 Gauge coupling unification

517 An additional motivation for supersymmetry is seen by the gauge coupling unification  
 518 high scales. In the Standard Model, as we saw the gauge couplings fail to unify at  
 519 high energies. In the MSSM and many other forms of supersymmetry, the gauge  
 520 couplings unify at high energy, as can be seen in Fig.???. This provides additional  
 521 aesthetic motivation for supersymmetric theories.



Figure 3.6: The running of Standard Model gauge couplings; compare to Fig.2.4. The MSSM gauge couplings nearly intersect at high energies.

## 522 Dark matter

523 As we discussed previously, the lack of any dark matter candidate in the Standard  
 524 Model naturally leads to beyond the Standard Model theories. In the Standard Model,  
 525 there is a natural dark matter candidate in the lightest supersymmetric particle[15]  
 526 The LSP would in dark matter experiments be called a *weakly-interacting massive*  
 527 *particle* (WIMP), which is a type of cold dark matter [22, 84]. These WIMPS would  
 528 only interact through the weak force and gravity, which is exactly as a model like the  
 529 MSSM predicts for the neutralino. In Fig.3.7, we can see the current WIMP exclusions  
 530 for a given mass. The range of allowed masses which have not been excluded for LSPs  
 531 and WIMPs have significant overlap. This provides additional motivation outside of  
 532 the context of theoretical details.



Figure 3.7: WIMP exclusions from direct dark matter detection experiments.

### 533 3.5 Conclusions

534 Supersymmetry is the most well-motivated theory for physics beyond the Standard  
 535 Model. It provides a solution to the hierarchy problem, leads to gauge coupling  
 536 unification, and provides a dark matter candidate consistent with galactic rotation  
 537 curves. As noted in this chapter, due to the LSPs in the final state, most SUSY  
 538 searches require a significant amount of missing transverse energy in combination  
 539 with jets of high transverse momentum. However, there is some opportunity to do  
 540 better than this, especially in final states where one has two weakly-interacting LSPs  
 541 on opposite sides of some potentially complicated decay tree. We will see how this is  
 542 done in Ch.??.



*The Large Hadron Collider*

545 The Large Hadron Collider (LHC) produces high-energy protons which are collided  
 546 at the center of multiple large experiments at CERN on the outskirts of Geneva,  
 547 Switzerland [85]. The LHC produces the highest energy collisions in the world,  
 548 with design center-of-mass energy of  $\sqrt{s} = 14$  TeV, which allows the experiments  
 549 to investigate physics far beyond the reach of previous colliders. This chapter will  
 550 summarize the basics of accelerator physics, especially with regards to discovering  
 551 physics beyond the Standard Model. We will describe the CERN accelerator complex  
 552 and the LHC.

553 **4.1 Basics of Accelerator Physics**

554 This section follows closely the presentation of [86].

Simple particle accelerators simply rely on the acceleration of charged particles in a static electric field. Given a field of strength  $E$ , charge  $q$ , and mass  $m$ , this is simply

$$a = \frac{qE}{m}. \quad (4.1)$$

555 For a given particle with a given mass and charge, this is limited by the static electric  
 556 field which can be produced, which in turn is limited by electrical breakdown at high  
 557 voltages.

558 There are two complementary solutions to this issue. First, we use the *radio*  
 559 *frequency acceleration* technique. We call the devices used for this *RF cavities*. The

560    cavities produce a time-varied electric field, which oscillate such that the charged  
 561    particles passing through it are accelerated towards the design energy of the RF  
 562    cavity. This oscillation also induces the particles into *bunches*, since particles which  
 563    are slightly off in energy from that induced by the RF cavity are accelerated towards  
 564    the design energy.

Second, one bends the particles in a magnetic field, which allows them to pass through the same RF cavity over and over. This second process is often limited by *synchrotron radiation*, which describes the radiation produced when a charged particle is accelerated. The power radiated is

$$P \sim \frac{1}{r^2} \left( E/m \right)^4 \quad (4.2)$$

565    where  $r$  is the radius of curvature and  $E, m$  is the energy (mass) of the charged  
 566    particle. Given an energy which can be produced by a given set of RF cavities (which  
 567    is *not* limited by the mass of the particle), one then has two options to increase the  
 568    actual collision energy : increase the radius of curvature or use a heavier particle.  
 569    Practically speaking, the easiest options for particles in a collider are protons and  
 570    electrons, since they are (obviously) copious in nature and do not decay<sup>1</sup>. Given the  
 571    dependence on mass, we can see why protons are used to reach the highest energies.  
 572    The tradeoff for this is that protons are not point particles, and we thus we don't  
 573    know the exact incoming four-vectors of the protons, as discussed in Ch.2.

The particle *beam* refers to the bunches all together. An important property of a beam of a particular energy  $E$ , moving in uniform magnetic field  $B$ , containing particles of momentum  $p$  is the *beam rigidity* :

$$R \equiv rB = p/c. \quad (4.3)$$

574    The linear relation between  $r$  and  $p$ , or alternatively  $B$  and  $p$  have important  
 575    consequences for LHC physics. For hadron colliders, this is the limiting factor on

---

<sup>1</sup>Muon colliders are a really cool option at high energies, since the relativistic  $\gamma$  factor gives them a relatively long lifetime in the lab frame.

576 going to higher energy scales; one needs a proportionally larger magnetic field to  
577 keep the beam accelerating in a circle.

578 Besides the rigidity of the beam, the most important quantities to characterize  
579 a beam are known as the (normalized) *emittance*  $\epsilon_N$  and the *betatron function*  $\beta$ .  
580 These quantities determine the transverse size  $\sigma$  of a relativistic beam  $v \gtrsim c$  beam :  
581  $\sigma^2 = \beta^* \epsilon_N / \gamma_{\text{rel}}$ , where  $\beta^*$  is the value of the betatron function at the collision point  
582 and  $\gamma_{\text{rel}}$  is the Lorentz factor.

These quantities determine the *instantaneous luminosity*  $L$  of a collider, which combined with the cross-section  $\sigma$  of a particular physics process, give the rate of this physics process :

$$R = L\sigma. \quad (4.4)$$

The instantaneous luminosity  $L$  is given by :

$$L = \frac{f_{\text{rev}} N_b^2 F}{4\pi\sigma^2} = \frac{f_{\text{rev}} n N_b^2 \gamma_{\text{rel}} F}{4\pi\beta^* \epsilon_N}. \quad (4.5)$$

583 Here we have introduced the frequency of revolutions  $f_{\text{rev}}$ , the number of bunches  $n$ ,  
584 the number of protons per bunch  $N_b^2$ , and a geometric factor  $F$  related to the crossing  
585 angle of the beams.

The *integrated luminosity*  $\int L$  gives the total number of a particular physics process  $P$ , with cross-section  $\sigma_P$ .

$$N_P = \sigma_P \int L. \quad (4.6)$$

586 Due to this simple relation, one can also quantify the “amount of data delivered” by  
587 a collider simply by  $\int L$ .

## 588 4.2 Accelerator Complex

589 The Large Hadron Collider is the last accelerator in a chain of accelerators which  
590 together form the CERN accelerator complex, which can be seen in 4.1. The protons



Figure 4.1: The CERN accelerator complex.

begin their journey to annihilation in a hydrogen source, where they are subsequently ionized. The first acceleration occurs in the Linac 2, a linear accelerator composed of RF cavities. The protons leave the Linac 2 at an energy of 50 MeV and enter the Proton Synchrotron Booster (PSB). The PSB contains four superimposed rings, which accelerate the protons to 1.4 GeV. The protons are then injected into the Proton Synchrotron (PS). This synchrotron increases the energy up to 25 GeV. After leaving the PS, the protons enter the Super Proton Synchrotron (SPS). This is the last step before entering the LHC ring, and the protons are accelerated to 450 GeV. From the SPS, the protons are injected into the beam pipes of the LHC. The process to fill the LHC rings with proton bunches from start to finish typically takes about four minutes.

602 **4.3 Large Hadron Collider**

The Large Hadron Collider is the final step in the CERN accelerator complex, and produces the collisions analyzed in this thesis. From the point of view of experimentalists on the general-purpose ATLAS and CMS experiments, the main goal of the LHC is to deliver collisions at the highest possible energy, with the highest possible instantaneous luminosity. The LHC was installed in the existing 27 km tunnel used by the Large Electron Positron (LEP) collider [87]. This allowed the existing accelerator complex at CERN, described in the previous section, to be used as the injection system to prepare the protons up to 450 GeV. Many aspects of the LHC design were decided by this very fact, and specified the options allowed to increase the energy or luminosity. In particular, the radius of the tunnel was already specified; from Eq.4.3, this implies the momentum (or energy) of the beam is entirely determined by the magnetic field. Given the 27 km circumference of the LEP tunnel, one can calculate the required magnetic field to reach the 7 TeV per proton design energy of the LHC :

$$r = C/2\pi = 4.3 \text{ km} \quad (4.7)$$

$$\rightarrow B = \frac{p}{rc} = 5 \text{ T} \quad (4.8)$$

603 In fact, the LHC consists of 8 528 m straight portions consisting of RF cavities, used  
604 to accelerate the particles, and 8 circular portions which bend the protons around the  
605 LHC ring. These circular portions actually have a slightly smaller radius of curvature  
606  $r = 2804 \text{ m}$ , and we require  $B = 8.33 \text{ T}$ . To produce this large field, we need to use  
607 superconducting magnets, as discussed in the next section.

608 **Magnets**

609 There are many magnets used by the LHC machine, but the most important are the  
610 1232 dipole magnets; a schematic is shown in Fig.4.2 and a photograph is shown in



CERN AC/DI/MM — 2001/06

Figure 4.2: Schematic of an LHC dipole magnet.

611 Fig.4.3.

612 The magnets are made of Niobium and Titanium. The maximum field strength is  
 613 10 T when cooled to 1.9 Kelvin. The magnets are cooled by superfluid helium, which  
 614 is supplied by a large cryogenic system. Due to heating between the eight helium  
 615 refrigerators and the beampipe, the helium is cooled in the refrigerators to 1.8 K.

616 A failure in the cooling system can cause what is known as a *quench*. If the  
 617 temperature goes above the critical superconducting temperature, the metal loses its  
 618 superconducting properties, which leads to a large resistance in the metal. This leads  
 619 to rapid temperature increases, and can cause extensive damages if not controlled.

620 The dipole magnets are 16.5 meters long with a diameter of 0.57 meters. There  
 621 are two individual beam pipes inside each magnet, which allows the dipoles to house  
 622 the beams travelling in both directions around the LHC ring. They curve slightly,  
 623 at an angle of 5.1 mrad, which carefully matches the curvature of the ring. The

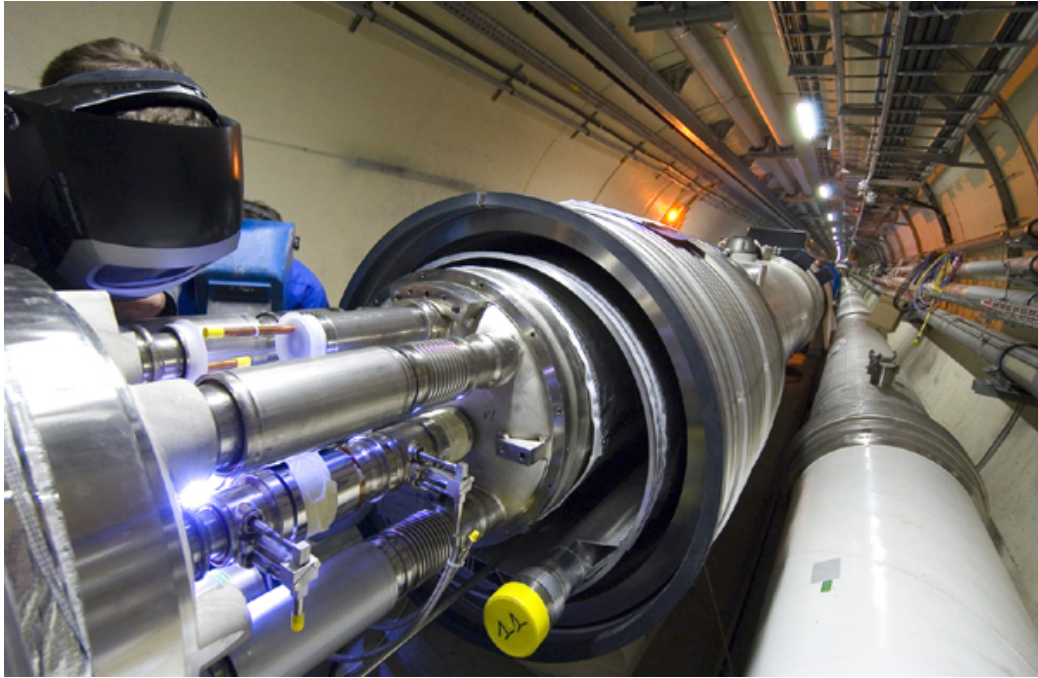


Figure 4.3: Photograph of a technician connecting an LHC dipole magnet.

624 beampipes inside of the magnets are held in high vacuum, to avoid stray particles  
625 interacting with the beam.

## 626 **4.4 Dataset Delivered by the LHC**

627 In this thesis, we analyze the data delivered by the LHC to ATLAS in the 2015 and  
628 2016 datasets. The beam parameters relevant to this dataset are available in Table  
629 [4.1](#).

630 The peak instantaneous luminosity delivered in 2015 (2016) was  $L =$   
631  $5.2(11) \text{ cm}^{-2}\text{s}^{-1} \times 10^{33}$ . One can note that the instantaneous luminosity delivered in  
632 the 2016 dataset exceeds the design luminosity of the LHC. The total integrated  
633 luminosity delivered was  $13.3 \text{ fb}^{-1}$ . In Figure [4.4](#), we display the integrated luminosity  
634 as a function of day for 2015 and 2016.

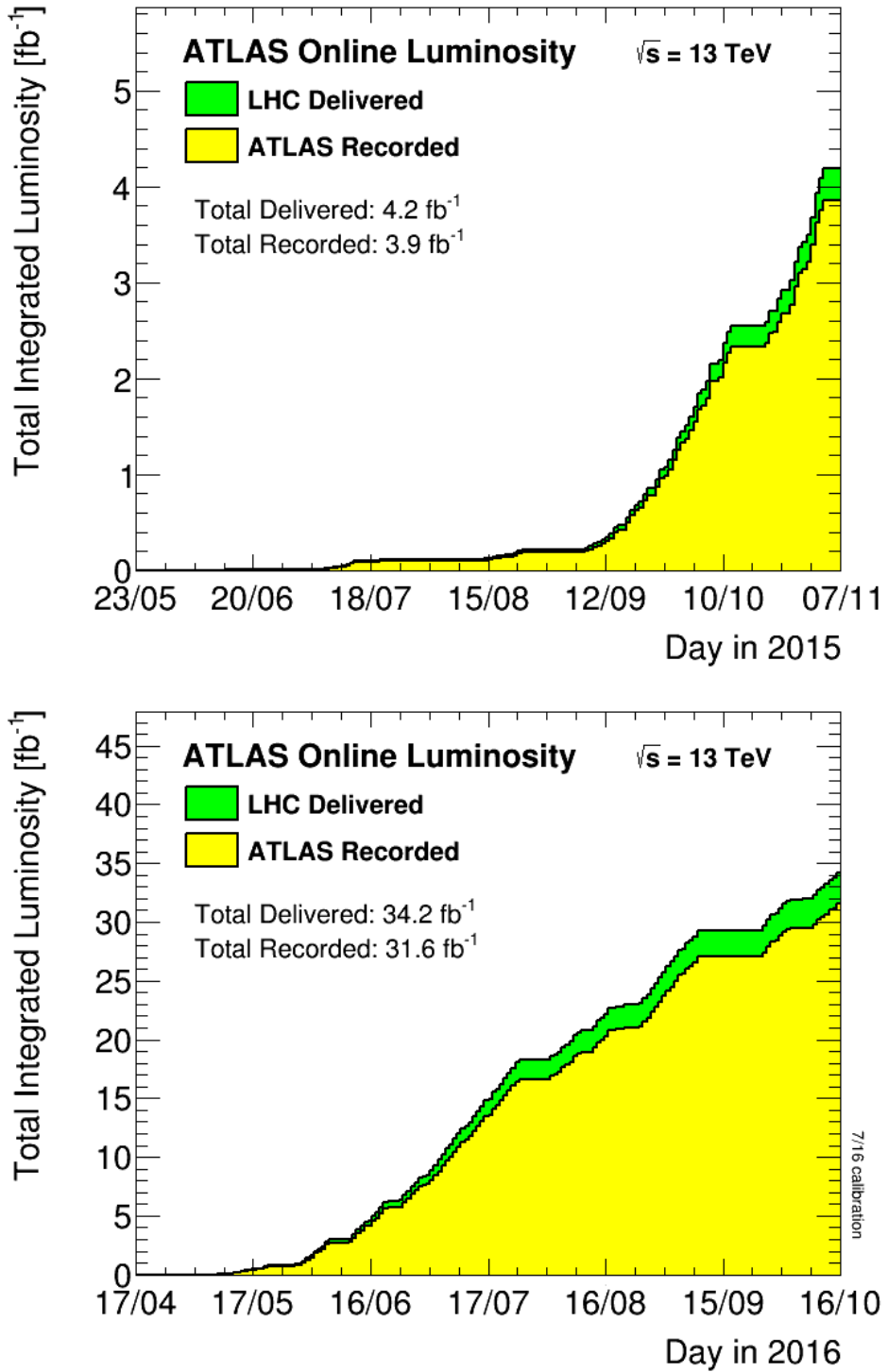


Figure 4.4: Integrated Luminosity delivered by the LHC and collected by ATLAS in the 2015 and 2016 datasets.

Parameter	Injection	Extraction
Energy (GeV)	450	7000
Rigidity (T-m)	3.8	23353
Bunch spacing (ns)	25	25
Design Luminosity ( $\text{cm}^{-2}\text{s}^{-1} \times 10^3$ )	-	1.0
Bunches per proton beam	2808	2808
Protons per bunch	1.15 e11	1.15 e11
Beam lifetime (hr)	-	10
Normalized Emittance $\epsilon_N$ (mm $\mu\text{rad}$ )	3.3	3.75
Betatron function at collision point $\beta^*$ (cm)	-	55

Table 4.1: Beam parameters of the Large Hadron Collider.

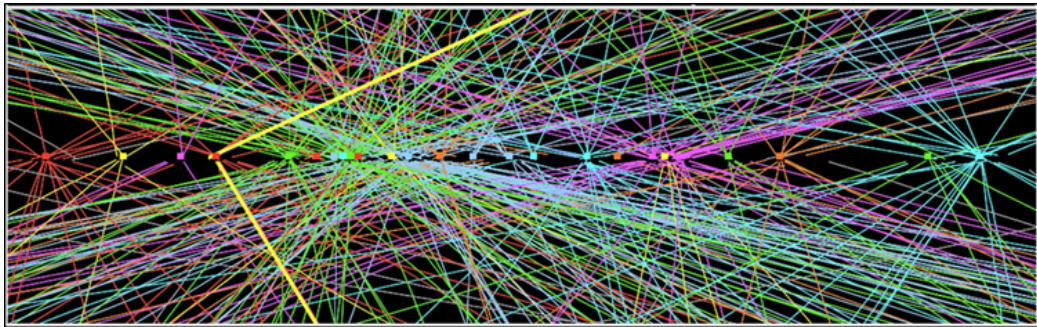


Figure 4.5: Simulated event with many pileup vertices.

## 635 Pileup

636 *Pileup* is the term for the additional proton-proton interactions which occur during  
 637 each bunch crossing of the LHC. At the beginning of the LHC physics program, there  
 638 had not been a collider which averaged more than a single interaction per bunch  
 639 crossing. In the LHC, each bunch crossing (or *event*) generally contains multiple  
 640 proton-proton interactions. An simulated event with many *vertices* can be seen in  
 641 Fig.4.5. The so-called *primary vertex* (or *hard scatter vertex*) refers to the vertex  
 642 which has the highest  $\Sigma p_T^2$ ; this summation occurs over the *tracks* in the detector,  
 643 which we will describe later[**ATL-INDET-PUB-2009-001**]. We then distinguish  
 644 between *in-time* pileup and *out-of-time* pileup. In-time pileup refers to the additional  
 645 proton-proton interactions which occur in the event. Out-of-time pileup refers to  
 646 effects related to proton-proton interactions previous bunch crossings.

647        We quantify in-time pileup by the number of “primary”<sup>2</sup> vertices in a particular  
648    event. To quantify the out-of-time pileup, we use the average number of interactions  
649    per bunch crossing  $\langle \mu \rangle$  over some human-scale time. In Figure 4.6, we show the  
650    distribution of  $\mu$  for the dataset used in this thesis.

---

<sup>2</sup>The primary vertex is as defined above, but we unfortunately use the same name here.



Figure 4.6: Mean number of interactions per bunch crossing in the 2015 and 2016 datasets.



*The ATLAS detector*

653 The dataset analyzed in this thesis was taken by the ATLAS detector [88], which is  
 654 located at the “Point 1” cavern of the LHC beampipe, just across the street from  
 655 the main CERN campus. The much-maligned acronym stands for *A Toroidal LHC*  
 656 *ApparatuS*. ATLAS is a massive cylindrical detector, with a radius of 12.5 m and a  
 657 length of 44 m, with nearly hermitic coverage around the collision point. It consists  
 658 of multiple subdetectors; each plays a role in ATLAS’s ultimate purpose of measuring  
 659 the energy, momentum, and type of the particles produced in collisions delivered by  
 660 the LHC. These subdetectors are immersed in a hybrid solenoid-toroid magnet system  
 661 whichs forces charged particles to curve, which allows for precise measurements of  
 662 their momenta. These magnetic fields are maximized in the central solenoid magnet,  
 663 which contains a magnetic field of 2 T. A schematic of the detector can be seen in  
 664 [5.1](#).

665 The *inner detector* (ID) lies closest to the collision point, and contains three  
 666 separate subdetectors. It provides pseudorapidity<sup>1</sup>coverage of  $|\eta| < 2.5$  for charged  
 667 particles to interact with the tracking material. The tracks reconstructed from the  
 668 inner detector hits are used to reconstruct the primary vertices, as noted in Ch.??,

---

<sup>1</sup>ATLAS uses a right-handed Cartesian coordinate system; the origin is defined by the nominal beam interaction point. The positive- $z$  direction is defined by the incoming beam travelling counterclockwise around the LHC. The positive- $x$  direction points towards the center of the LHC ring from the origin, and the positive- $y$  direction points upwards towards the sky. For particles of transverse (in the  $x - y$  plane) momentum  $p_T = \sqrt{p_x^2 + p_y^2}$  and energy  $E$ , it is generally most convenient fully describe this particle’s kinematics as measured by the detector in the  $(p_T, \phi, \eta, E)$  basis. The angle  $\phi = \arctan(p_y/p_x)$  is the standard azimuthal angle, and  $\eta = \ln \tan(\theta/2)$  is known as the pseudorapidity, and defined based on the standard polar angle  $\theta = \arccos(p_z/p_T)$ . For locations of i.e. detector elements, both  $(r, \phi, \eta)$  and  $(z, \phi, \eta)$  can be useful.



Figure 5.1: The ATLAS detector

and to determine the momemta of charged particles. The ATLAS *calorimeter* consists of two subdetectors, known as the *electromagnetic* and *hadronic* calorimeters. These detectors stop particles in their detector material, and measure the energy deposition inside, which measures the energy of the particles deposited. The calorimeters provide coverage out to pseudorapidity of  $|\eta| < 4.9$ . The muon spectrometer is aptly named; it is specifically used for muons, which are the only particles which generally reach the outer portions of the detector. In this region, we have the large tracking systems of the muon spectrometer, which provide precise measurements of muon momenta. The muon spectrometer has pseudorapidity coverage of  $|\eta| < 2.7$ .

## 5.1 Magnets

ATLAS contains multiple magnetic systems; primarily, we are concerned with the solenoid, used by the inner detector, and the toroids located outside of the ATLAS calorimeter. A schematic is shown in Fig.5.2. These magnetic fields are used to bend

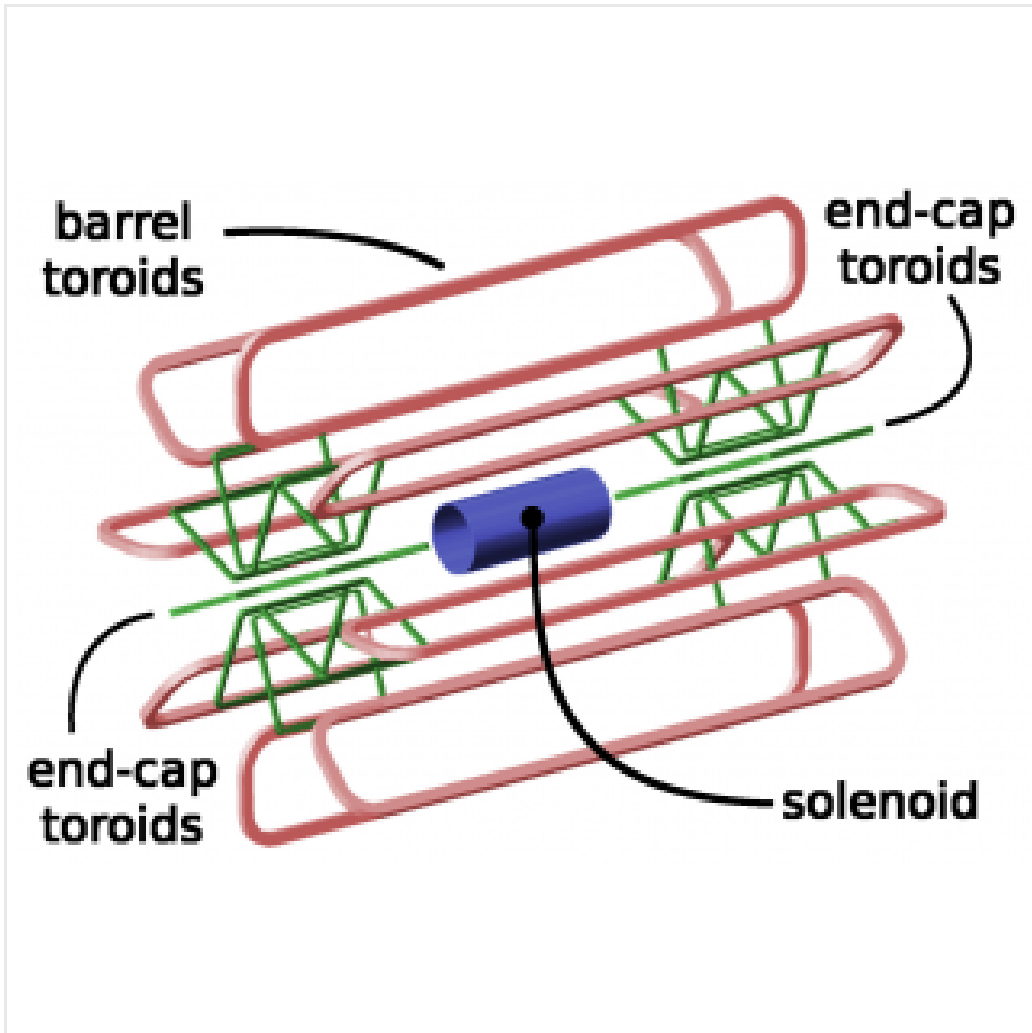


Figure 5.2: The ATLAS magnet system

682 charged particles under the Lorentz force, which subsequently allows one to measure  
683 their momentum.

684 The ATLAS central solenoid is a 2.3 m diameter, 5.3 m long solenoid at the center  
685 of the ATLAS detector. It produces a uniform magnetic field of 2 T; this strong field  
686 is necessary to accurately measure the charged particles in this field. An important  
687 design constraint for the central solenoid was the decision to place it in between the  
688 inner detector and the calorimeters. To avoid excessive impacts on measurements in  
689 the calorimetry, the central solenoid must be as transparent as possible<sup>2</sup>.

---

<sup>2</sup>This is also one of the biggest functional differences between ATLAS and CMS; in CMS, the



Figure 5.3: The ATLAS inner detector

690     The toroid system consists of eight air-core superconducting barrel loops; these  
 691    give ATLAS its distinctive shape. There are also two endcap air-core magnets. These  
 692    produce a magnetic field in a region of approximately 26 m in length and 10 m of  
 693    radius. The magnetic field in this region is non-uniform, due to the prohibitive costs  
 694    of a solenoid magnet of that size.

## 695    **5.2 Inner Detector**

696    The ATLAS inner detector consists of three separate tracking detectors, which are  
 697    known as, in order of increasing distance from the interaction point, the Pixel  
 698    Detector, Semiconductor Tracker (SCT), and the Transition Radiation Tracker  
 699    (TRT). When charged particles pass through these tracking layers, they produce  
 700    *hits*, which using the known 2 T magnetic field, allows the reconstruction of *tracks*.  
 701    Tracks are used as inputs for reconstruction of many higher-level physics objects,

---

solenoid is outside of the calorimeters.

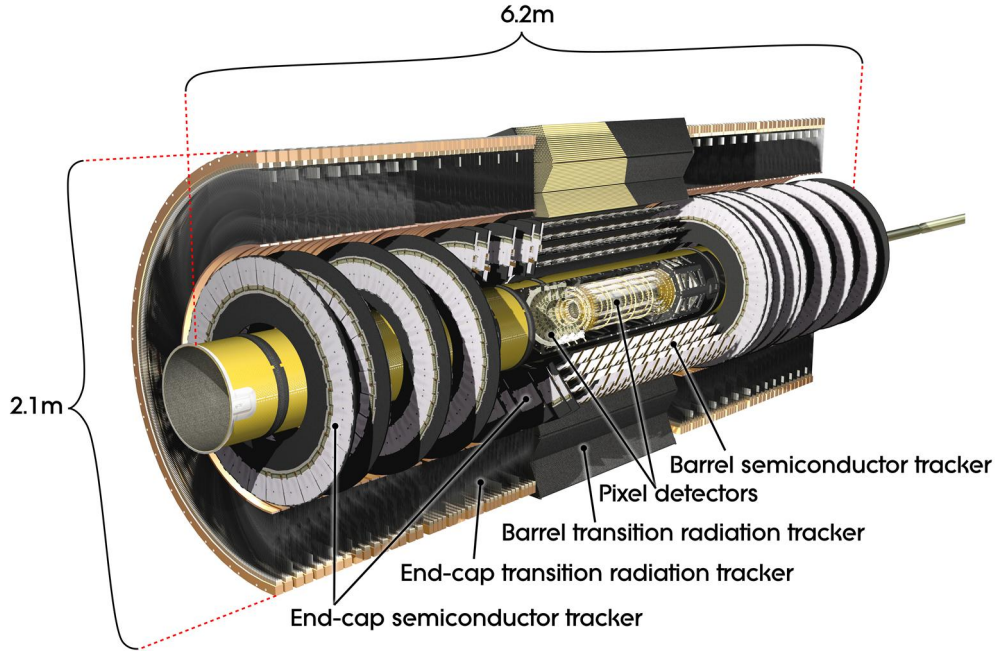


Figure 5.4: The ATLAS pixel detector

such as electrons, muons, photons, and  $E_T^{\text{miss}}$ . Accurate track reconstruction is thus crucial for precise measurements of charged particles.

## Pixel Detector

The ATLAS pixel detector consists four layers of silicon “pixels”. This refers to the segmentation of the active medium into the pixels; compare to the succeeding silicon detectors, which will use silicon “strips”. This provides precise 3D hit locations. The layers are known as the “Insertable”<sup>3</sup>B-Layer (IBL), the B-Layer (or Layer-0), Layer-1, and Layer-2, in order of increasing distance from the interaction point. These layers are very close to the interaction point, and therefore experience a large amount of radiation.

Layer-1, Layer-2, and Layer-3 were installed with the initial construction of ATLAS. They contain front-end integrated electronics (FEI3s) bump-bonded to 1744

---

<sup>3</sup>Very often, the IBL is mistakenly called the Inner B-Layer, which would have been a much more sensible name.

714 silicon modules; each module is  $250\ \mu\text{m}$  in thickness and contains 47232 pixels. These  
715 pixels have planar sizes of  $50 \times 400\ \mu\text{m}^2$  or  $50 \times 600\ \mu\text{m}^2$ , to provide highly accurate  
716 location information. The FEI3s are mounted on long rectangular structures known  
717 as staves, which encircle the beam pipe. A small tilt to each stave allows full coverage  
718 in  $\phi$  even with readout systems which are installed. These layers are at radia of 50.5  
719 mm, 88.5 mm, and 122.5 mm from the interaction point.

720 The IBL was added to ATLAS after Run1 in 2012 at a radius of 33 mm from the  
721 interaction point. The entire pixel detector was removed from the center of ATLAS  
722 to allow an additional pixel layer to be installed. The IBL was required to preserve  
723 the integrity of the pixel detector as radiation damage leads to inoperative pixels in  
724 the other layers. The IBL consists of 448 FEI4 chips, arranged onto 14 staves. Each  
725 FEI4 has 26880 pixels, of planar size  $50 \times 250\ \mu\text{m}$ . This smaller granularity was  
726 required due to the smaller distance to the interaction point.

727 In total, a charged particle passing through the inner detector would expect to  
728 leave four hits in the pixel detector.

## 729 Semiconductor Tracker

730 The SCT is directly beyond Layer-2 of the pixel detector. This is a silicon strip  
731 detector, which do not provide the full 3D information of the pixel detector. The  
732 dual-sensors of the SCT contain  $2 \times 768$  individual strips; each strip has area  $6.4\ \text{cm}^2$ .  
733 The SCT dual-sensor is then double-layered, at a relative angle of 40 mrad;  
734 together these layers provide the necessary 3D information for track reconstruction.  
735 There are four of these double-layers, at radia of 284 mm, 355 mm, 427 mm, and 498  
736 mm. These double-layers provide hits comparable to those of the pixel detector, and  
737 we have four additional hits to reconstruct tracks for each charged particle.

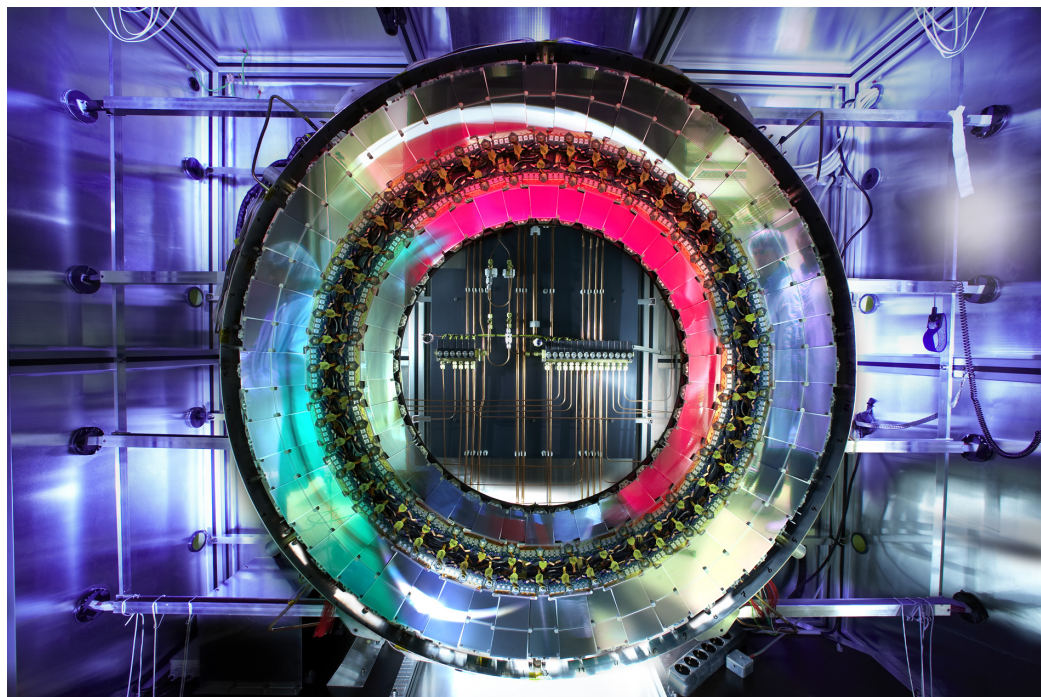


Figure 5.5: A ring of the Semiconductor Tracker

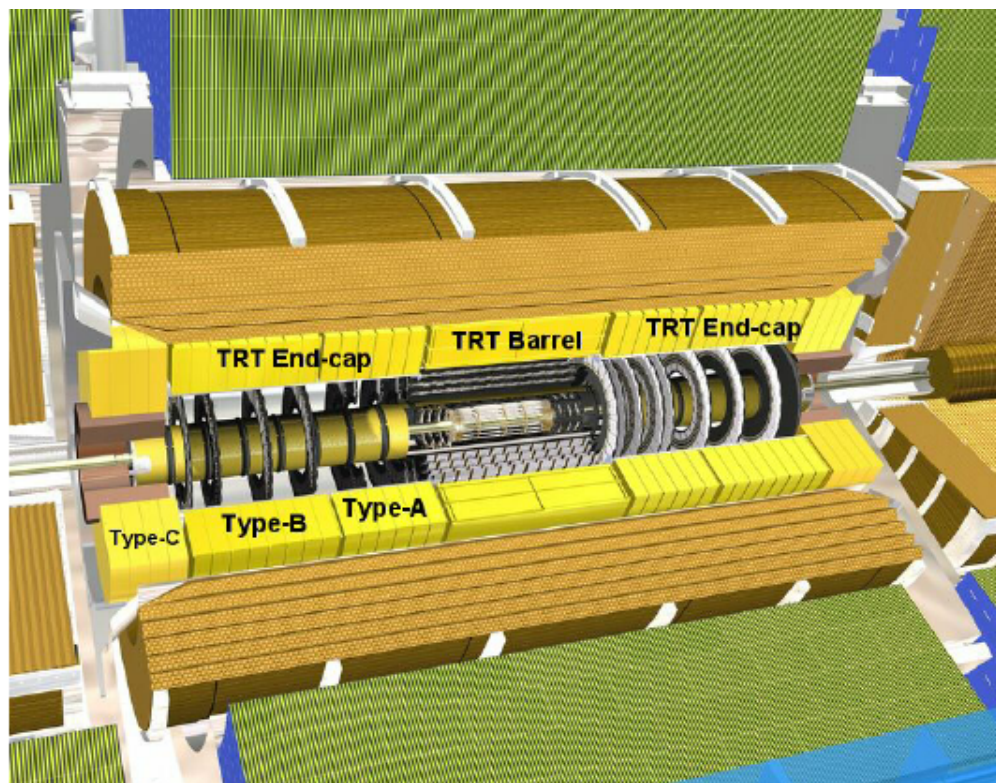


Figure 5.6: A schematic of the Transition Radiation Tracker

738 **Transition Radiation Tracker**

739 The Transition Radiation Tracker is the next detector radially outward from the SCT.  
740 It contains straw drift tubes; these contain a tungsten gold-plated wire of  $32 \mu\text{m}$   
741 diameter held under high voltage (-1530 V) with the edge of the Kapton-aluminum  
742 tube. They are filled with a gas mixture of primarily xenon that is ionized when  
743 a charged particle passes through the tube. The ions are collected by the “drift”  
744 due to the voltage inside the tubes, which is read out by the electronics. This gives  
745 so-called “continuous tracking” throughout the tube, due to the large number of ions  
746 produced.

747 The TRT is so-named due to the *transition radiation* (TR) it induces. Due to  
748 the dielectric difference between the gas and tubes, TR is induced. This is important  
749 for distinguishing electrons from their predominant background of minimum ionizing  
750 particles. Generally, electrons have a much larger Lorentz factor than minimum  
751 ionizing particles, which leads to additional TR. This can be used as an additional  
752 handle for electron reconstruction.

753 **5.3 Calorimetry**

754 The calorimetry of the ATLAS detector also includes multiple subdetectors; these sub-  
755 detectors allow precise measurements of the electrons, photons, and hadrons produced  
756 by the ATLAS detector. Generically, calorimeters work by stopping particles in their  
757 material, and measuring the energy deposition. This energy is deposited as a cascade  
758 particles induce from interactions with the detector material known *showers*. ATLAS  
759 uses *sampling* calorimeters; these alternate a dense absorbing material, which induces  
760 showers, with an active layer which measures energy depositions by the induced  
761 showers. Since some energy is deposited into the absorption layers as well, the energy  
762 depositions must be properly calibrated for the detector.

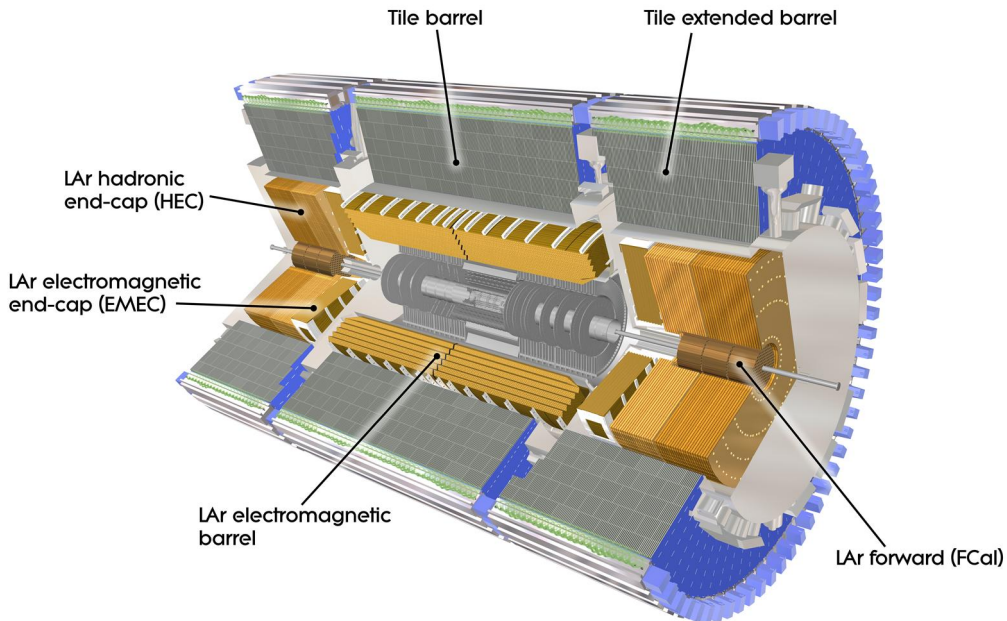


Figure 5.7: The ATLAS calorimeter

763 Electromagnetic objects (electrons and photons) and hadrons have much different  
 764 interaction properties, and thus we need different calorimeters to accurately measure  
 765 these different classes of objects; we can speak of the *electromagnetic* and *hadronic*  
 766 calorimeters. ATLAS contains four separate calorimeters : the liquid argon (LAr)  
 767 electromagnetic barrel calorimeter, the Tile barrel hadronic calorimeter, the LAr  
 768 endcap electromagnetic calorimeter, the LAr endcap hadronic calorimeter, and the  
 769 LAr Forward Calorimeter (FCal). Combined, these provide full coverage in  $\phi$  up to  
 770  $|\eta| < 4.9$ , and can be seen in Fig.5.7.

## 771 Electromagnetic Calorimeters

772 The electromagnetic calorimeters of the ATLAS detector consist of the barrel and  
 773 endcap LAr calorimeters. These are arranged into an ingenious “accordion” shape,  
 774 shown in 5.8, which allows full coverage in  $\phi$  and exceptional coverage in  $\eta$  while  
 775 still allowing support structures for detector operation. The accordion is made of



Figure 5.8: A schematic of a subsection of the barrel LAr electromagnetic calorimeter

layers with liquid argon (active detection material) and lead (absorber) to induce electromagnetic showers. The LAr EM calorimeters are each more than 20 radiation lengths deep, which provides the high stopping power necessary to properly measure the electromagnetic showers.

The barrel component of the LAr EM calorimeter extends from the center of the detector out to  $|\eta| < 1.475$ . The calorimeter has a presampler, which measures the energy of any EM shower induced before the calorimeter. This has segmentation of  $\Delta\eta = 0.025, \Delta\phi = .01$ . There are three “standard” layers in the barrel, which have decreasing segmentation into calorimeter *cells* as one travels radially outward from the interaction point. The first layer has segmentation of  $\Delta\eta = 0.003, \Delta\phi = .1$ , and is quite thin relative to the other layers at only 4 radiation lengths deep. It provides precise  $\eta$  and  $\phi$  measurements for incoming EM objects. The second layer is the deepest at 16 radiation lengths, with a segmentation of  $\Delta\eta = 0.025, \Delta\phi = 0.025$ . It



Figure 5.9: A schematic of Tile hadronic calorimeter

is primarily responsible for stopping the incoming EM particles, which dictates its large relative thickness, and measures most of the energy of the incoming particles. The third layer is only 2 radiation lengths deep, with a rough segmentation of  $\Delta\eta = 0.05$ ,  $\Delta\phi = .025$ . The deposition in this layer is primarily used to distinguish hadrons interacting electromagnetically and entering the hadronic calorimeter from the strictly EM objects which are stopped in the second layer.

The barrel EM calorimeter has a similar overall structure, but extends from  $1.4 < |\eta| < 3.2$ . The segmentation in  $\eta$  is better in the endcap than the barrel; the  $\phi$  segmentation is the same. In total, the EM calorimeters contain about 190000 individual calorimeter cells.

## Hadronic Calorimeters

The hadronic calorimetry of ATLAS sits directly outside the EM calorimetry. It contains three subdetectors : the barrel Tile calorimeter, the endcap LAr calorimeter,

802 and the Forward LAr Calorimeter. Similar to the EM calorimeters, these are  
803 sampling calorimeters that alternate steel (dense material) with an active layer  
804 (plastic scintillator).

805 The barrel Tile calorimeter extends out to  $|\eta| < 1.7$ . There are again three layers,  
806 which combined give about 10 interactions length of distance, which provides excellent  
807 stopping power for hadrons. This is critical to avoid excess *punchthrough* to the muon  
808 spectrometer beyond the hadronic calorimeters. The first layer has a depth of 1.5  
809 interaction lengths. The second layer is again the thickest at a depth of 4.1 interaction  
810 lengths; most of the energy of incoming particle is deposited here. Both the first and  
811 second layer have segmentation of about  $\Delta\eta = 0.1, \Delta\phi = 0.1$ . Generally, one does not  
812 need as fine of granularity in the hadronic calorimeter, since the energy depositions  
813 in the hadronic calorimeters will be summed into the composite objects we know as  
814 jets. The third layer has a thickness of 1.8 interaction lengths, with a segmentation of  
815  $\Delta\eta = 0.2, \Delta\phi = 0.1$ . The use of multiple layers allows one to understand the induced  
816 hadronic shower as it propagates through the detector material.

817 The endcap LAr hadronic calorimeter covers the region  $1.5 < |\eta| < 3.2$ . It is  
818 again a sampling calorimeter; the active material is LAr with a copper absorbed. It  
819 does not use the accordion shape of the other calorimeters; it has a “standard” flat  
820 shape perpendicular to the interaction point. The segmentation varies with  $\eta$ . For  
821  $1.5 < |\eta| < 2.5$ , the cells are  $\Delta\eta = 0.1, \Delta\phi = 0.1$ ; in the region  $2.5 < |\eta| < 3.2$ , the  
822 cells are  $\Delta\eta = 0.2, \Delta\phi = 0.2$  in size.

823 The final calorimeter in ATLAS is the forward LAr calorimeter. Of those  
824 subdetectors which are used for standard reconstruction techniques, the FCal sits  
825 at the most extreme values of  $3.1 < |\eta| < 4.9$ . The FCal itself is made of three  
826 subdetectors; FCal1 is actually an electromagnetic module, while FCal2 and FCal3  
827 are hadronic. The absorber in FCal1 is copper, with a liquid argon active medium.  
828 FCal2 and FCal3 also use a liquid argon active medium, with a tungsten absorber.

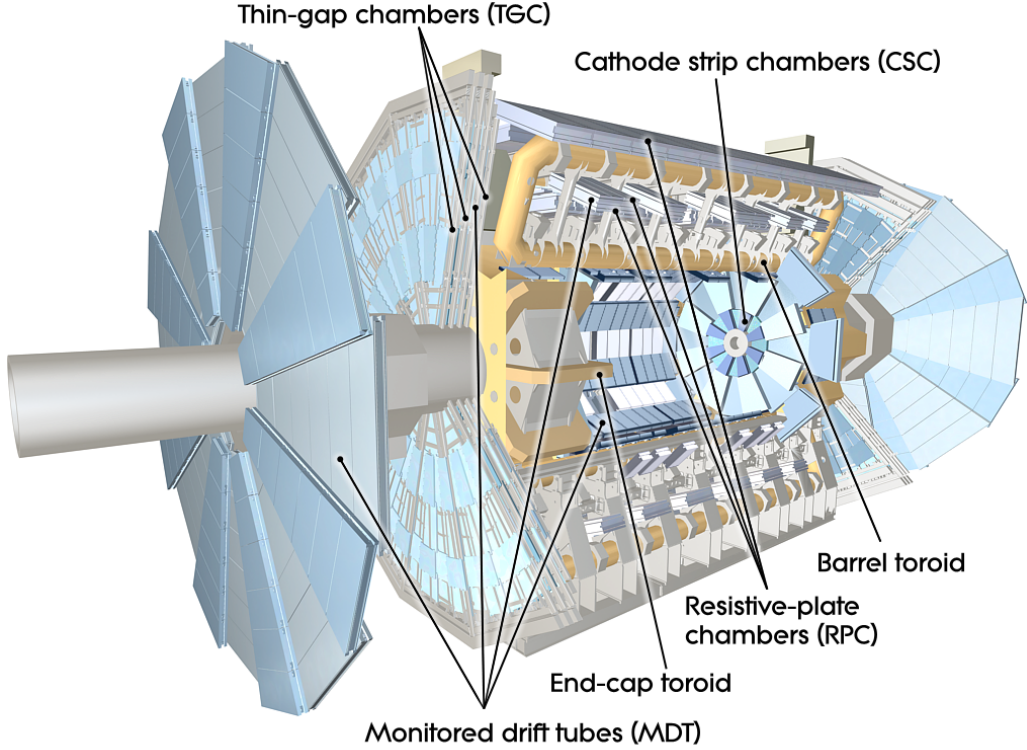


Figure 5.10: The ATLAS muon spectrometer

## 829 5.4 Muon Spectrometer

830 The muon spectrometer is the final major subdetector of the ATLAS detector.  
 831 The muon spectrometer sits outside the hadronic calorimetry, with pseudorapidity  
 832 coverage out to  $|\eta| < 2.7$ . The MS is a huge detector, with some detector elements  
 833 existing as far as 11 m in radius from the interaction point. This system is used  
 834 almost exclusively to measure the momenta of muons; these are the only measured  
 835 SM particles which consistently exit the hadronic calorimeters. These systems provide  
 836 a rough measurement, which is used in triggering (described in Ch.5.5), and a precise  
 837 measurement to be used in offline event reconstruction as described in Ch.???. The  
 838 MS produces tracks in a similar way to the ID; the hits in each subdetector are  
 839 recorded and then tracks are produced from these hits. Muon spectrometer tracks are  
 840 largely independent of the ID tracks due to the independent solenoidal and toroidal  
 841 magnet systems used in the ID and MS respectively. The MS consists of four separate

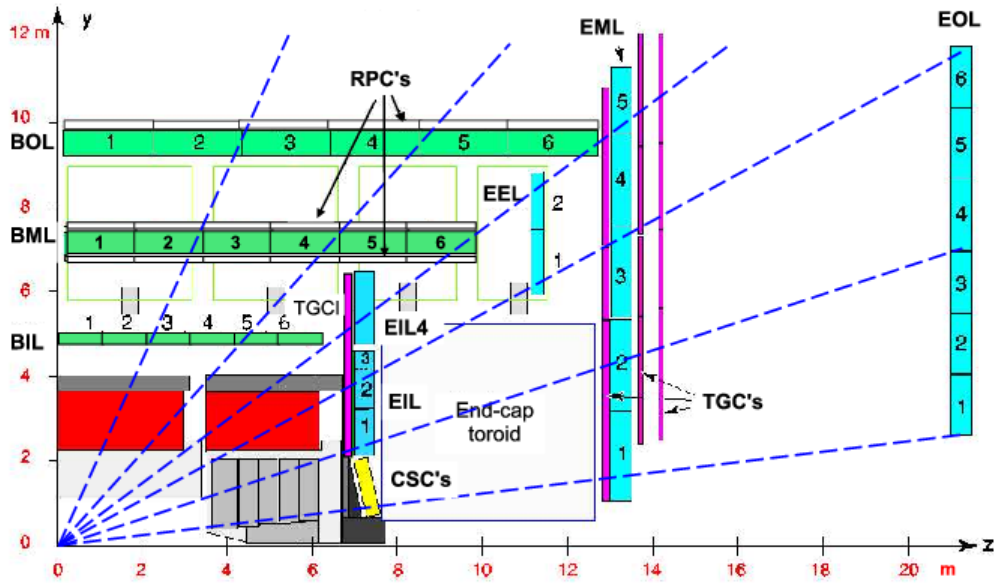


Figure 5.11: A schematic in  $z/\eta$  showing the location of the subdetectors of the muon spectrometer

842 subdetectors: the barrel region is covered by the Resistive Plate Chambers (RPCs)  
 843 and Monitored Drift Tubes (MDTs) while the endcaps are covered by MDTs, Thin  
 844 Gap Chambers (TGCs), and Cathode Strip Chambers (CSCs).

## 845 Monitored Drift Tubes

846 The MDT system is the largest individual subdetector of the MS. MDTs provide  
 847 precision measurements of muon momenta as well as fast measurements used for  
 848 triggers. There are 1088 MDT chambers providing coverage out to pseudorapidity  
 849  $|\eta| < 2.7$ ; each consists of an aluminum tube containing an argon- $\text{CO}_2$  gas mixture.  
 850 In the center of each tube there  $50\mu\text{m}$  diameter tungsten-rhenium wire at a voltage of  
 851 3080 V. A muon entering the tube will induce ionization in the gas, which will “drift”  
 852 towards the wire due to the voltage. One measures this ionization as a current in the  
 853 wire; this current comes with a time measurement related to how long it takes the  
 854 ionization to drift to the wire.

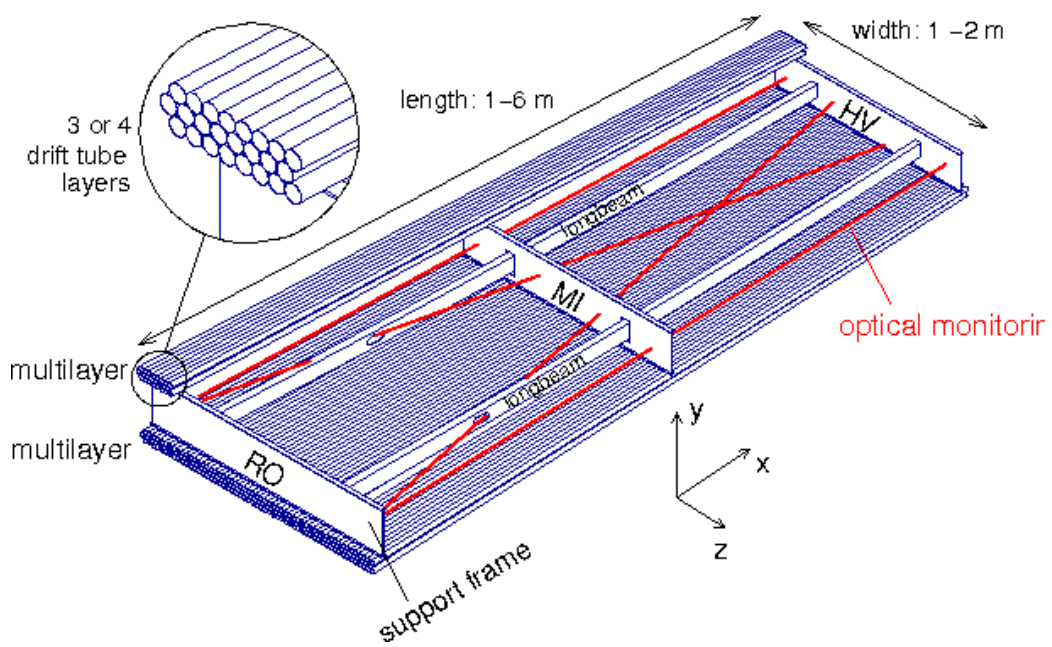


Figure 5.12: Schematic of a Muon Drift Tube chamber

855 These tubes are layered in a pattern shown in Fig.5.12. Combining the measure-  
856 ments from the tubes in each layer gives good position resolution. The system consists  
857 of three subsystems of these layers, at 5 m, 7m, and 9 m from the interaction point.  
858 The innermost layer is directly outside the hadronic calorimeter. The combination of  
859 these three measurements gives precise momenta measurements for muons.

## 860 Resistive Plate Chambers

861 The RPC system is alternated with the MDT system in the barrel; the first two layers  
862 of RPC detectors surround the second MDT layer while the third is outside the final  
863 MDT layer. The RPC system covers pseudorapidity  $|\eta| < 1.05$ . Each RPC consists  
864 of two parallel plates at a distance of 2 mm surrounding a  $\text{C}_2\text{H}_2\text{F}_4$  mixture. The  
865 electric field between these plates is 4.9k kV/mm. Just as in the MDTs, an incoming  
866 muon ionizes the gas, and the deposited ionization is collected by the detector (in this  
867 case on the plates). It is quite fast, but with a relatively poor spatial resolution of  
868 1 cm. Still, it can provide reasonable  $\phi$  resolution due to its large distance from the  
869 interaction point. This is most useful in triggering, where the timing requirements are  
870 quite severe. The RPCs are also complement the MDTs by providing a measurement  
871 of the non-bending coordinate.

## 872 Cathode Strip Chambers

873 The CSCs are used in place of MDTs in the first layer of the endcaps. This region, at  
874  $2.0 < |\eta| < 2.7$ , has higher particle multiplicity at the close distance to the interaction  
875 point from low-energy photons and neutrons. The MDTs were not equip to deal with  
876 the higher particle rate of this region, so the CSCs were designed to deal with this  
877 deficiency.

878 Each CSC consists multiwire proportional chambers, oriented radially outward  
879 from the interaction point. These chambers overlap partially in  $\phi$ . The wires contain



Figure 5.13: Photo of the installation of Cathode Strip Chambers and Monitored Drift Tubes

a gas mixture of argon and CO<sub>2</sub>, which is ionized when muons enter. The detectors operate with a voltage of 1900 V, with much lower drift times than the MDTs. They provide less hits than MDTs, but their lower drift times lower uptime and reduce the amount of detector overload.

The CSCs are arranged into four planes on the wheels of the muon spectrometer, as seen in Fig.???. There are 32 CSCs in total, with 16 on each side of the detector in  $\eta$ .

### Thin Gap Chambers

The TGCs serve the purpose of the RPCs in the endcap at pseudorapidity of  $1.05 < |\eta| < 2.4$ ; they provide fast measurements used in triggering. The TGCs are also multiwire proportional chambers a la the CSCs. The fast readouts necessary for trigger are provided by a high electric field and a small wire-to-wire distance of 1.8 mm. These detectors provide both  $\eta$  and  $\phi$  information, allowing the trigger to use as much information as possible when selecting events.



Figure 5.14: Photo of a muon Big Wheel, consisting of Thin Gap Chambers

## 894 5.5 Trigger System

895 The data rate delivered by the LHC is staggering [89]. In the 2016 dataset, the  
896 collision rate was 40 MHz, meaning a *bunch spacing* of 25 ns. In each of the event,  
897 as we saw in Ch.??, there are many proton-proton collisions. Most of the collisions  
898 are uninteresting, such as elastic scattering of protons, or even inelastic scattering  
899 leading to low-energy dijet events. These types of events have been studied in detail  
900 in previous experiments.

901 Even if one is genuinely interested in these events, it's *impossible* to save all of  
902 the information available in each event. If all events were written "to tape" (as the  
903 jargon goes), ATLAS would store terabytes of data per second. We are limited to only  
904 about 1000 Hz readout by computing processing time and storage space. We thus  
905 implement a *trigger* which provides fast inspection of events to drastically reduce  
906 the data rate from the 40 MHz provided by the LHC to the 1000 Hz we can write to  
907 tape for further analysis.

908       The ATLAS trigger system consists of a two-level trigger, known as the Level-  
909       1 trigger (L1 trigger) and the High-Level Trigger (HLT)<sup>4</sup>. Trigger selections are  
910       organized into *trigger chains*, where events passing a particular L1 trigger are passed  
911       to a corresponding HLT trigger. For example, one would require a particular high- $p_T$   
912       muon at L1, with additional quality requirements at HLT. One can also use HLT  
913       triggers as prerequisites for each other, as is done in some triggers requiring both jets  
914       and  $E_T^{\text{miss}}$ .

915       **Level-1 Trigger**

916       The L1 trigger is hardware-based, and provides the very fast rejection needed to  
917       quickly select events of interest. The L1 trigger uses only what is known as *prompt*  
918       data to quickly identify interesting events. Only the calorimeters and the triggering  
919       detectors (RPCs and TGCs) of the MS are fast enough to be considered at L1,  
920       since the tracking reconstruction algorithms used by the ID and the more precise  
921       MS detectors are very slow. This allows quick identification of events with the  
922       most interesting physical objects : large missing transverse momentum and high-  
923        $p_T$  electrons, muons, and jets.

924       L1 trigger processing is done locally. This means that events are selected without  
925       considering the entire available event. Energy deposits over some threshold are  
926       reconstructed as *regions of interest*. These RoIs are then compared using pattern  
927       recognition hardware to “expected” patterns for the given RoIs. Events with RoIs  
928       matching these expected patterns are then handed to the HLT through the Central  
929       Trigger Processor. This step alone lowers the data rate down by about three orders  
930       of magnitude.

---

<sup>4</sup>In Run1, ATLAS ran with a three-level trigger system. The L1 was essentially as today; the HLT consisted of two separate systems known as the L2 trigger and the Event Filter (EF). This was changed to the simpler system used today during the shutdown between Run1 and Run2.

931 **High-Level Trigger**

932 The HLT performs the next step, taking the incoming data rate from the L1 trigger  
933 of  $\sim 75$  kHz down to the  $\sim 1$  kHz that can be written to tape. The HLT really  
934 performs much like a simplified offline reconstruction, using many common quality  
935 and analysis cuts to eliminate uninteresting events. This is done by using computing  
936 farms located close to the detector, which process events in parallel. Individually, each  
937 event which enters the computing farms takes about 4 seconds to reconstruct; the  
938 HLT reconstruction time also has a long tail, which necessitates careful monitoring  
939 of the HLT to ensure smooth operation.

940 HLT triggers are targetted to a particular physics process, such as a  $E_T^{\text{miss}}$  trigger,  
941 single muon trigger, or multijet trigger. The collection of all triggers is known as  
942 the trigger *menu*. Since many low-energy particles are produced in collisions, it is  
943 necessary to set a *trigger threshold* on the object of interest; this is really just a fancy  
944 naming for a trigger  $p_T$  cut. Due to the changing luminosity conditions of the LHC,  
945 these thresholds change constantly, mostly by increasing thresholds with increasing  
946 instantaneous luminosity. This allows an approximately constant number of events to be  
947 written for further analysis. Triggers which have rates higher than those designated  
948 by the menu are *prescaled*. This means writing only some fraction of the triggered  
949 events. Of course, for physics analyses, one wishes to investigate all data events  
950 passing some set of analysis cuts, so often one uses the “lowest threshold unprescaled  
951 trigger”. *Turn-on curves* allow one to select the needed offline analysis cut to ensure  
952 the trigger is fully efficient. An example turn-on curve for the  $E_T^{\text{miss}}$  triggers used in  
953 the signal region of this analysis is shown in ??.

954 The full set of the lowest threshold unprescaled triggers considered here can be  
955 found in Table 5.1. These are the lowest unprescaled triggers associated to the SUSY  
956 signal models and Standard Model backgrounds considered in this thesis. More  
957 information can be found in [89].

Physics Object	Trigger	$p_T$ (GeV)	Threshold	Level-1 Seed	Additional Requirements	Approximate Rate (Hz)
<b>2015 Data</b>						
$E_T^{\text{miss}}$	HLT_xe70	70	L1_XE50	-	60	
Muon	HLT_mu24_iloose_L1MU15	50	L1_MU15	isolated, loose	130	
Muon	HLT_mu50	50	L1_MU15	-	30	
Electron	HLT_e24_1hmedium_ll2base_L1EM20VH		L1_EM20VH	medium OR isolated, loose	140	
Electron	HLT_e60_1hmedium	60	L1_EM20VH	medium	10	
Electron	HLT_e120_1hloose	120	L1_EM20VH	loose	<10	
Photon	HLT_g120_loose	120	L1_EM20VH	loose	20	
<b>2016 Data</b>						
$E_T^{\text{miss}}$	HLT_xe100_mht_L1XE5000		L1_XE50	-	180	
Muon	HLT_mu24_ivarmedium4	50	L1_MU20	medium	120	
Muon	HLT_mu50	50	L1_MU20	-	40	
Electron	HLT_e24_1htight_noD1ivarloose		L1_EM22VHI	tight with no $d_0$ or loose	110	
Electron	HLT_e60_1hmedium_nd60		L1_EM22VHI	medium with no $d_0$	10	
Electron	HLT_e140_1hloose_noD0		L1_EM22VHI	loose with no $d_0$	<10	
Photon	HLT_g140_loose	140	L1_EM22VHI	loose	20	

Table 5.1: High-Level Triggers used in this thesis. Descriptions of loose, medium, tight, and isolated can be found in [89]. The  $d_0$  cut refers to a quality cut on the vertex position; this was removed from many triggers in 2016 to increase sensitivity to displaced vertex signals. For most triggers, the increased thresholds in 2016 compared to 2016 were designed to keep the rate approximately equal. The exception is the  $E_T^{\text{miss}}$  triggers; see 5.5.

958 **Razor Triggers**

959 For the analysis presented in this thesis, the *razor triggers* were developed. These are  
960 topological triggers, combining both jet and  $E_T^{\text{miss}}$  information to select interesting  
961 events. In particular, they use the razor variable  $M_{\Delta}^R$  which will be described in  
962 Chapter ??.

963 Based on 2015 run conditions, these triggers would have allowed the use of a lower  
964 offline  $E_T^{\text{miss}}$  cut with a similar rate to the nominal  $E_T^{\text{miss}}$  triggers. This can be seen  
965 in the turn-on curves shown in Figure 5.15. The razor triggers are fully efficient at  
966 nearly 100 GeV lower than the corresponding  $E_T^{\text{miss}}$  triggers in  $M_{\Delta}^R$ .

967 There was a quite big change in the 2016 menu, which increased the rate given to  
968  $E_T^{\text{miss}}$  triggers drastically. This can be seen in the difference in rate shown between  
969  $E_T^{\text{miss}}$  triggers in 2015 and 2016 in Table 5.1. This allowed the  $E_T^{\text{miss}}$  triggers to  
970 maintain a lower threshold throughout the dataset used in this thesis.

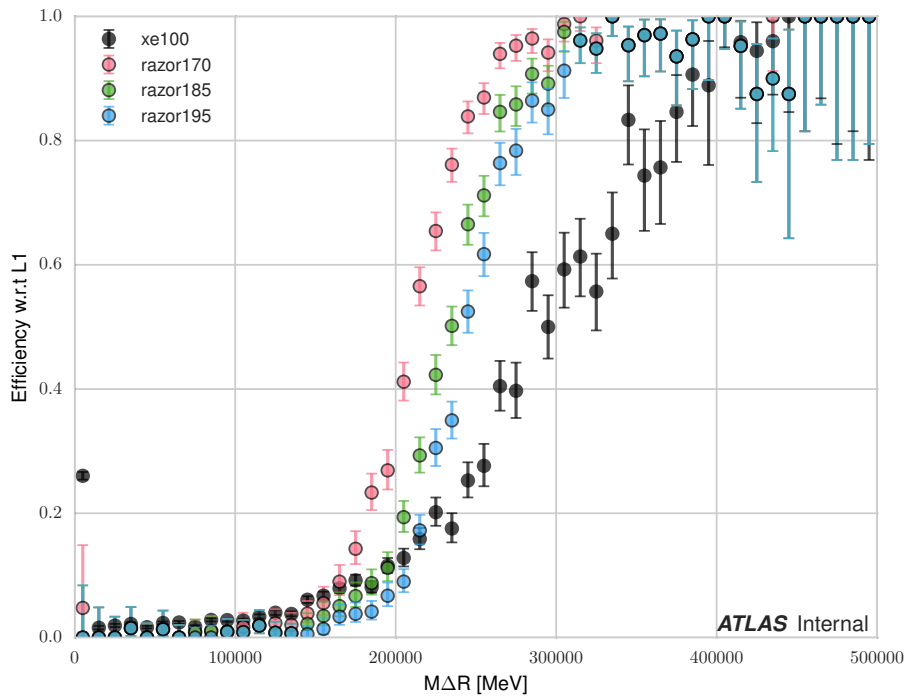
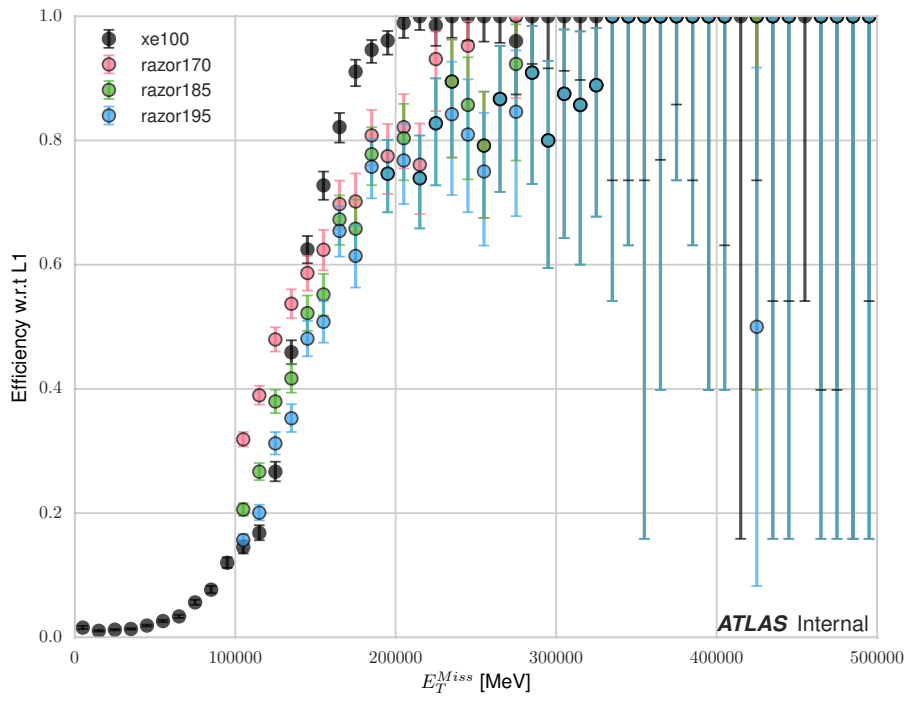


Figure 5.15: Turn-on curves for the razor triggers and nominal  $E_T^{\text{miss}}$  trigger. The razor triggers show a much sharper turn-on in  $M_D^R$  relative to the  $E_T^{\text{miss}}$  trigger. The converse is true for the  $E_T^{\text{miss}}$  triggers.



971

## Chapter 6

---

972

### *Object Reconstruction*

973 This chapter describes the reconstruction algorithms used within ATLAS. We will  
974 make the distinction between the “primitive” objects which are reconstructed from  
975 the detector signals from the “composite” physics objects we use in measurements  
976 and searches for new physics.

977

## 6.1 Primitive Object Reconstruction

978 The primitive objects reconstructed by ATLAS are *tracks* and (calorimeter) *clusters*.  
979 These are reconstructed directly from tracking hits and calorimeter energy deposits  
980 into cells. Tracks can be further divided into inner detector and muon spectrom-  
981 eter tracks. Calorimeter clusters can be divided into sliding-window clusters and  
982 topological clusters (topoclusters).

983

### Inner Detector Tracks

984 Inner detector tracks are reconstructed from hits in the inner detector [90, 91] These  
985 hits indicate that a charged particle has passed through the detector material. Due  
986 to the 2 T solenoid in the inner detector, the hits associated with any individual  
987 particle will be curved. The amount of curvature determines the momentum of the  
988 particle. In any given event, there are upwards of  $10^4$  hits, making it impossible to do  
989 any sort of combinatorics to reconstruct tracks. There are two algorithms used by  
990 ATLAS track reconstruction, known as *inside-out* and *outside-in*.

991     ATLAS first employs the inside-out algorithm. One assumes the track begins  
992 at the interaction point. Moving out from the interaction point, one creates track  
993 seeds. Track seeds are proto-tracks constructed from three hits. These hits can be  
994 distributed as three pixel hits, two pixel hits and one SCT hit, or three SCT hits.  
995 One extrapolates the track and uses a combinatorial Kalman filter[90], which adds  
996 the rest of the pixel and SCT hits to the seeds. This is done seed by seed, so it  
997 avoids the combinatorial complexity involved with checking all hits with all seeds.  
998 At this point, the algorithm applies an additional filter to avoid ambiguities from  
999 nearby tracks. The TRT hits are added to the seeds using the same method. After  
1000 this procedure, all hits are associated to a track.

1001     The next step is to figure out the correct kinematics of the track. This is  
1002 done by applying a fitting algorithm which outputs the best-fit track parameters  
1003 by minimizing the track distance from hits, weighted by each hit's resolution. These  
1004 parameters are  $(d_0, z_0, \eta, \phi, q/p)$  where  $d_0$  ( $z_0$ ) is the transverse (longitudinal) impact  
1005 parameter and  $q/p$  is the charge over the track momenta. This set of parameters  
1006 uniquely defines the measurement of the trajectory of the charged particle associated  
1007 to the track. An illustration of a track with these parameters is shown in Fig.6.1.

1008     The other track reconstruction algorithm is the outside-in algorithm. As the  
1009 name implies, we start from the outside of the inner detector, in the TRT, and  
1010 extend the tracks in toward the interaction point. One begins by seeding from  
1011 TRT hits, and extending the track back towards the center of the detector. The  
1012 same fitting procedure is used as in the inside-out algorithm to find the optimal  
1013 track parameters. This algorithm is particularly important for finding tracks which  
1014 originate from interactions with the detector material, especially the SCT. For tracks  
1015 from primary vertices, this often finds the same tracks as the inside-out algorithm,  
1016 providing an important check on the consistency of the tracking procedure.

1017     In the high luminosity environment of the LHC, even the tracks reconstructed

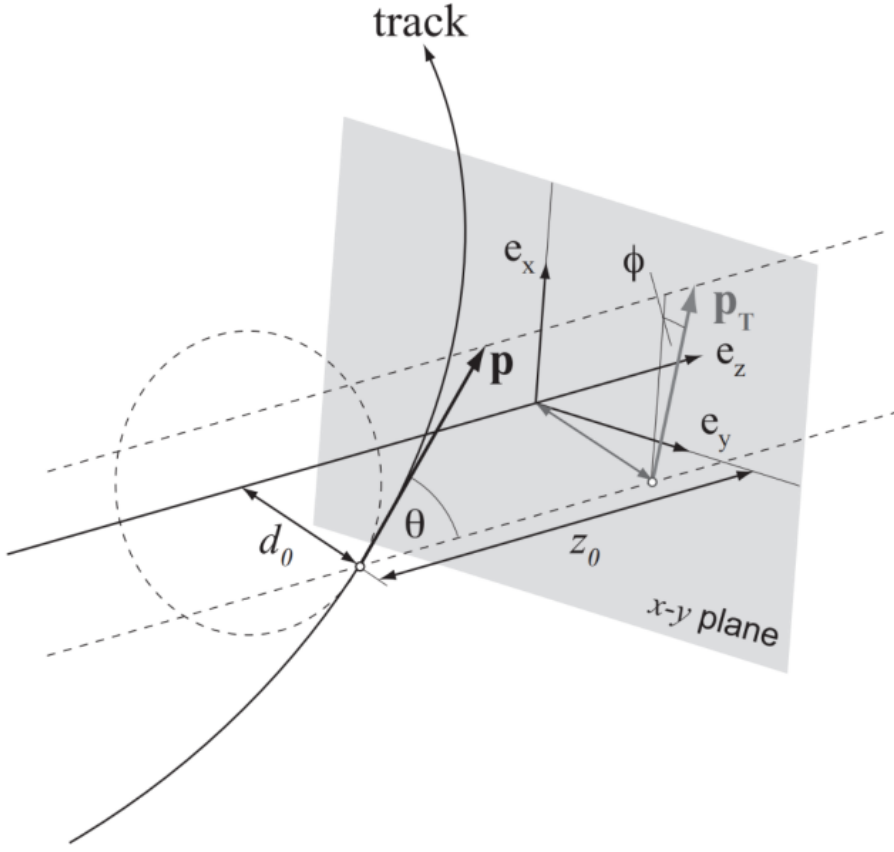


Figure 6.1: The parameters associated to a track.

from precision detectors such as those of ATLAS inner detector can sometimes lead to fake tracks from simple combinatoric chance. Several quality checks are imposed after track fitting which reduce this background. Seven silicon (pixel + SCT) hits are required for all tracks. No more than two *holes* are allowed in the pixel detector. Holes are expected measurements from the track that are missing in the pixel detector. Finally, tracks with poor fit quality, as measured by  $\chi^2/ndf$ , are also rejected. Due to the high quality of the silicon measurements in the pixel detector and SCT, these requirements give good track reconstruction efficiency, as seen in Fig.6.2 for simulated events[92].



(a) Track reconstruction as a function of  $p_T$ . (b) Track reconstruction as a function of  $\eta$ .

Figure 6.2: Track reconstruction efficiency as a function of track  $p_T$  and  $\eta$ . The efficiency is defined as the number of reconstructed tracks divided by the number of generate charged particles.

## 1027 Sliding-window clusters

1028 The sliding-window algorithm is a way to combine calorimeter cells into composite  
 1029 objects (clusters) to be used as inputs for other algorithms[93]. Sliding-window  
 1030 clusters are the primary inputs to electron and photon reconstruction, as described  
 1031 below. The electromagnetic calorimeter has high granularity, with a cell size of  
 1032  $(\eta, \phi) = (.025, .025)$  in the coarsest second layer throughout most of the calorimeter.  
 1033 The “window” consists of 3 by 5 cells in the  $(\eta, \phi)$  space. All layers are added on  
 1034 this same 2D space. One translates this window over the space and seeds a cluster  
 1035 whenever the energy sum of the cells is maximized. If the seed energy is greater  
 1036 than 2.5 GeV, this seed is called a sliding-window cluster. This choice was motivated  
 1037 to optimize the reconstruction efficiency of proto-electrons and proto-photons while  
 1038 rejecting fakes from electronic noise and additional particles from pileup vertices.

1039 **Topological clusters**

1040 Topoclusters are the output of the algorithm used within ATLAS to combine  
1041 hadronic and electromagnetic calorimeter cells in a way which extracts signal from  
1042 a background of significant electronic noise[94]. They are the primary input to the  
1043 algorithms which reconstruct jets.

1044 Topological clusters are reconstructed from calorimeter cells in the following way.  
1045 First, one maps all cells onto a single  $\eta - \phi$  plane so one can speak of *neighboring*  
1046 cells. Two cells are considered neighboring if they are in the same layer and directly  
1047 adjacent, or if they are in adjacent layers and overlap in  $\eta - \phi$  space. The *significance*  
1048  $\xi_{\text{cell}}$  of a cell during a given event is

$$\xi_{\text{cell}} = \frac{E_{\text{cell}}}{\sigma_{\text{noise},\text{cell}}} \quad (6.1)$$

1049 where  $\sigma_{\text{noise},\text{cell}}$  is measured for each cell in ATLAS and  $E_{\text{cell}}$  measures the current  
1050 energy level of the cell. One thinks of this as the measurement of the energy *over*  
1051 *threshold* for the cell.

1052 Topocluster *seeds* are defined as calorimeter cells which have a significance  $\xi_{\text{cell}} >$   
1053 4. These are the inputs to the algorithm. One iteratively tests all cells adjacent  
1054 to these seeds for  $\xi_{\text{cell}} > 2$ . Each cells passing this selection is then added to the  
1055 topocluster, and the procedure is repeated. When the algorithm reaches the point  
1056 where there are no additional adjacent cells with  $\xi_{\text{cell}} > 2$ , every positive-energy cell  
1057 adjacent to the current proto-cluster is added. The collection of summed cells is a  
1058 topocluster. An example of this procedure for a simulation dijet event is shown in  
1059 Fig.6.3.

1060 There are two calibrations used for clusters[95]. These are known as the  
1061 electromagnetic (EM) scale and the local cluster weighting (LCW) scale. The EM  
1062 scale is the energy read directly out of the calorimeters as described. This scale  
1063 is appropriate for electromagnetic processes. The LCW scale applies additional



Figure 6.3: Example of topoclustering on a simulated dijet event.

1064 scaling to the clusters based on the shower development. The cluster energy can be  
1065 corrected for calorimeter non-compensation and the differences in the hadronic and  
1066 electromagnetic calorimeters’ responses. This scale provides additional corrections  
1067 that improve the accuracy of hadronic energy measurements. This thesis only uses  
1068 the EM scale corrections. LCW scaling requires additional measurements that only  
1069 became available with additional data. Due to the jet calibration procedure that  
1070 we will describe below, it is also a relatively complicated procedure to rederive the  
1071 “correct” jet energy.

## 1072 Muon Spectrometer Tracks

1073 Muon spectrometer tracks are fit using the same algorithms as the ID tracks, but  
1074 different subdetectors. The tracks are seeded by hits in the MDTs or CSCs. After  
1075 seeding in the MDTs and CSCs, the hits from all subsystems are refit as the final  
1076 MS track. These tracks are used as inputs to the muon reconstruction, as we will see  
1077 below.

## 1078 6.2 Physics Object Reconstruction and Quality

### 1079 Identification

1080 There are essentially six objects used in ATLAS searches for new physics: electrons,  
1081 photons, muons,  $\tau$ -jets, jets, and  $E_T^{\text{miss}}$ . The reconstruction of these objects is  
1082 described here. In this thesis,  $\tau$  lepton jets are not treated differently from other  
1083 hadronic jets, and we will not consider their reconstruction algorithms. A very  
1084 convenient summary plot is shown in Fig.6.4.

1085 One often wishes to understand “how certain” we are that a particular object  
1086 is truly the underlying physics object. In ATLAS, we often generically consider, in



Figure 6.4: The interactions of particles with the ATLAS detector. Solid lines indicate the particle is interacting with the detector, while dashed lines are shown where the particle does not interact.

1087 order, *very loose*, *loose*, *medium*, and *tight* objects<sup>1</sup>. These are ordered in terms of  
 1088 decreasing object efficiency, or equivalently, decreasing numbers of fake objects. We  
 1089 will also describe briefly the classification of objects into these categories.

1090 In this thesis, since we present a search for new physics in a zero lepton final state,  
 1091 we will provide additional details about jet and  $E_T^{\text{miss}}$  reconstruction.

---

<sup>1</sup> These are not all used for all objects, but it's conceptually useful to think of these different categories.

1092 **Electrons and Photons**

1093 **Reconstruction**

1094 The reconstruction of electrons and photons (often for brevity called “electromagnetic  
1095 objects”) is very similar [93, 96, 97]. This is because the reconstruction begins with  
1096 the energy deposit in the calorimeter in the form of an electromagnetic shower. For  
1097 any incoming  $e/\gamma$ , this induces many more electrons and photons in the shower. The  
1098 measurement in the calorimeter is similar for these two objects.

1099 One begins the reconstruction of electromagnetic objects from the sliding-window  
1100 clusters reconstructed from the EM calorimeter. These  $E > 2.5$  GeV clusters the  
1101 the primary seed for electrons and photons. One then looks for all ID tracks within  
1102  $\Delta R < 0.3$ , where  $\Delta R = \sqrt{\Delta\eta^2 + \Delta\phi^2}$ . We “match” the track and cluster if they are  
1103 within  $\Delta\phi < 0.2$  in the direction of track curvature, or  $\Delta\phi < 0.05$  in the direction  
1104 opposite the track curvature. Those track-cluster seeds with tracks pointing to the  
1105 primary vertex are reconstructed as electrons.

1106 For photons, we have two options to consider, known as *converted* and *unconverted*  
1107 photons. Due to the high energy of the LHC collisions, typical photons have energy  
1108  $>\sim 1$  GeV. At this scale, photons interact almost exclusively via pair-production in  
1109 the presence of the detector material, as shown in Fig.6.5 [56]. If the track-cluster seed  
1110 has a track which does not point at the primary vertex, we reconstruct this object as a  
1111 converted photon. This happens since the photon travels a distance before decay into  
1112 two electrons, and see the tracks coming from this secondary vertex. Those clusters  
1113 which do not have any associated tracks are then reconstruced as an unconverted  
1114 photon.

1115 The final step in electromagnetic object reconstruction is the final energy value  
1116 assigned to these objects. This process is different between electrons and photons due  
1117 to their differing signatures in the EM calorimeter. In the barrel, electrons energies

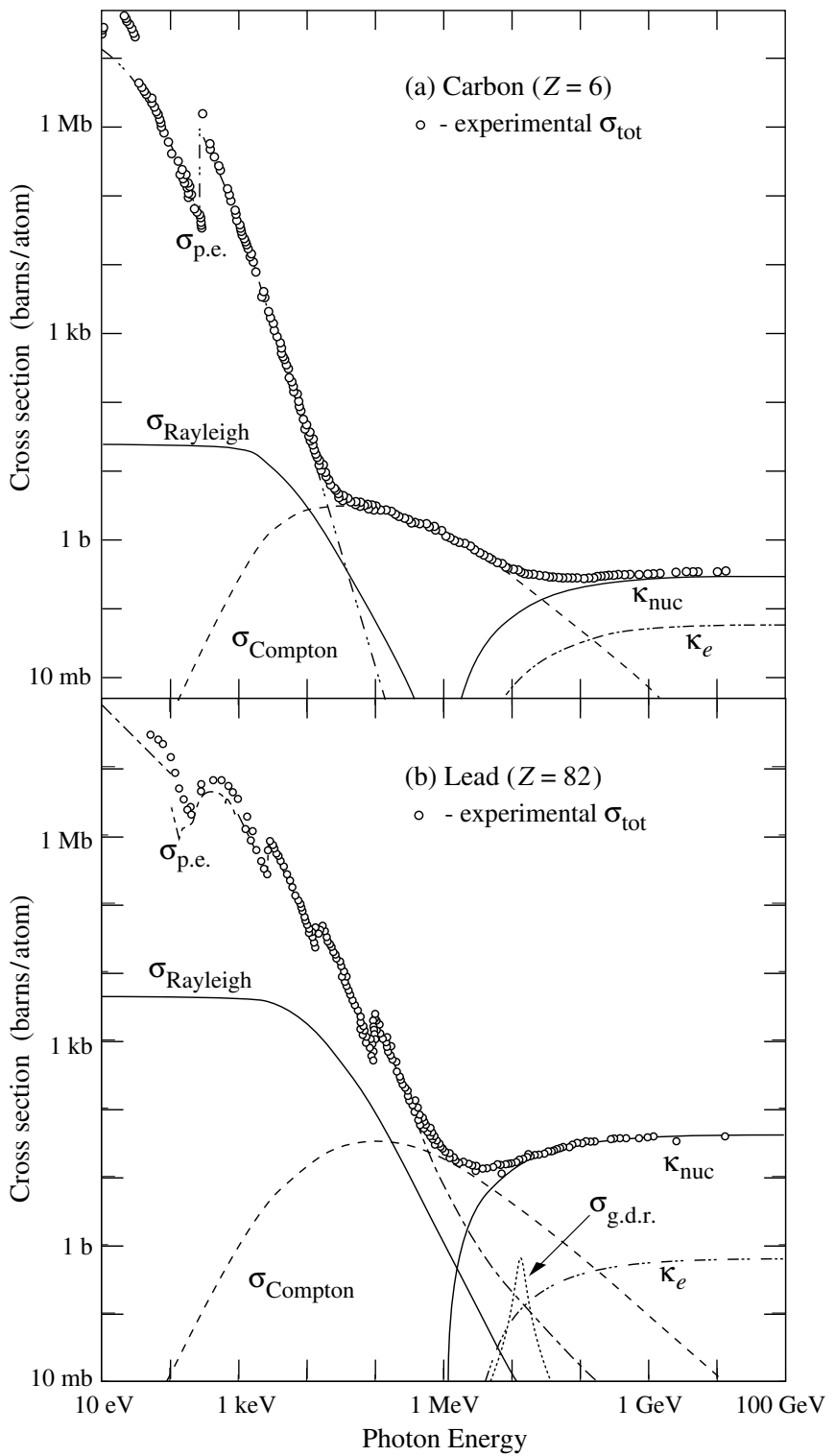


Figure 6.5: Photon total cross sections as a function of energy in carbon and lead, showing the contributions of different processes[56].

1118 are assigned as the sum of the 3 clusters in  $\eta$  and 7 clusters in  $\phi$  to account for the  
1119 electron curving in the  $\phi$  direction. Barrel photons are assigned the energy sum of  
1120 (3, 5) clusters in  $(\eta, \phi)$  space. In the endcap, the effect of the magnetic field on the  
1121 electrons is smaller, and there is a coarser granularity. Both objects sum the (5, 5)  
1122 clusters for their final energy value.

## 1123 Quality Identification

1124 Electrons have a number of important backgrounds which can give fakes. Fake  
1125 electrons come primarily from secondary vertices in hadron decays or misidentified  
1126 hadronic jets. To reduce these backgrounds, quality requirements are imposed on  
1127 electron candidates. Loose electrons have requirements imposed on the shower  
1128 shapes in the electromagnetic calorimeter and on the quality of the associated ID  
1129 track. There is also a requirement that there is a small energy deposition in the  
1130 hadronic calorimeter behind the electron, to avoid jets being misidentified as electrons  
1131 (low hadronic leakage). Medium and tight electrons have increasingly stronger  
1132 requirements on these variables, and additional requirements on the isolation (as  
1133 measured by  $\Delta R$ ) and matching of the ID track momentum and the calorimeter  
1134 energy deposit.

1135 Photons are relatively straightforward to measure, since there are few background  
1136 processes[98]. The primary one is pion decays to two photons, which can cause a jet  
1137 to be misidentified as photon. Loose photons have requirements on the shower shape  
1138 and hadronic leakage. Tight photons have tighter shower shape cuts, especially on  
1139 the high granularity first layer of the EM calorimeter. The efficiency for unconverted  
1140 tight photons as a function of  $p_T$  is shown in

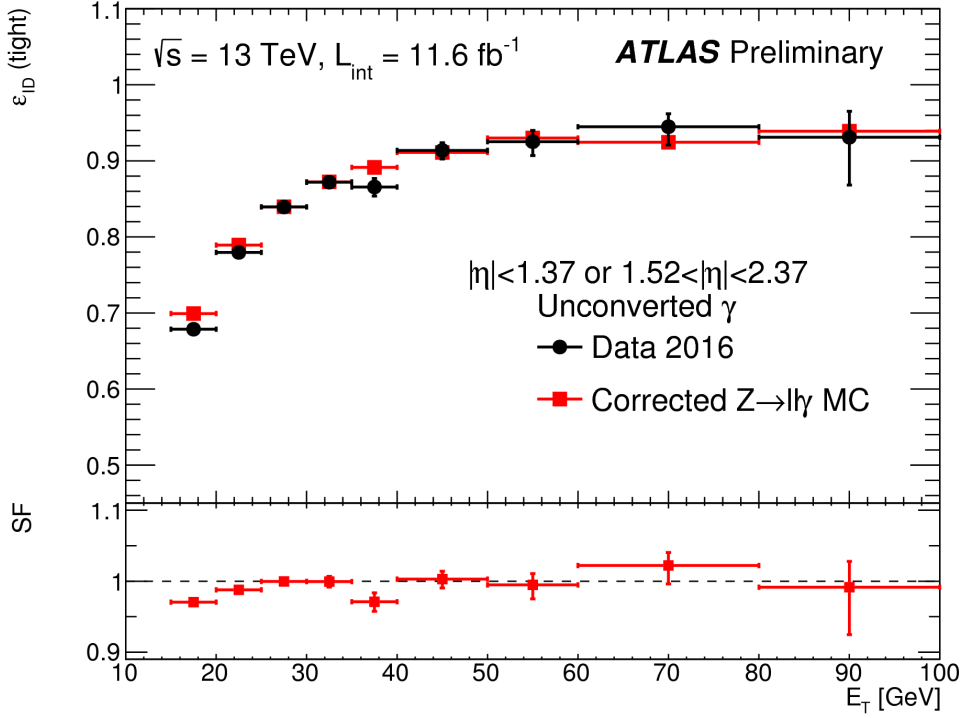


Figure 6.6: Unconverted photon efficiency as measured in [98].

## 1141 Muons

### 1142 Reconstruction

1143 Muons are reconstructed using measurements from all levels of the ATLAS detector[99]. They leave a ID track, a small, characteristic deposition in the EM calorimeter, and then a track in the muon spectrometer. The primary reconstruction technique 1145 produces a so-called *combined* muon. “Combined” means using a combination of the 1146 ID and MS tracks to produce the final reconstructed muon kinematics. This is done 1147 by refitting the hits associated to both tracks, and using this refit track for the muon 1148 kinematics. This process produces the best measured muons, although several other 1149 worse algorithms are used when the full detector information is missing. An example 1150 is in the region  $2.5 < |\eta| < 2.7$  outside the ID acceptance, where MS tracks are used 1151 without the corresponding ID tracks.

1153 **Quality Identification**

Several additional criteria are used to assure muon measurements are free of significant background contributions, especially from pion and kaon decays to muons. Muons produced via these decay processes are often characterized by a “kink”. Candidate muons with a poor fit quality, characterized by  $\chi^2/\text{n.d.f.}$ , are thus rejected. Additionally, the absolute difference in momentum measurements between the ID and MS provide another handle, since the other decay products from hadron decays carry away some amount of the initial hadron momentum. This is measured by

$$\rho' = \frac{|p_T^{\text{ID}} - p_T^{\text{MS}}|}{p_T^{\text{Combined}}}. \quad (6.2)$$

Additionally, there is a requirement on the  $q/p$  significance, defined as

$$S_{q/p} = \frac{|(q/p)^{\text{ID}} - (q/p)^{\text{MS}}|}{\sqrt{\sigma_{\text{ID}}^2 + \sigma_{\text{MS}}^2}}. \quad (6.3)$$

1154 The  $\sigma_{\text{ID,MS}}$  in the denominator of Eq.6.3 are the uncertainties on the corresponding  
1155 quantity from the numerator. Finally, cuts are placed on the number of hits in the  
1156 various detector elements.

1157 Subsequently tighter cuts on these variables allow one to define the different muon  
1158 identification criteria. Loose muons have the highest reconstruction efficiency, but  
1159 the highest number of fake muons, since there are no requirements on the number  
1160 of subdetector hits and the loosest requirements on the suite of quality variables.  
1161 Medium muons consist of Loose muons with tighter cuts on the quality variables.  
1162 They also require more than three MDT hits in at least two MDT layers. These are  
1163 the default used by ATLAS analyses. Tight muons have stronger cuts than those of  
1164 the medium selection, and reducing the reconstruction efficiency. The reconstruction  
1165 efficiency as a function of  $p_T$  can be seen for Medium muons in Fig.6.7.

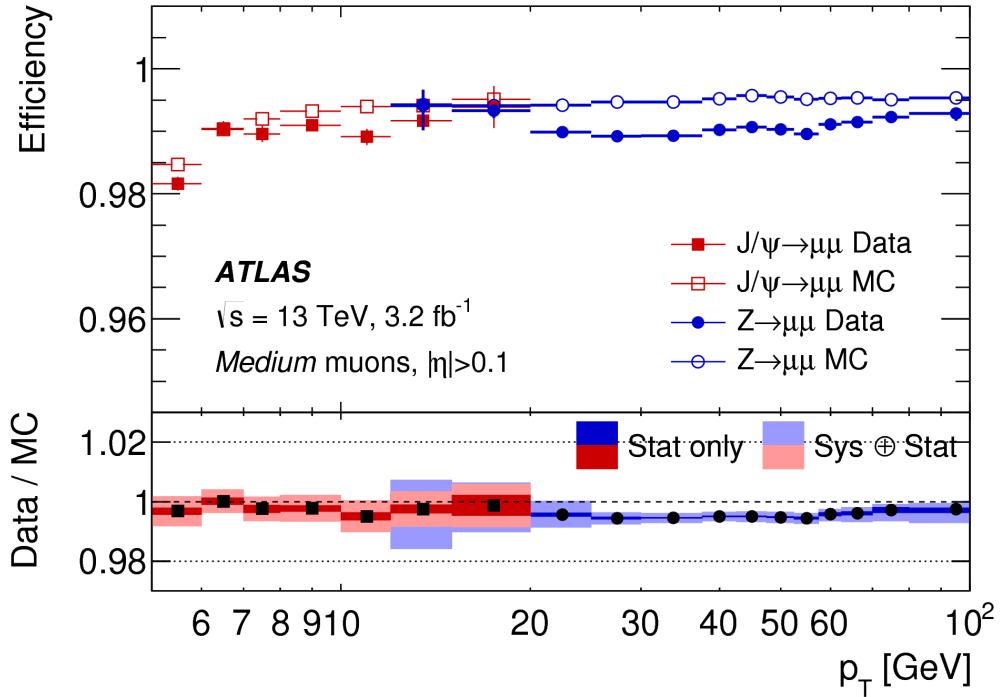


Figure 6.7: Medium muon efficiency as measured in [99].

## 1166 Jets

1167 Jets are composite objects corresponding to many physical particles [56, 100, 101]  
 1168 This is a striking difference from the earlier particles. Fortunately, we normally (and  
 1169 in this thesis) care about the original particle produced in primary collision. In the  
 1170 SM, this corresponds to quarks and gluons. Due to the hadronization process, free  
 1171 quarks and gluons spontaneously hadronize and produce a hadronic shower, which  
 1172 we call a jet. These showers can be measured by the EM and hadronic calorimeters,  
 1173 and the charged portions can be measured in the ID. The first question is how to  
 1174 combine these measurements into a composite object representing the underlying  
 1175 physical parton. This is done via jet algorithms.

1176 **Jet Algorithms**

1177 It might seem straightforward to combine the underlying physical particles into a  
1178 jet. There are three important characteristics required for any jet reconstruction  
1179 algorithm to be used by ATLAS.

- 1180     • Collinear safety - if any particle with four-vector  $p$  is replaced by two particles  
1181       of  $p_1, p_2$  with  $p = p_1 + p_2$ , the subsequent jet should not change  
  
1182     • Radiative (infrared) safety - if any particle with four-vector  $p$  radiates a particle  
1183       of energy  $\alpha \rightarrow 0$ , the subsequent jet should not change  
  
1184     • Fast - the jet algorithm should be “fast enough” to be useable by ATLAS  
1185       computing resources

1186 The first two requirements can be seen in terms of requirements on soft gluon emission.  
1187 Since partons emit arbitrarily soft gluons freely, one should expect the algorithms  
1188 to not be affected by this emission. The final requirement is of course a practical  
1189 limitation.

The algorithms in use by ATLAS (and CMS) which satisfies these requirements are collectively known as the  $k_T$ algorithms [102–104]. These algorithms iteratively combine the “closest” objects, defined using the following distance measures :

$$d_{ij} = \min(k_{T,i}^{2p}, k_{T,j}^{2p}) \frac{\Delta_{ij}^2}{R^2} \quad (6.4)$$
$$d_{iB} = k_{Ti}^{2p}$$

1190 In Eq.6.4,  $k_T, i$  is the transverse momentum of  $i$ -th jet *constituent*,  $\Delta_{ij}$  is the angular  
1191 distance between the constituents. Both  $R$  and  $p$  are adjustable parameters:  $R$  is  
1192 known as the (jet) *cone size* and  $p$  regulates the power of the energy versus the  
1193 geometrical scales. The algorithm sequence, for a given set of objects  $i$  with four-  
1194 vector  $k$  :

- 1195     1. Find the minimum distance in the set of all  $d_{ij}$  and  $d_{iB}$ .

1196     2. If the distance is one of the  $d_{ij}$ , combine the input pair of object  $i, j$  and return  
1197         to (1). If the distance is one of the  $d_{iB}$ , remove the object from the list, call it  
1198         a jet, and return to (1).

1199 This process ends when all objects  $i$  have been added to a jet.

1200 Any choice of  $(p, R)$  has the requirements of collinear and radiative safety. In  
1201 essence, the choice is then to optimize based on speed and the potential for new  
1202 physics discoveries. In ATLAS, we make the choice of  $p = -1$  which is also known  
1203 as the *anti- $k_T$*  algorithm. The choice of  $R = 0.4$  is used for the distance parameter of  
1204 the jets.

1205 The primary “nice” quality of this algorithm can be seen with the following  
1206 example. Consider three inputs to an anti- $k_T$  algorithm, all with  $\eta = 0$  :

- 1207     • Object 1 :  $(p_T, \phi) = (30 \text{ GeV}, 0)$
- 1208     • Object 2 :  $(p_T, \phi) = (20 \text{ GeV}, -0.2)$
- 1209     • Object 3 :  $(p_T, \phi) = (10 \text{ GeV}, 0.2)$
- 1210     • Object 4 :  $(p_T, \phi) = (1 \text{ GeV}, 0.5)$

1211 . In the case shown, it seems natural to first combine the “bigger” objects 1 and 2.  
1212 These then pick up the extra small object 3, and object 4 is not included in the jet.  
1213 This is exactly what is done by the anti- $k_T$  algorithm. The (normal)  $k_T$  algorithm with  
1214  $p = 1$  instead combines the smallest objects, 3 and 4, first. Object 1 and 2 combine  
1215 to form their own jet, instead of these jets picking up object 3. This behavior is not  
1216 ideal due to the effects of pileup, as we will see in the next section.

## 1217 Jet Reconstruction

1218 In ATLAS, jets are reconstructed using multiple different objects as inputs, including  
1219 tracks, “truth” objects, calorimeter clusters, and *particle flow objects* (PFOs). For

1220 physics analyses, ATLAS primarily uses jets reconstructed from calorimeter clusters,  
1221 but we will describe the others here, as they are often used for derivations of  
1222 systematic uncertainties or future prospects.

1223 Calorimeter jets are reconstructed using topoclusters using the anti- $k_T$  algorithm  
1224 with  $R = 0.4$ . The jet reconstruction algorithm is run on the collection of all  
1225 topoclusters reconstructed as in Sec.6.1. Both EM and LCW scale clusters are used  
1226 in the ATLAS reconstruction software and produce two sets of jets for analysis. As  
1227 stated above, this thesis presents an analysis using jets reconstructed using EM scale  
1228 clusters, which we refer to these as *EM jets*.

1229 Tracks can be used as inputs to jet reconstruction algorithms. Jets reconstructed  
1230 from tracks are known as *track jets*. Since the ID tracks do not measure neutral  
1231 objects, these jets measure an incorrect energy. However, these are still useful for  
1232 checks and derivations of systematic uncertainties.

1233 *Truth* jets are reconstructed from *truth* particles. In this case, truth is jargon for  
1234 simulation. In simulation, the actual simulated particles are available and used as  
1235 inputs to the jet reconstruction algorithms. Similarly to track jets, these are not useful  
1236 in and of themselves. Instead, truth jets are used for comparisons and derivations of  
1237 systematic uncertainties.

1238 The last object used as inputs to jet reconstruction algorithms are *particle flow*  
1239 *objects* (PFOs). These are used extensively as the primary input to jet particle  
1240 reconstruction algorithms by the CMS collaboration[105]. Particle flow objects are  
1241 reconstructed by associating tracks and clusters through a combination of angular  
1242 distance measures and detector response measurements to create a composite object  
1243 which contains information from both the ID and the calorimeters. For calorimeter  
1244 clusters which do not have any associated ID track, the cluster is simply the PFO.  
1245 The natural association between tracks and clusters provides easy pileup subtraction  
1246 since tracks are easily associated to the primary vertex. This technique is generally

1247 used in CMS, and ATLAS has been slow to adopt the same. As pileup has increased,  
1248 the utility of using PFOs as inputs to jet reconstruction has increased as well.

1249 **Jet Calibration**

1250 Jets as described in the last section are still *uncalibrated*. Even correcting the cluster  
1251 energies using the LCW does not fully correct the jet energy, due to particles losing  
1252 energy in the calorimeters. The solution to this is the *jet energy scale* (JES). The  
1253 JES is a series of calibrations which on average restore the correct truth jet energy  
1254 for a given reconstructed jet. These steps are shown in Fig.6.8 and described here.

1255 The first step is the origin correction. This adjusts the jet to point at the  
1256 primary vertex. Next, is the jet-area based pileup correction. This step subtracts  
1257 the “average” pileup as measured by the energy density  $\rho$  outside of the jets and  
1258 assumes this is a good approximation for the pileup inside the jet. One then removes  
1259 energy  $\Delta E = \rho \times A_{\text{jet}}$  in this step. The residual pileup correction makes a final offset  
1260 correction by parametrizing the change in jet energy as a function of the number of  
1261 primary vertices  $N_{\text{PV}}$  and the average number of interactions  $\mu$ .

1262 The next step is the most important single correction, known as the AbsoluteEta-  
1263 JES step. Due to the use of non-compensation and sampling calorimeters in ATLAS,  
1264 the measured energy of a jet is a fraction of the true energy of the outgoing parton.  
1265 Additionally, due to the use of different technologies and calorimeters throughout the  
1266 detector, there are directional biases induced by these effects. The correction bins a  
1267 multiplicative factor in  $p_{\text{T}}$  and  $\eta$  which scales the reconstructed jets to corresponding  
1268 truth jet  $p_{\text{T}}$ . This step does not entirely correct the jets, since it is entirely a  
1269 simulation-based approach.

1270 The final steps are known as the global sequential calibration (GSC) and the  
1271 residual in-situ calibration. The GSC uses information about the jet showering shape  
1272 to apply additional corrections based on the expected shape of gluon or quark jets.

1273 The final step is the residual in-situ calibration, which is only applied to data. This  
1274 step uses well-measured objects recoiling off a jet to provide a final correction to the  
1275 jets in data. In the low  $p_T$  region ( $20 \text{ GeV} \sim < p_{T,\text{jet}} \sim < 200 \text{ GeV}$ ),  $Z \rightarrow ll$  events are  
1276 used as a reference object. In the middle  $p_T$  region ( $100 \text{ GeV} \sim < p_{T,\text{jet}} \sim < 600 \text{ GeV}$ ),  
1277 the reference object is a photon, while in the high  $p_T$  region ( $p_{T,\text{jet}} \sim > 200 \text{ GeV}$ ),  
1278 the high  $p_T$  jet is compared to multiple smaller  $p_T$  jets. The reference object is this  
1279 group of multijets. After this final correction, the data and MC scales are identical  
1280 up to the corresponding uncertainties. The combined JES uncertainty as a function  
1281 of  $p_T$  is shown in Fig.6.9.

## 1282 Jet Vertex Tagger

1283 The *jet vertex tagger* (JVT) technique is used to separate pileup jets from those  
1284 associated to the hard primary vertex[106]. The technique for doing so first involves  
1285 *ghost association*[107]. Ghost association runs the anti- $k_T$ jet clustering algorithm on  
1286 a combined collection of the topoclusters and tracks. The tracks *only* momenta are  
1287 set to zero<sup>2</sup>, with only the directional information is included. As discussed above,  
1288 the anti- $k_T$ algorithm is “big to small”; tracks are associated to the “biggest” jet near  
1289 them in  $(\eta, \phi)$ . This method uniquely associates each track to a jet, without changing  
1290 the final jet kinematics.

1291 The JVT technique uses a combination of these track variables to determine the  
1292 likelihood that the jet originated at the primary vertex. For jets which have associated  
1293 tracks from ghost association, this value ranges from 0 (likely pileup jet) to 1 (likely  
1294 hard scatter jet). Jets without associated tracks are assigned  $\text{JVT} = -.1$ . The  
1295 working point of  $\text{JVT} > .59$  is used for jets in this thesis.

---

<sup>2</sup>Well, not exactly zero, since zero momentum tracks wouldn’t have a well-defined  $(\eta, \phi)$  coordinate, but set to a value obeying  $p_{T,\text{track}} << 400 \text{ MeV} = p_{\text{track,min}}$ . This is the minimum momentum for a track to reach the ATLAS inner detector.

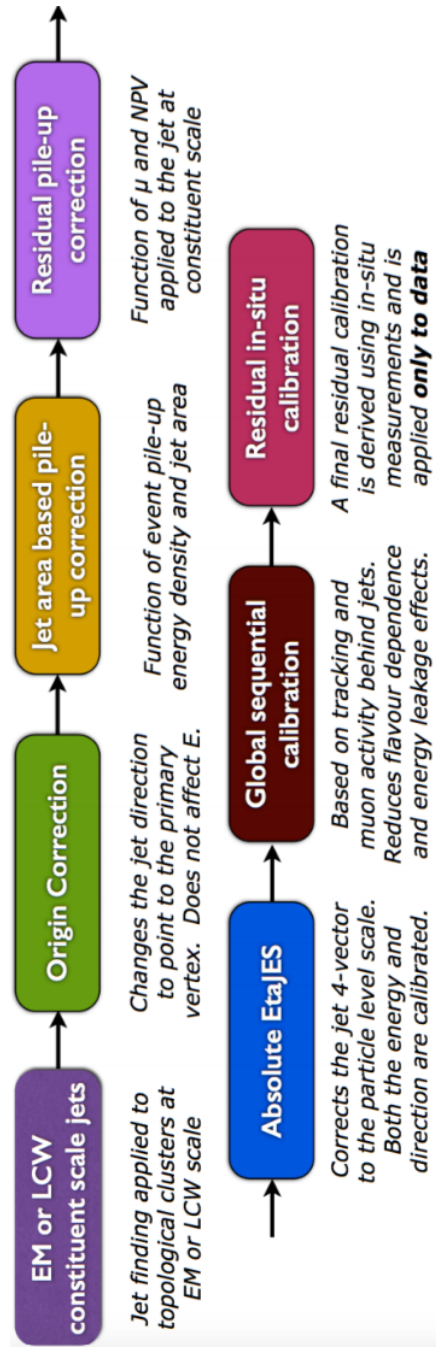


Figure 6.8: The steps used by ATLAS to calibrate jets

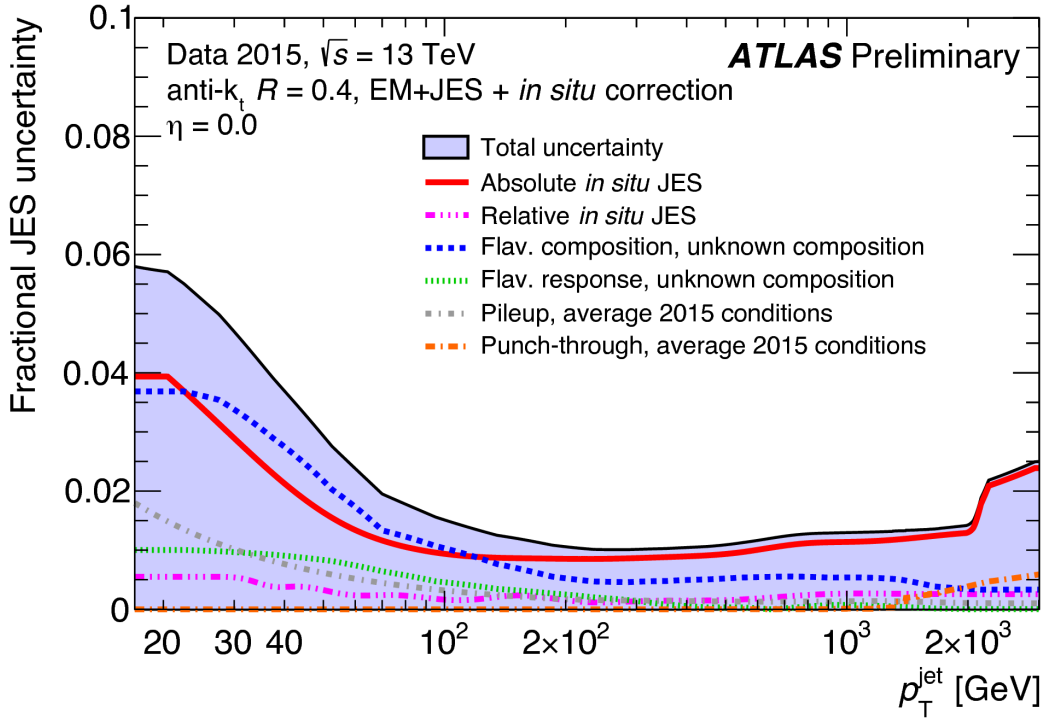


Figure 6.9: Combined jet energy scale uncertainty as a function of  $p_T$  at  $\eta = 0$ .

## 1296 B-jets

1297 Jets originating from bottom quarks (b-jets) are interesting physical phenomena that  
 1298 can be *tagged* by the ATLAS detector[Aad:2015ydr, 108]. B-hadrons, which have  
 1299 a comparatively long lifetime compared to hadrons consisting of lighter quarks, can  
 1300 travel a macroscopic distance inside the ATLAS detector. The high-precision tracking  
 1301 detectors identify the secondary vertices from these decays and the jet matched to  
 1302 that vertex is called a *b-jet*. The “MV2c10” algorithm, based on boosted decision  
 1303 trees, identifies these jets using a combination of variables sensitive to the difference  
 1304 between light-quark and b-quark jets. The efficiency of this tagger is 77%, with a  
 1305 rejection factor of 134 for light-quarks and 6 for charm jets.

## 1306 Missing Transverse Momentum

1307 Missing transverse momentum  $E_T^{\text{miss}}$  [109] is a key observable in searches for new  
1308 physics, especially in SUSY searches[110, 111]. However,  $E_T^{\text{miss}}$  is not a uniquely  
1309 defined object when considered from the detector perspective (as compared to the  
1310 Feynammn diagram), and it is useful to understand the choices that affect the  
1311 performance of this observable in searches for new physics.

### 1312 $E_T^{\text{miss}}$ Definitions

*Hard* objects refers to all physical objects as defined in the previous sections. The  
 $E_T^{\text{miss}}$  reconstruction procedure uses these hard objects and the *soft term* to provide  
a value and direction of the missing transverse momentum. The  $E_{x(y)}^{\text{miss}}$  components  
are calculated as:

$$E_{x(y)}^{\text{miss}} = E_{x(y)}^{\text{miss, } e} + E_{x(y)}^{\text{miss, } \gamma} + E_{x(y)}^{\text{miss, jets}} + E_{x(y)}^{\text{miss, } \mu} + E_{x(y)}^{\text{miss, soft}}, \quad (6.5)$$

1313 where each value  $E_{x(y)}^{\text{miss, } i}$  is the negative vectorial sum of the calibrated objects defined  
1314 in the previous sections.

1315 For purposes of  $E_T^{\text{miss}}$  reconstruction, we must assign an ordering of *overlap*  
1316 *removal*. This is to avoid double counting of the underlying primitive objects (clusters  
1317 and tracks) which are inputs to the reconstruction of the physics objects. We resolve  
1318 this in the following order : electrons, photons , jets and muons. This is motivated  
1319 by the performance of the reconstruction of these objects in the calorimeters.

1320 The soft term  $E_{x(y)}^{\text{miss, soft}}$  contains all of the primitive objects which are not  
1321 associated to any of the reconstructed physics objects. Of course, we need to choose  
1322 which primitive object to use. The primary choices which have been used within  
1323 ATLAS are the *calorimeter-based soft term* (CST) and the *track-based soft term*  
1324 (TST). Based on the soft term choice, we then call  $E_T^{\text{miss}}$  built with a CST (TST)

1325 soft term simply CST (TST)  $E_T^{\text{miss}}$ . An additional option, which will be important  
1326 as pileup continues to increase, particle flow  $E_T^{\text{miss}}$  (PFlow  $E_T^{\text{miss}}$ ).

1327 The CST  $E_T^{\text{miss}}$  was used for much of the early ATLAS data-taking. CST  $E_T^{\text{miss}}$  is  
1328 built from the calibrated hard objects, combined with the calorimeter clusters which  
1329 are *not* assigned to any of those hard objects. In the absence of pileup, it provides the  
1330 best answer for the “true”  $E_T^{\text{miss}}$  in a given event, due to the impressive hermiticity of  
1331 the calorimeters. Unfortunately, the calorimeters do not know “where” from where  
1332 their energy deposition came, and thus CST is susceptible to drastically reduced  
1333 performance as pileup is increased.

1334 TST  $E_T^{\text{miss}}$  is the standard for ATLAS searches as currently performed by ATLAS.  
1335 TST  $E_T^{\text{miss}}$  is built by using the calibrated hard objects and the soft term is built from  
1336 the tracks which are not assigned to any of those hard objects. In particular, due  
1337 to the impressive track-vertex association efficiency, one chooses tracks which only  
1338 come from the primary vertex. This drastically reduces the pileup contributions to  
1339 the  $E_T^{\text{miss}}$  measurement. However, since the ID tracking system is unable to measure  
1340 neutral objects, the TST  $E_T^{\text{miss}}$  is “wrong”. This bias is important to understand for  
1341 many measurements. However, in most searches for new physics, the soft  $E_T^{\text{miss}}$  is  
1342 generally a small fraction of the total  $E_T^{\text{miss}}$ , and thus this bias is not particularly  
1343 hurtful.

1344 PFlow  $E_T^{\text{miss}}$  uses the PFOs described above to build the  $E_T^{\text{miss}}$ . The PFOs which  
1345 are assigned to hard objects are calibrated, and the PFOs which are not assigned  
1346 to any hard object are added to the soft term. In this context, it is convenient to  
1347 distinguish between “charged” and “neutral” PFOs. Charged PFOs can be seen as a  
1348 topocluster which has an associated track, while neutral PFOs do not. This charged  
1349 PFO is essentially a topocluster that we are “sure” comes from the primary vertex.  
1350 The neutral PFOs are in the same status as the original topoclusters. Thus a “full”  
1351 PFlow  $E_T^{\text{miss}}$  should have performance somewhere between TST  $E_T^{\text{miss}}$  and CST  $E_T^{\text{miss}}$ <sup>3</sup>.

1352 A *charged* PFlow  $E_T^{\text{miss}}$  should for sanity be the same as TST.

1353 **Measuring  $E_T^{\text{miss}}$  Performance : event selection**

1354 The question is now straightforward: how do we compare these different algorithms?  
1355 We compare these algorithms in  $Z \rightarrow \ell\ell + \text{jets}$  and  $W \rightarrow \ell\nu + \text{jets}$  events. Due to  
1356 the presence of leptons, these events are well-measured “standard candles”. Here  
1357 we present the results in early 2015 data with  $Z \rightarrow \mu\mu$  and  $W \rightarrow e\nu$  events, as  
1358 shown in [112, 113]. This result was important to assure the integrity of the  $E_T^{\text{miss}}$   
1359 measurements at the higher energy and pileup environment of Run-2.

1360 The  $Z \rightarrow \ell\ell$  selection is used to measure the intrinsic  $E_T^{\text{miss}}$  resolution of the  
1361 detector. The only possible source of neutrinos in these decays is from heavy-flavor  
1362 decays inside of jets, and thus  $Z \rightarrow \ell\ell$  events they have very low  $E_T^{\text{miss}}$ . This provides  
1363 an ideal event topology to understand the modelling of  $E_T^{\text{miss}}$  mismeasurement.  
1364 Candidate  $Z \rightarrow \mu\mu$  events are first required to pass a muon or electron trigger, as  
1365 described in Table 5.1. Offline, the selection of  $Z \rightarrow \mu\mu$  events requires exactly two  
1366 medium muons. The muons are required to have opposite charge and  $p_T > 25 \text{ GeV}$ ,  
1367 and mass of the dimuon system is required to be consistent with the  $Z$  mass  
1368  $|m_{ll} - m_Z| < 25 \text{ GeV}$ .

$W \rightarrow \ell\nu$  events are an important topology to evaluate the  $E_T^{\text{miss}}$  modelling in  
an event with real  $E_T^{\text{miss}}$ . This  $E_T^{\text{miss}}$  is from the neutrino, which is not detected.  
The  $E_T^{\text{miss}}$  in these events has a characteristic distribution with a peak at  $\frac{1}{2}m_W$ . The  
selection of  $W \rightarrow e\nu$  events begins with the selection of exactly one electron of medium  
quality. A selection on TST  $E_T^{\text{miss}} > 25 \text{ GeV}$  drastically reduces the background from  
multijet events where the jet fakes an electron. The transverse mass is used to select

---

<sup>3</sup>Naively, due to approximate isospin symmetry, about 2/3 of the hadrons will be charged and 1/3 will be neutral.

the  $W \rightarrow e\nu$  events :

$$m_T = \sqrt{2p_T^\ell E_T^{\text{miss}}(1 - \cos \Delta\phi)}, \quad (6.6)$$

1369 where  $\Delta\phi$  is the difference in the  $\phi$  between the  $E_T^{\text{miss}}$  and the electron.  $m_T$  is required  
1370 to be greater than 50 GeV.

1371 There are two main ingredients to investigate : the  $E_T^{\text{miss}}$  resolution and the  $E_T^{\text{miss}}$   
1372 scale.

1373 **Measuring  $E_T^{\text{miss}}$  Performance in early 2015 data : metrics**

1374 To compare these algorithms we use the  $E_T^{\text{miss}}$  resolution,  $E_T^{\text{miss}}$  scale, and the  
1375 linearity. Representative distributions of TST  $E_x^{\text{miss}}$ ,  $E_y^{\text{miss}}$ , and  $E_T^{\text{miss}}$  from early  
1376 2015 datataking are shown in Fig.6.10.

The  $E_T^{\text{miss}}$  resolution is an important variable due to the fact that the bulk of the distributions associated to  $E_{x(y)}^{\text{miss}}$  are Gaussian distributed [Aad2012]. However, to properly measure the tails of this distribution, especially when considering non-calorimeter based soft terms, it is important to use the root-mean square as the proper measure of the resolution. This is strictly larger than a resolution as measured using a fit to a Gaussian, due to the long tails from i.e. track mismeasurements. The resolution is measured with respect to two separate variables :  $\sum E_T$  and  $N_{\text{PV}}$ .  $\sum E_T$  is an important measure of the “total event activity”. It is defined as

$$\sum E_T = \sum p_T^e + \sum p_T^\gamma + \sum p_T^\tau + \sum p_T^{\text{jets}} + \sum p_T^\mu + \sum p_T^{\text{soft}}. \quad (6.7)$$

1377 The measurement as a function of  $N_{\text{PV}}$  is useful to understand the degradation of  
1378  $E_T^{\text{miss}}$  performance with increasing pileup. Figure 6.11 shows the  $E_T^{\text{miss}}$  resolution in  
1379 the early 2015 data. The degradation of the  $E_T^{\text{miss}}$  performance is shown as a function  
1380 of pileup  $N_{\text{PV}}$  and total event activity  $\sum E_T$ .

Another important performance metric is the  $E_T^{\text{miss}}$  scale, or how “right” we are in our  $E_T^{\text{miss}}$  calculation. This can be off in various directions, as CST  $E_T^{\text{miss}}$  contains

additional particles from pileup, while soft neutral particles<sup>4</sup> are ignored by TST  $E_T^{\text{miss}}$ .

To measure this in data, we again use  $Z \rightarrow \mu\mu$  events, where the  $Z \rightarrow \mu\mu$  system is treated as a well-measured reference object. The component of  $E_T^{\text{miss}}$  which is in the same direction as the reconstructed  $Z \rightarrow \mu\mu$  system is sensitive to potential biases in the detector response. The unit vector  $\mathbf{A}_Z$  of the  $Z$  system is defined as

$$\mathbf{A}_Z = \frac{\vec{p}_T^{\ell^+} + \vec{p}_T^{\ell^-}}{|\vec{p}_T^{\ell^+} + \vec{p}_T^{\ell^-}|}, \quad (6.8)$$

where  $\vec{p}_T^{\ell^+}$  and  $\vec{p}_T^{\ell^-}$  are the transverse momenta of the leptons from the  $Z$  boson decay. The relevant scale metric is then the mean value of the  $\vec{E}_T^{\text{miss}}$  projected onto  $\mathbf{A}_Z$  :  $\langle \vec{E}_T^{\text{miss}} \cdot \mathbf{A}_Z \rangle$ . In Figure 6.12, the scale is shown for the early 2015 dataset. The negative bias, which is maximized at about 5 GeV, is a reflection of two separate effects. The soft neutral particles are missed by the tracking system, and thus ignored in TST  $E_T^{\text{miss}}$ . Missed particles due to the limited ID acceptance can also affect the scale.

For events with real  $E_T^{\text{miss}}$ , one can also look at the *linearity* in simulation. This is defined as

$$\text{linearity} = \left\langle \frac{E_T^{\text{miss}} - E_T^{\text{miss,Truth}}}{E_T^{\text{miss,Truth}}} \right\rangle. \quad (6.9)$$

$E_T^{\text{miss,Truth}}$  refers to “truth” particles as defined before, or the magnitude of the vector sum of all noninteracting particles. The linearity is expected to be zero if the  $E_T^{\text{miss}}$  is reconstructed at the correct scale.

## 1391 Particle Flow Performance

As described above, the resolution, scale, and linearity are the most important metrics to understand the performance of the different  $E_T^{\text{miss}}$  algorithms. In this section, we present comparisons of the different algorithms, including particle flow, in simulation

---

<sup>4</sup>“Soft” here means those particles which are not hard enough to be reconstructed as their own particle, using the reconstruction algorithms above.

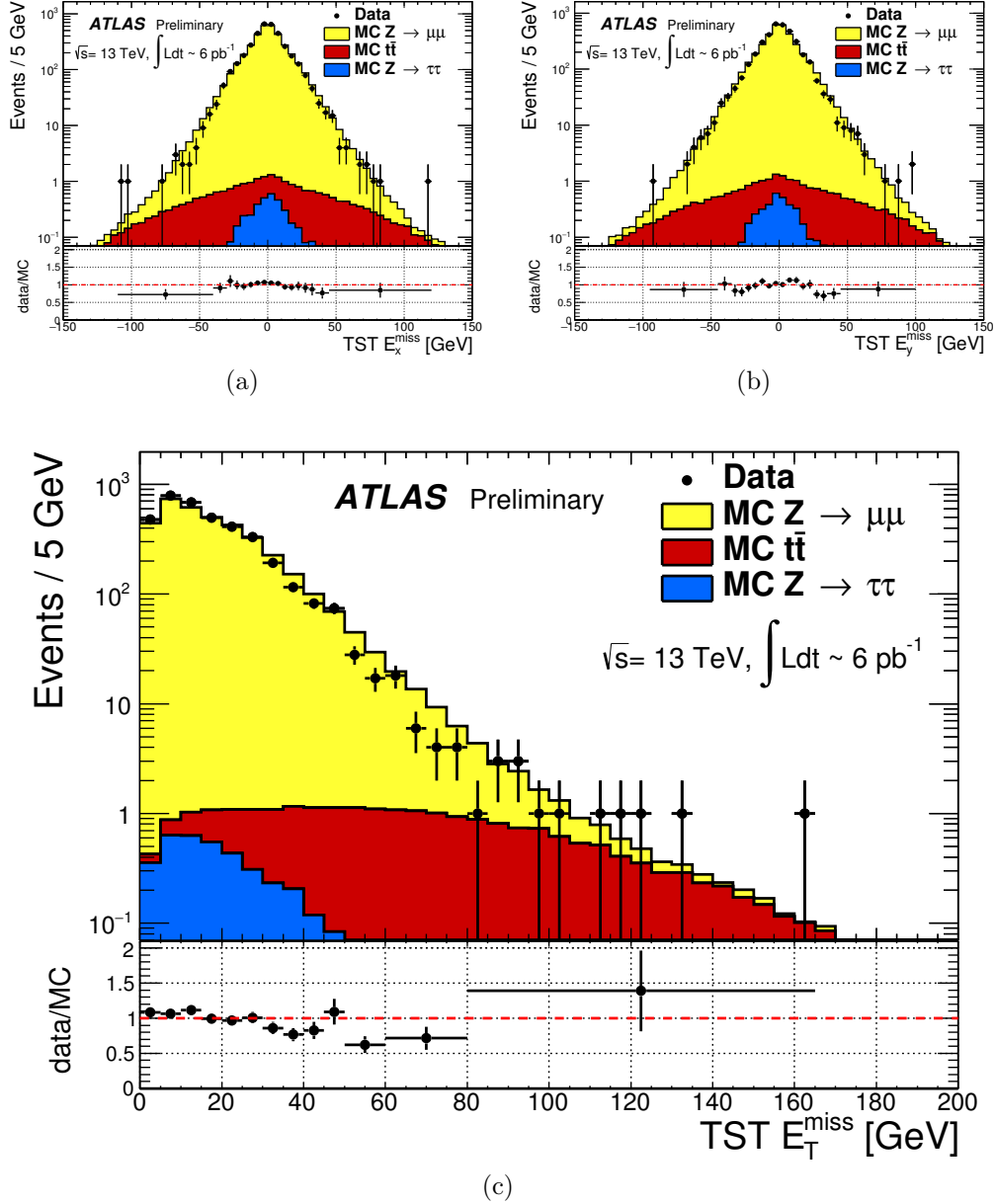


Figure 6.10: TST  $E_x^{\text{miss}}$ ,  $E_y^{\text{miss}}$ , and  $E_T^{\text{miss}}$  distributions of early  $\sqrt{s} = 13$  TeV data compared with simulation after the  $Z \rightarrow \mu\mu$  selection described in Sec. 6.2. The data sample consists of  $6 \text{ pb}^{-1}$ .

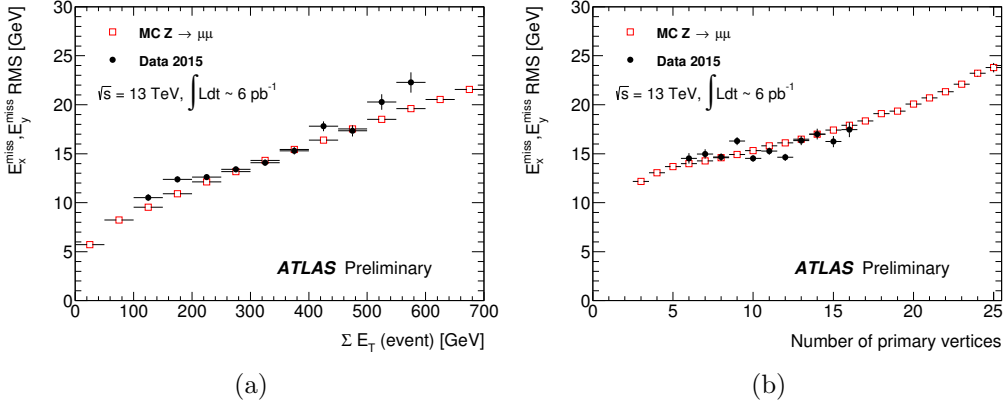


Figure 6.11: Resolution of TST  $E_T^{\text{miss}}$  of early  $\sqrt{s} = 13$  TeV data compared with simulation after the  $Z \rightarrow \mu\mu$  selection described in Sec.6.2. The data sample consists of  $6 \text{ pb}^{-1}$ .

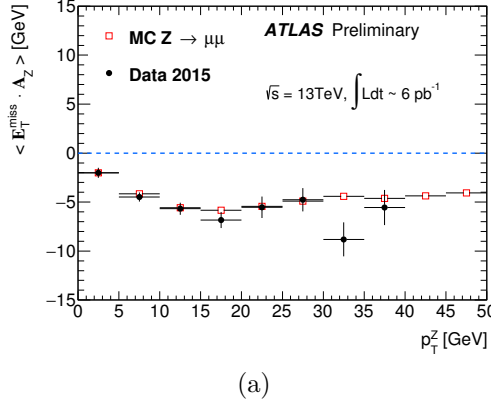


Figure 6.12: Scale of TST  $E_T^{\text{miss}}$  of early  $\sqrt{s} = 13$  TeV data compared with simulation after the  $Z \rightarrow \mu\mu$  selection described in Sec.6.2. The data sample consists of  $6 \text{ pb}^{-1}$ .

1395 and using a data sample from 2015 of  $80 \text{ pb}^{-1}$ . In these plots, ‘‘MET\_PFlow-TST’’  
1396 refers to charged PFlow  $E_T^{\text{miss}}$ , while the other algorithms are as described above.

1397 Figures ?? show the resolution and scale in simulated  $Z \rightarrow \mu\mu$  events. The  
1398 resolution curves follow the ‘‘intuitive’’ behavior discussed before. Due to the high  
1399 pileup in 2015 run conditions, the CST  $E_T^{\text{miss}}$  resolution is poor, and becomes even  
1400 poorer with increasing pileup and event activity. The ‘‘regular’’ PFlow  $E_T^{\text{miss}}$  shows  
1401 reduces pileup and event activity dependence as compared to the CST. As stated  
1402 earlier, the  $E_T^{\text{miss}}$  from the PFlow algorithm can be seen as a hybrid of TST  $E_T^{\text{miss}}$

1403 and CST  $E_T^{\text{miss}}$ . The charged PFOs ( $\sim 2/3$ ) are pileup suppressed, while the neutral  
1404 PFOs (or topoclusters) are not. Both charged PFlow and TST  $E_T^{\text{miss}}$  show only a  
1405 small residual dependence on  $N_{\text{PV}}$  and  $\sum E_T$ , since they have fully pileup suppressed  
1406 inputs through the track associations.

1407 The scale plots are shown for  $Z + \text{jets}$  events and  $Z$  events with no jets. For the  
1408 nonsuppressed CST, the scale continues to worsen with increasing  $p_T^Z$ . It is almost  
1409 always the worst performing algorithm. The standard PFlow algorithm performs the  
1410 second worst in the region of high  $p_T^Z$ , but is the best at low  $p_T^Z$ . The most exciting note  
1411 in this plot is the improved scale of the charged PFlow  $E_T^{\text{miss}}$  compared to the TST  
1412  $E_T^{\text{miss}}$ . Considering the resolution is essentially identical, the PFlow algorithm is better  
1413 picking up the contributions from additional neutral particles. In events with no jets,  
1414 the soft term is essentially the only indication of the  $E_T^{\text{miss}}$  mismeasurement, since  
1415 the muons will be well-measured. In this case, the pileup effects cancel, on average,  
1416 due to the  $U(1)_\phi$  symmetry of the ATLAS detector, and CST performs rather well  
1417 compared to the more complicated track-based algorithms. The full PFlow algorithm  
1418 performs best, since it provides a small amount of pileup suppression on the neutral  
1419 components from CST.

1420 The resolution and linearity are shown in simulated  $W \rightarrow e\nu$  events in Figure ???.  
1421 The resolution in  $W \rightarrow e\nu$  events shows a similar qualitative behavior to that shown  
1422 in  $Z \rightarrow \mu\mu$  events. The CST  $E_T^{\text{miss}}$  has the worst performance, with charged PFlow  
1423  $E_T^{\text{miss}}$  performing best. The surprise here is that the scale associated to TST  $E_T^{\text{miss}}$  in  
1424 these events is best throughout the space parameterized by  $E_T^{\text{miss,Truth}}$ , except for one  
1425 bin at  $40 \text{ GeV} < E_T^{\text{miss,Truth}} < 50 \text{ GeV}$ . The scale in these events is best measured  
1426 using a track-based soft term.

1427 The resolution also investigated in real data passing the  $Z \rightarrow \mu\mu$  selection  
1428 described above. A comparison of the  $E_T^{\text{miss}}$  between real data and simulation for  
1429 each algorithm is presented in Figure 6.16. The resolution as a function of  $\sum E_T$  and

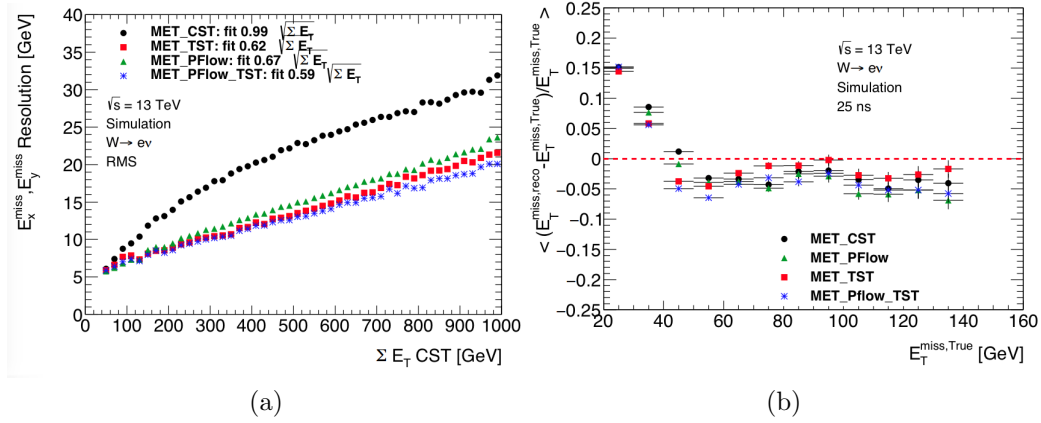


Figure 6.13: Comparison of  $E_T^{\text{miss}}$  resolution and linearity using different  $E_T^{\text{miss}}$  algorithms with simulated  $W \rightarrow e\nu$  events.

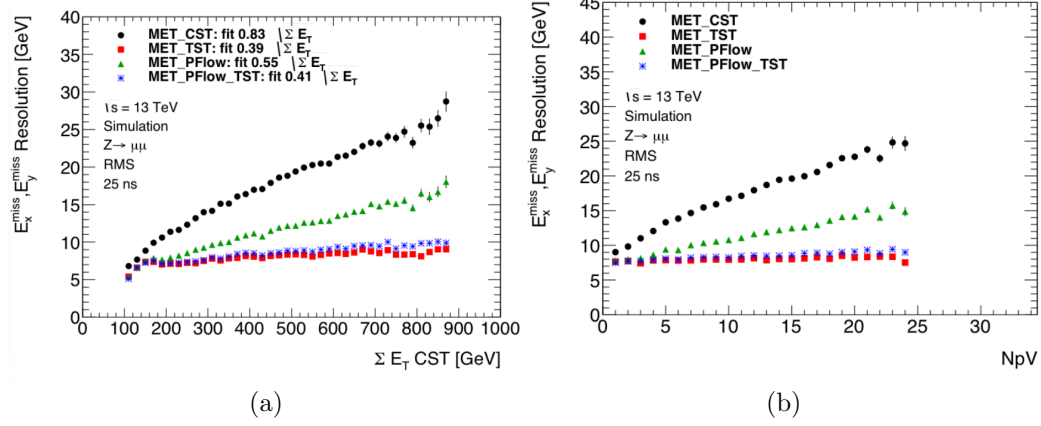


Figure 6.14: Comparison of  $E_T^{\text{miss}}$  resolution using different  $E_T^{\text{miss}}$  algorithms with simulated  $Z \rightarrow \mu\mu$  events.

1430  $N_{\text{PV}}$  is shown in Figure 6.17 for this dataset. Overall, this plot shows the same general  
 1431 features as the simulation dataset in terms of algorithm performance. However, the  
 1432 performance of all algorithms seems to be significantly worse in data. This is likely due  
 1433 to simplifications made in the simulation: soft interactions that cannot be simulated  
 1434 can have a significant effect on an event level variable such as the  $E_T^{\text{miss}}$  resolution.

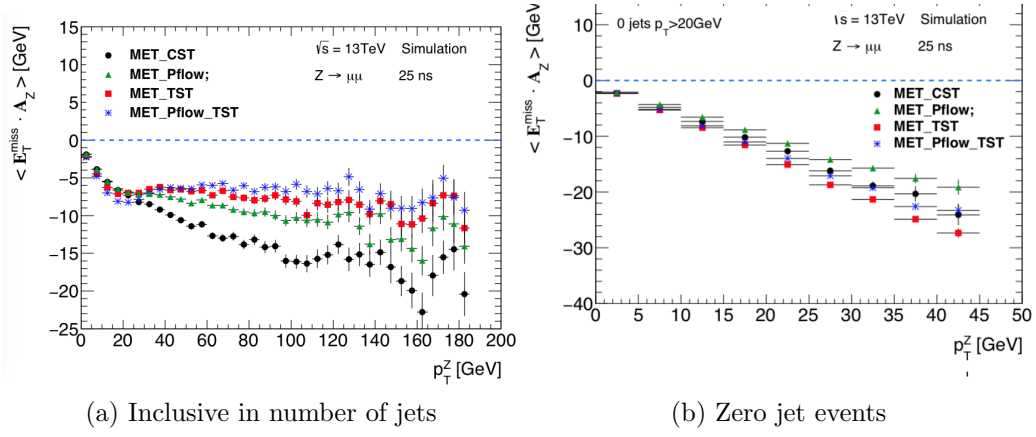


Figure 6.15: Comparison of  $E_T^{\text{miss}}$  scale using different  $E_T^{\text{miss}}$  algorithms with simulated  $Z \rightarrow \mu\mu$  events.

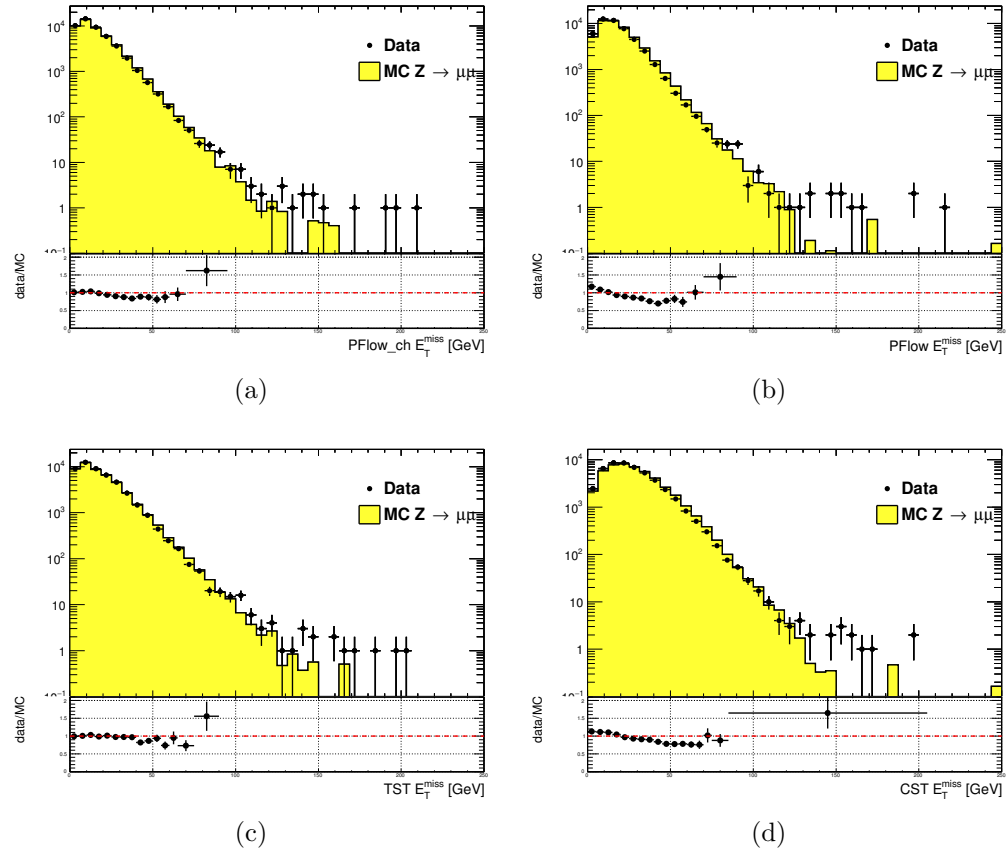


Figure 6.16: Comparison of  $E_T^{\text{miss}}$  distributions using different  $E_T^{\text{miss}}$  algorithms with a data sample of  $80 \text{ pb}^{-1}$  after the  $Z \rightarrow \mu\mu$  selection described in Sec.6.2

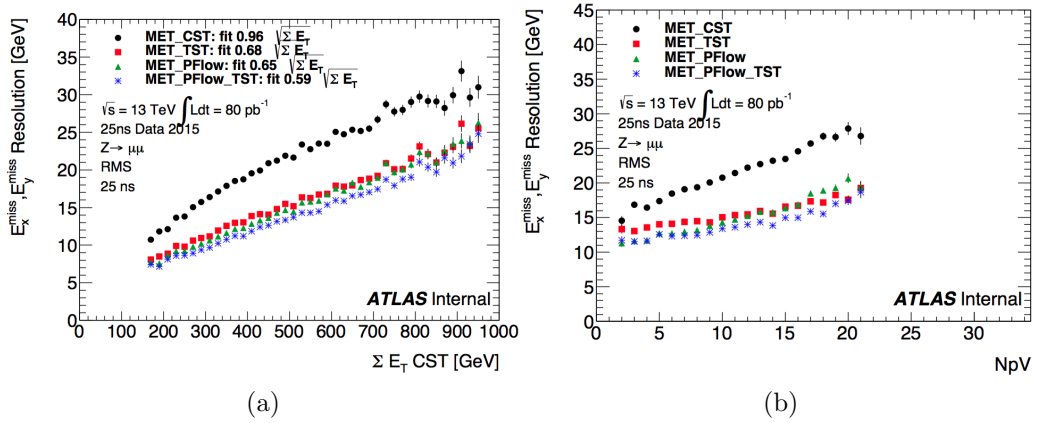


Figure 6.17: Comparison of  $E_T^{\text{miss}}$  resolution using different  $E_T^{\text{miss}}$  algorithms with a data sample of  $80 \text{ pb}^{-1}$  after the  $Z \rightarrow \mu\mu$  selection described in Sec.6.2

## *Recursive Jigsaw Reconstruction*

1437 *Recursive Jigsaw Reconstruction* (RJR) [Jackson:2016mfb,  
1438 **ATLAS-CONF-2016-078**] is a novel algorithm used for the analysis presented  
1439 in this thesis. This technique is the conceptual successor to the razor technique  
1440 [**Rogan:2010kb**, **Buckley:2013kua**], which has been used successfully in many  
1441 new physics searches [37, 38, 40, 41, 47, 114].

### 1442 **7.1 Razor variables**

1443 By using the asterisk to start a new section, I keep the section from appearing in the  
1444 table of contents. If you want your sections to be numbered and to appear in the  
1445 table of contents, remove the asterisk.

### 1446 **7.2 SuperRazor variables**

### 1447 **7.3 Recursive Jigsaw Reconstruction**

1448 The algorithm proceeds by the imposition of a particular *decay tree*, which corre-  
1449 sponds to a simplified Feynmann diagram. At each step in this decay tree, we can  
1450 calculate variables of interest, through a series of simplifying assumptions. In order  
1451 to

<sub>1452</sub> **7.4 Variables used in the search for zero lepton**

<sub>1453</sub> **SUSY**

1454

## Chapter 8

---

1455

*Title of Chapter 1*



1456

## Chapter 9

---

1457

### *Title of Chapter 1*

1458 Here you can write some introductory remarks about your chapter. I like to give each  
1459 sentence its own line.

1460 When you need a new paragraph, just skip an extra line.

1461 **9.1 Object reconstruction**

1462 **Photons, Muons, and Electrons**

1463 **Jets**

1464 **Missing transverse momentum**

1465 Probably longer, show some plots from the PUB note that we worked on

1466 **9.2 Signal regions**

1467 **Gluino signal regions**

1468 **Squark signal regions**

1469 **Compressed signal regions**

1470 **9.3 Background estimation**

1471 **Z vv**

1472 **W ev**

1473 **ttbar**

1474

## Chapter 10

---

1475

### *Title of Chapter 1*

1476 Here you can write some introductory remarks about your chapter. I like to give each

1477 sentence its own line.

1478 When you need a new paragraph, just skip an extra line.

## 1479 **10.1 Statistical Analysis**

1480 maybe to be moved to an appendix

## 1481 **10.2 Signal Region distributions**

## 1482 **10.3 Pull Plots**

## 1483 **10.4 Systematic Uncertainties**

## 1484 **10.5 Exclusion plots**



---

1485

## *Conclusion*

1486 Here you can write some introductory remarks about your chapter. I like to give each  
1487 sentence its own line.

1488 When you need a new paragraph, just skip an extra line.

1489 **10.6 New Section**

1490 By using the asterisk to start a new section, I keep the section from appearing in the  
1491 table of contents. If you want your sections to be numbered and to appear in the  
1492 table of contents, remove the asterisk.



---

*Bibliography*

- 1494 [1] O. Perdereau, *Planck 2015 cosmological results*,  
1495 AIP Conf. Proc. **1743** (2016) p. 050014.
- 1496 [2] N. Aghanim et al.,  
1497 *Planck 2016 intermediate results. LI. Features in the cosmic microwave*  
1498 *background temperature power spectrum and shifts in cosmological parameters*  
1499 (2016), arXiv: [1608.02487 \[astro-ph.CO\]](https://arxiv.org/abs/1608.02487).
- 1500 [3] J. S. Schwinger,  
1501 *On Quantum electrodynamics and the magnetic moment of the electron*,  
1502 Phys. Rev. **73** (1948) p. 416.
- 1503 [4] S. Laporta and E. Remiddi,  
1504 *The Analytical value of the electron (g-2) at order alpha\*\*3 in QED*,  
1505 Phys. Lett. **B379** (1996) p. 283, arXiv: [hep-ph/9602417 \[hep-ph\]](https://arxiv.org/abs/hep-ph/9602417).
- 1506 [5] S. Schael et al., *Precision electroweak measurements on the Z resonance*,  
1507 Phys. Rept. **427** (2006) p. 257, arXiv: [hep-ex/0509008 \[hep-ex\]](https://arxiv.org/abs/hep-ex/0509008).
- 1508 [6] S. L. Glashow, *Partial Symmetries of Weak Interactions*,  
1509 Nucl. Phys. **22** (1961) p. 579.
- 1510 [7] S. Weinberg, *A Model of Leptons*, Phys. Rev. Lett. **19** (1967) p. 1264.
- 1511 [8] A. Salam, *Weak and Electromagnetic Interactions*,  
1512 Conf. Proc. **C680519** (1968) p. 367.
- 1513 [9] M. Gell-Mann, *A Schematic Model of Baryons and Mesons*,  
1514 Phys. Lett. **8** (1964) p. 214.
- 1515 [10] G. Zweig, “An SU(3) model for strong interaction symmetry and its  
1516 breaking. Version 2,” *DEVELOPMENTS IN THE QUARK THEORY OF*  
1517 *HADRONS. VOL. 1. 1964 - 1978*, ed. by D. Lichtenberg and S. P. Rosen,  
1518 1964 p. 22,  
1519 URL: <http://inspirehep.net/record/4674/files/cern-th-412.pdf>.

- 1520 [11] S. Weinberg, *Implications of Dynamical Symmetry Breaking*,  
 1521 Phys. Rev. **D13** (1976) p. 974.
- 1522 [12] S. Weinberg, *Implications of Dynamical Symmetry Breaking: An Addendum*,  
 1523 Phys. Rev. **D19** (1979) p. 1277.
- 1524 [13] E. Gildener, *Gauge Symmetry Hierarchies*, Phys. Rev. **D14** (1976) p. 1667.
- 1525 [14] L. Susskind, *Dynamics of Spontaneous Symmetry Breaking in the*  
 1526 *Weinberg-Salam Theory*, Phys. Rev. **D20** (1979) p. 2619.
- 1527 [15] S. P. Martin, “A Supersymmetry Primer,” 1997,  
 1528 eprint: [arXiv:hep-ph/9709356](https://arxiv.org/abs/hep-ph/9709356).
- 1529 [16] V. C. Rubin and W. K. Ford Jr., *Rotation of the Andromeda Nebula from a*  
 1530 *Spectroscopic Survey of Emission Regions*, Astrophys. J. **159** (1970) p. 379.
- 1531 [17] M. S. Roberts and R. N. Whitehurst,  
 1532 “*The rotation curve and geometry of M31 at large galactocentric distances*,  
 1533 Astrophys. J. **201** (1970) p. 327.
- 1534 [18] V. C. Rubin, N. Thonnard, and W. K. Ford Jr.,  
 1535 *Rotational properties of 21 SC galaxies with a large range of luminosities and*  
 1536 *radii, from NGC 4605 /R = 4kpc/ to UGC 2885 /R = 122 kpc/*,  
 1537 Astrophys. J. **238** (1980) p. 471.
- 1538 [19] V. C. Rubin et al., *Rotation velocities of 16 SA galaxies and a comparison of*  
 1539 *Sa, Sb, and SC rotation properties*, Astrophys. J. **289** (1985) p. 81.
- 1540 [20] A. Bosma,  
 1541 *21-cm line studies of spiral galaxies. 2. The distribution and kinematics of*  
 1542 *neutral hydrogen in spiral galaxies of various morphological types.*,  
 1543 Astron. J. **86** (1981) p. 1825.
- 1544 [21] M. Persic, P. Salucci, and F. Stel, *The Universal rotation curve of spiral*  
 1545 *galaxies: 1. The Dark matter connection*,  
 1546 Mon. Not. Roy. Astron. Soc. **281** (1996) p. 27,  
 1547 arXiv: [astro-ph/9506004](https://arxiv.org/abs/astro-ph/9506004) [astro-ph].
- 1548 [22] M. Lisanti, “Lectures on Dark Matter Physics,” 2016,  
 1549 eprint: [arXiv:1603.03797](https://arxiv.org/abs/1603.03797).
- 1550 [23] H. Miyazawa, *Baryon Number Changing Currents*,  
 1551 Prog. Theor. Phys. **36** (1966) p. 1266.

- 1552 [24] J.-L. Gervais and B. Sakita, *Generalizations of dual models*,  
 1553      *Nucl. Phys.* **B34** (1971) p. 477.
- 1554 [25] J.-L. Gervais and B. Sakita,  
 1555      *Field Theory Interpretation of Supergauges in Dual Models*,  
 1556      *Nucl. Phys.* **B34** (1971) p. 632.
- 1557 [26] Yu. A. Golfand and E. P. Likhtman, *Extension of the Algebra of Poincare  
 1558      Group Generators and Violation of  $p$  Invariance*,  
 1559      *JETP Lett.* **13** (1971) p. 323, [*Pisma Zh. Eksp. Teor. Fiz.* **13**, 452 (1971)].
- 1560 [27] A. Neveu and J. H. Schwarz, *Factorizable dual model of pions*,  
 1561      *Nucl. Phys.* **B31** (1971) p. 86.
- 1562 [28] A. Neveu and J. H. Schwarz, *Quark Model of Dual Pions*,  
 1563      *Phys. Rev.* **D4** (1971) p. 1109.
- 1564 [29] D. V. Volkov and V. P. Akulov, *Is the Neutrino a Goldstone Particle?*  
 1565      *Phys. Lett.* **B46** (1973) p. 109.
- 1566 [30] J. Wess and B. Zumino,  
 1567      *A Lagrangian Model Invariant Under Supergauge Transformations*,  
 1568      *Phys. Lett.* **B49** (1974) p. 52.
- 1569 [31] A. Salam and J. A. Strathdee, *Supersymmetry and Nonabelian Gauges*,  
 1570      *Phys. Lett.* **B51** (1974) p. 353.
- 1571 [32] S. Ferrara, J. Wess, and B. Zumino, *Supergauge Multiplets and Superfields*,  
 1572      *Phys. Lett.* **B51** (1974) p. 239.
- 1573 [33] J. Wess and B. Zumino, *Supergauge Transformations in Four-Dimensions*,  
 1574      *Nucl. Phys.* **B70** (1974) p. 39.
- 1575 [34] J. D. Lykken, “Introduction to supersymmetry,” *Fields, strings and duality. Proceedings, Summer School, Theoretical Advanced Study Institute in Elementary Particle Physics, TASI’96, Boulder, USA, June 2-28, 1996*, 1996  
 1576      p. 85, arXiv: [hep-th/9612114](https://arxiv.org/abs/hep-th/9612114) [hep-th],  
 1577      URL: [http://lss.fnal.gov/cgi-bin/find\\_paper.pl?pub-96-445-T](http://lss.fnal.gov/cgi-bin/find_paper.pl?pub-96-445-T).
- 1580 [35] A. Kobakhidze, “Intro to SUSY,” 2016, URL: <https://indico.cern.ch/event/443176/page/5225-pre-susy-programme>.
- 1582 [36] G. R. Farrar and P. Fayet, *Phenomenology of the Production, Decay, and  
 1583      Detection of New Hadronic States Associated with Supersymmetry*,  
 1584      *Phys. Lett.* **B76** (1978) p. 575.

- 1585 [37] ATLAS Collaboration,  
 1586 *Search for the electroweak production of supersymmetric particles in*  
 1587  $\sqrt{s} = 8 \text{ TeV}$  *pp collisions with the ATLAS detector,*  
 1588 *Phys. Rev. D* **93** (2016) p. 052002, arXiv: [1509.07152 \[hep-ex\]](#).
- 1589 [38] ATLAS Collaboration, *Summary of the searches for squarks and gluinos*  
 1590 *using  $\sqrt{s} = 8 \text{ TeV}$  pp collisions with the ATLAS experiment at the LHC,*  
 1591 *JHEP* **10** (2015) p. 054, arXiv: [1507.05525 \[hep-ex\]](#).
- 1592 [39] ATLAS Collaboration, *ATLAS Run 1 searches for direct pair production of*  
 1593 *third-generation squarks at the Large Hadron Collider,*  
 1594 *Eur. Phys. J. C* **75** (2015) p. 510, arXiv: [1506.08616 \[hep-ex\]](#).
- 1595 [40] CMS Collaboration, *Search for supersymmetry with razor variables in pp*  
 1596 *collisions at  $\sqrt{s} = 7 \text{ TeV}$ , Phys. Rev. D* **90** (2014) p. 112001,  
 1597 arXiv: [1405.3961 \[hep-ex\]](#).
- 1598 [41] CMS Collaboration, *Inclusive search for supersymmetry using razor variables*  
 1599 *in pp collisions at  $\sqrt{s} = 7 \text{ TeV}$ , Phys. Rev. Lett.* **111** (2013) p. 081802,  
 1600 arXiv: [1212.6961 \[hep-ex\]](#).
- 1601 [42] CMS Collaboration, *Search for Supersymmetry in pp Collisions at 7 TeV in*  
 1602 *Events with Jets and Missing Transverse Energy,*  
 1603 *Phys. Lett. B* **698** (2011) p. 196, arXiv: [1101.1628 \[hep-ex\]](#).
- 1604 [43] CMS Collaboration, *Search for Supersymmetry at the LHC in Events with*  
 1605 *Jets and Missing Transverse Energy, Phys. Rev. Lett.* **107** (2011) p. 221804,  
 1606 arXiv: [1109.2352 \[hep-ex\]](#).
- 1607 [44] CMS Collaboration, *Search for supersymmetry in hadronic final states using*  
 1608  *$M_{T2}$  in pp collisions at  $\sqrt{s} = 7 \text{ TeV}$ , JHEP* **10** (2012) p. 018,  
 1609 arXiv: [1207.1798 \[hep-ex\]](#).
- 1610 [45] CMS Collaboration, *Searches for supersymmetry using the  $M_{T2}$  variable in*  
 1611 *hadronic events produced in pp collisions at 8 TeV, JHEP* **05** (2015) p. 078,  
 1612 arXiv: [1502.04358 \[hep-ex\]](#).
- 1613 [46] CMS Collaboration, *Search for new physics with the  $M_{T2}$  variable in all-jets*  
 1614 *final states produced in pp collisions at  $\sqrt{s} = 13 \text{ TeV}$  (2016),*  
 1615 arXiv: [1603.04053 \[hep-ex\]](#).
- 1616 [47] ATLAS Collaboration, *Multi-channel search for squarks and gluinos in*  
 1617  $\sqrt{s} = 7 \text{ TeV}$  *pp collisions with the ATLAS detector at the LHC,*  
 1618 *Eur. Phys. J. C* **73** (2013) p. 2362, arXiv: [1212.6149 \[hep-ex\]](#).

- 1619 [48] Y. Grossman, “Introduction to the SM,” 2016, URL: <https://indico.fnal.gov/sessionDisplay.py?sessionId=3&confId=11505#20160811>.
- 1620
- 1621 [49] () .
- 1622 [50] P. W. Higgs, *Broken Symmetries and the Masses of Gauge Bosons*,  
1623 *Phys. Rev. Lett.* **13** (1964) p. 508.
- 1624 [51] ATLAS Collaboration, *Observation of a new particle in the search for the*  
1625 *Standard Model Higgs boson with the ATLAS detector at the LHC*,  
1626 *Phys. Lett. B* **716** (2012) p. 1, arXiv: [1207.7214](https://arxiv.org/abs/1207.7214) [hep-ex].
- 1627 [52] CMS Collaboration, *Observation of a new boson at a mass of 125 GeV with*  
1628 *the CMS experiment at the LHC*, *Phys. Lett. B* **716** (2012) p. 30,  
1629 arXiv: [1207.7235](https://arxiv.org/abs/1207.7235) [hep-ex].
- 1630 [53] A. Chodos et al., *A New Extended Model of Hadrons*,  
1631 *Phys. Rev. D* **9** (1974) p. 3471.
- 1632 [54] A. Chodos et al., *Baryon Structure in the Bag Theory*,  
1633 *Phys. Rev. D* **10** (1974) p. 2599.
- 1634 [55] J. C. Collins, D. E. Soper, and G. F. Sterman,  
1635 *Factorization of Hard Processes in QCD*,  
1636 *Adv. Ser. Direct. High Energy Phys.* **5** (1989) p. 1,  
1637 arXiv: [hep-ph/0409313](https://arxiv.org/abs/hep-ph/0409313) [hep-ph].
- 1638 [56] K. A. Olive et al., *Review of Particle Physics*,  
1639 *Chin. Phys. C* **38** (2014) p. 090001.
- 1640 [57] N. Cabibbo, *Unitary Symmetry and Leptonic Decays*,  
1641 *Phys. Rev. Lett.* **10** (1963) p. 531, [,648(1963)].
- 1642 [58] M. Kobayashi and T. Maskawa,  
1643 *CP Violation in the Renormalizable Theory of Weak Interaction*,  
1644 *Prog. Theor. Phys.* **49** (1973) p. 652.
- 1645 [59] W. F. L. Hollik, *Radiative Corrections in the Standard Model and their Role*  
1646 *for Precision Tests of the Electroweak Theory*,  
1647 *Fortsch. Phys.* **38** (1990) p. 165.
- 1648 [60] D. Yu. Bardin et al.,  
1649 *ELECTROWEAK RADIATIVE CORRECTIONS TO DEEP INELASTIC*  
1650 *SCATTERING AT HERA! CHARGED CURRENT SCATTERING*,  
1651 *Z. Phys. C* **44** (1989) p. 149.

- 1652 [61] D. C. Kennedy et al.,  
 1653 *Electroweak Cross-Sections and Asymmetries at the Z0*,  
 1654 *Nucl. Phys.* **B321** (1989) p. 83.
- 1655 [62] A. Sirlin, *Radiative Corrections in the SU(2)-L x U(1) Theory: A Simple*  
 1656 *Renormalization Framework*, *Phys. Rev.* **D22** (1980) p. 971.
- 1657 [63] S. Fanchiotti, B. A. Kniehl, and A. Sirlin,  
 1658 *Incorporation of QCD effects in basic corrections of the electroweak theory*,  
 1659 *Phys. Rev.* **D48** (1993) p. 307, arXiv: [hep-ph/9212285 \[hep-ph\]](#).
- 1660 [64] C. Quigg, “Cosmic Neutrinos,” *Proceedings, 35th SLAC Summer Institute on*  
 1661 *Particle Physics: Dark matter: From the cosmos to the Laboratory (SSI*  
 1662 *2007): Menlo Park, California, July 30- August 10, 2007*, 2008,  
 1663 arXiv: [0802.0013 \[hep-ph\]](#),  
 1664 URL: [http://lss.fnal.gov/cgi-bin/find\\_paper.pl?conf=07-417](http://lss.fnal.gov/cgi-bin/find_paper.pl?conf=07-417).
- 1665 [65] S. R. Coleman and J. Mandula, *All Possible Symmetries of the S Matrix*,  
 1666 *Phys. Rev.* **159** (1967) p. 1251.
- 1667 [66] R. Haag, J. T. Lopuszanski, and M. Sohnius,  
 1668 *All Possible Generators of Supersymmetries of the s Matrix*,  
 1669 *Nucl. Phys.* **B88** (1975) p. 257.
- 1670 [67] A. Salam and J. A. Strathdee, *On Superfields and Fermi-Bose Symmetry*,  
 1671 *Phys. Rev.* **D11** (1975) p. 1521.
- 1672 [68] S. Dimopoulos and H. Georgi, *Softly Broken Supersymmetry and SU(5)*,  
 1673 *Nucl. Phys.* **B193** (1981) p. 150.
- 1674 [69] S. Dimopoulos, S. Raby, and F. Wilczek,  
 1675 *Supersymmetry and the Scale of Unification*, *Phys. Rev.* **D24** (1981) p. 1681.
- 1676 [70] L. E. Ibanez and G. G. Ross,  
 1677 *Low-Energy Predictions in Supersymmetric Grand Unified Theories*,  
 1678 *Phys. Lett.* **B105** (1981) p. 439.
- 1679 [71] W. J. Marciano and G. Senjanovic,  
 1680 *Predictions of Supersymmetric Grand Unified Theories*,  
 1681 *Phys. Rev.* **D25** (1982) p. 3092.
- 1682 [72] L. Girardello and M. T. Grisaru, *Soft Breaking of Supersymmetry*,  
 1683 *Nucl. Phys.* **B194** (1982) p. 65.

- 1684 [73] D. J. H. Chung et al.,  
 1685 *The Soft supersymmetry breaking Lagrangian: Theory and applications*,  
 1686 Phys. Rept. **407** (2005) p. 1, arXiv: [hep-ph/0312378 \[hep-ph\]](#).
- 1687 [74] J. Hisano et al., *Lepton flavor violation in the supersymmetric standard*  
 1688 *model with seesaw induced neutrino masses*, Phys. Lett. **B357** (1995) p. 579,  
 1689 arXiv: [hep-ph/9501407 \[hep-ph\]](#).
- 1690 [75] F. Gabbiani et al., *A Complete analysis of FCNC and CP constraints in*  
 1691 *general SUSY extensions of the standard model*,  
 1692 Nucl. Phys. **B477** (1996) p. 321, arXiv: [hep-ph/9604387 \[hep-ph\]](#).
- 1693 [76] F. Gabbiani and A. Masiero,  
 1694 *FCNC in Generalized Supersymmetric Theories*,  
 1695 Nucl. Phys. **B322** (1989) p. 235.
- 1696 [77] J. S. Hagelin, S. Kelley, and T. Tanaka, *Supersymmetric flavor changing*  
 1697 *neutral currents: Exact amplitudes and phenomenological analysis*,  
 1698 Nucl. Phys. **B415** (1994) p. 293.
- 1699 [78] J. S. Hagelin, S. Kelley, and V. Ziegler, *Using gauge coupling unification and*  
 1700 *proton decay to test minimal supersymmetric SU(5)*,  
 1701 Phys. Lett. **B342** (1995) p. 145, arXiv: [hep-ph/9406366 \[hep-ph\]](#).
- 1702 [79] D. Choudhury et al.,  
 1703 *Constraints on nonuniversal soft terms from flavor changing neutral currents*,  
 1704 Phys. Lett. **B342** (1995) p. 180, arXiv: [hep-ph/9408275 \[hep-ph\]](#).
- 1705 [80] R. Barbieri and L. J. Hall, *Signals for supersymmetric unification*,  
 1706 Phys. Lett. **B338** (1994) p. 212, arXiv: [hep-ph/9408406 \[hep-ph\]](#).
- 1707 [81] B. de Carlos, J. A. Casas, and J. M. Moreno,  
 1708 *Constraints on supersymmetric theories from mu —> e gamma*,  
 1709 Phys. Rev. **D53** (1996) p. 6398, arXiv: [hep-ph/9507377 \[hep-ph\]](#).
- 1710 [82] J. A. Casas and S. Dimopoulos,  
 1711 *Stability bounds on flavor violating trilinear soft terms in the MSSM*,  
 1712 Phys. Lett. **B387** (1996) p. 107, arXiv: [hep-ph/9606237 \[hep-ph\]](#).
- 1713 [83] C. Borschensky et al., *Squark and gluino production cross sections in pp*  
 1714 *collisions at  $\sqrt{s} = 13, 14, 33$  and  $100$  TeV*,  
 1715 Eur. Phys. J. **C74** (2014) p. 3174, arXiv: [1407.5066 \[hep-ph\]](#).
- 1716 [84] M. Klasen, M. Pohl, and G. Sigl, *Indirect and direct search for dark matter*,  
 1717 Prog. Part. Nucl. Phys. **85** (2015) p. 1, arXiv: [1507.03800 \[hep-ph\]](#).

- 1718 [85] L. Evans and P. Bryant, *LHC Machine*, JINST **3** (2008) S08001.
- 1719 [86] V. Shiltsev, “Accelerator Physics and Technology,” 2016,  
1720 URL: [https://indico.fnal.gov/sessionDisplay.py?sessionId=3&](https://indico.fnal.gov/sessionDisplay.py?sessionId=3&confId=11505#20160811)  
1721 [confId=11505#20160811](#).
- 1722 [87] *LEP design report*, Copies shelved as reports in LEP, PS and SPS libraries,  
1723 Geneva: CERN, 1984, URL: <https://cds.cern.ch/record/102083>.
- 1724 [88] ATLAS Collaboration,  
1725 *The ATLAS Experiment at the CERN Large Hadron Collider*,  
1726 JINST **3** (2008) S08003.
- 1727 [89] ATLAS Collaboration, *2015 start-up trigger menu and initial performance*  
1728 *assessment of the ATLAS trigger using Run-2 data*,  
1729 ATL-DAQ-PUB-2016-001, 2016,  
1730 URL: <https://cds.cern.ch/record/2136007/>.
- 1731 [90] ATLAS Collaboration, *Performance of the ATLAS Inner Detector Track and*  
1732 *Vertex Reconstruction in High Pile-Up LHC Environment*,  
1733 ATLAS-CONF-2012-042, 2012,  
1734 URL: <https://cds.cern.ch/record/1435196>.
- 1735 [91] ATLAS Collaboration, *Early Inner Detector Tracking Performance in the*  
1736 *2015 Data at  $\sqrt{s} = 13 \text{ TeV}$* , ATL-PHYS-PUB-2015-051, 2015,  
1737 URL: <https://cds.cern.ch/record/2110140>.
- 1738 [92] K Hamano, A Morley, and A Salzburger,  
1739 “Track Reconstruction Performance and Efficiency Estimation using different  
1740 ID geometry samples,” tech. rep. ATL-COM-PHYS-2012-1541,  
1741 plots for a poster at HCP: CERN, 2012,  
1742 URL: <https://cds.cern.ch/record/1489674>.
- 1743 [93] ATLAS Collaboration,  
1744 *Electron reconstruction and identification efficiency measurements with the*  
1745 *ATLAS detector using the 2011 LHC proton–proton collision data*,  
1746 Eur. Phys. J. C **74** (2014) p. 2941, arXiv: [1404.2240 \[hep-ex\]](https://arxiv.org/abs/1404.2240).
- 1747 [94] ATLAS Collaboration, *Topological cell clustering in the ATLAS calorimeters*  
1748 *and its performance in LHC Run 1* (2016), arXiv: [1603.02934 \[hep-ex\]](https://arxiv.org/abs/1603.02934).
- 1749 [95] ATLAS Collaboration, *Jet energy resolution in proton–proton collisions at*  
1750  *$\sqrt{s} = 7 \text{ TeV}$  recorded in 2010 with the ATLAS detector*,  
1751 Eur. Phys. J. C **73** (2013) p. 2306, arXiv: [1210.6210 \[hep-ex\]](https://arxiv.org/abs/1210.6210).

- 1752 [96] M. Aaboud et al., *Measurement of the photon identification efficiencies with*  
 1753 *the ATLAS detector using LHC Run-1 data* (2016),  
 1754 arXiv: [1606.01813 \[hep-ex\]](https://arxiv.org/abs/1606.01813).
- 1755 [97] ATLAS Collaboration, *Electron and photon energy calibration with the*  
 1756 *ATLAS detector using LHC Run 1 data*, Eur. Phys. J. C **74** (2014) p. 3071,  
 1757 arXiv: [1407.5063 \[hep-ex\]](https://arxiv.org/abs/1407.5063).
- 1758 [98] “Electron and photon energy calibration with the ATLAS detector using  
 1759 data collected in 2015 at  $\sqrt{s} = 13$  TeV,”  
 1760 tech. rep. ATL-PHYS-PUB-2016-015, CERN, 2016,  
 1761 URL: <https://cds.cern.ch/record/2203514>.
- 1762 [99] ATLAS Collaboration, *Muon reconstruction performance of the ATLAS*  
 1763 *detector in proton–proton collision data at  $\sqrt{s} = 13$  TeV* (2016),  
 1764 arXiv: [1603.05598 \[hep-ex\]](https://arxiv.org/abs/1603.05598).
- 1765 [100] ATLAS Collaboration, *Jet energy measurement with the ATLAS detector in*  
 1766 *proton–proton collisions at  $\sqrt{s} = 7$  TeV*, Eur. Phys. J. C **73** (2013) p. 2304,  
 1767 arXiv: [1112.6426 \[hep-ex\]](https://arxiv.org/abs/1112.6426).
- 1768 [101] ATLAS Collaboration,  
 1769 *Jet energy measurement and its systematic uncertainty in proton–proton*  
 1770 *collisions at  $\sqrt{s} = 7$  TeV with the ATLAS detector*,  
 1771 Eur. Phys. J. C **75** (2015) p. 17, arXiv: [1406.0076 \[hep-ex\]](https://arxiv.org/abs/1406.0076).
- 1772 [102] S. D. Ellis and D. E. Soper,  
 1773 *Successive combination jet algorithm for hadron collisions*,  
 1774 Phys. Rev. **D48** (1993) p. 3160, arXiv: [hep-ph/9305266 \[hep-ph\]](https://arxiv.org/abs/hep-ph/9305266).
- 1775 [103] M. Cacciari and G. P. Salam, *Dispelling the  $N^3$  myth for the  $k_t$  jet-finder*,  
 1776 Phys. Lett. **B641** (2006) p. 57, arXiv: [hep-ph/0512210 \[hep-ph\]](https://arxiv.org/abs/hep-ph/0512210).
- 1777 [104] M. Cacciari, G. P. Salam, and G. Soyez,  
 1778 *The Anti- $k(t)$  jet clustering algorithm*, JHEP **04** (2008) p. 063,  
 1779 arXiv: [0802.1189 \[hep-ph\]](https://arxiv.org/abs/0802.1189).
- 1780 [105] *Particle-Flow Event Reconstruction in CMS and Performance for Jets, Taus,*  
 1781 *and MET* (2009).
- 1782 [106] ATLAS Collaboration,  
 1783 *Tagging and suppression of pileup jets with the ATLAS detector*,  
 1784 ATLAS-CONF-2014-018, 2014,  
 1785 URL: <https://cds.cern.ch/record/1700870>.

- 1786 [107] M. Cacciari, G. P. Salam, and G. Soyez, *The Catchment Area of Jets*,  
 1787 JHEP **04** (2008) p. 005, arXiv: [0802.1188](https://arxiv.org/abs/0802.1188) [hep-ph].
- 1788 [108] “Optimisation of the ATLAS  $b$ -tagging performance for the 2016 LHC Run,”  
 1789 tech. rep. ATL-PHYS-PUB-2016-012, CERN, 2016,  
 1790 URL: <https://cds.cern.ch/record/2160731>.
- 1791 [109] G. Aad et al., *Performance of algorithms that reconstruct missing transverse*  
 1792 *momentum in  $\sqrt{s} = 8$  TeV proton-proton collisions in the ATLAS detector*  
 1793 (2016), arXiv: [1609.09324](https://arxiv.org/abs/1609.09324) [hep-ex].
- 1794 [110] ATLAS Collaboration,  
 1795 *Prospects for Supersymmetry discovery based on inclusive searches at a*  
 1796 *7 TeV centre-of-mass energy with the ATLAS detector*,  
 1797 ATL-PHYS-PUB-2010-010, 2010,  
 1798 URL: <https://cds.cern.ch/record/1278474>.
- 1799 [111] ATLAS Collaboration,  
 1800 *Expected sensitivity studies for gluino and squark searches using the early*  
 1801 *LHC 13 TeV Run-2 dataset with the ATLAS experiment*,  
 1802 ATL-PHYS-PUB-2015-005, 2015, URL:  
 1803 [https://atlas.web.cern.ch/Atlas/GROUPS/PHYSICS/PUBNOTES/ATL-](https://atlas.web.cern.ch/Atlas/GROUPS/PHYSICS/PUBNOTES/ATL-PHYS-PUB-2015-005)  
 1804 [PHYS-PUB-2015-005](https://atlas.web.cern.ch/Atlas/GROUPS/PHYSICS/PUBNOTES/ATL-PHYS-PUB-2015-005).
- 1805 [112] ATLAS Collaboration, *Expected performance of missing transverse*  
 1806 *momentum reconstruction for the ATLAS detector at  $\sqrt{s} = 13$  TeV*,  
 1807 ATL-PHYS-PUB-2015-023, 2015,  
 1808 URL: <https://cds.cern.ch/record/2037700>.
- 1809 [113] ATLAS Collaboration,  
 1810 *Performance of missing transverse momentum reconstruction with the*  
 1811 *ATLAS detector in the first proton–proton collisions at  $\sqrt{s} = 13$  TeV*,  
 1812 ATL-PHYS-PUB-2015-027, 2015,  
 1813 URL: <https://cds.cern.ch/record/2037904>.
- 1814 [114] CMS Collaboration, *Search for supersymmetry using razor variables in*  
 1815 *events with  $b$ -tagged jets in  $pp$  collisions at  $\sqrt{s} = 8$  TeV*,  
 1816 Phys. Rev. D **91** (2015) p. 052018, arXiv: [1502.00300](https://arxiv.org/abs/1502.00300) [hep-ex].

---

1817

## *The Standard Model*

1818 In this appendix, we provide a brief overview of the basic ingredients involved in  
1819 construction of the Standard Model Lagrangian : quantum field theory, symmetries,  
1820 and symmetry breaking.

## **1821 Quantum Field Theory**

1822 **TODO: cite Yuval's lectures and notes somehow**

1823 In this section, we provide a brief overview of the necessary concepts from  
1824 Quantum Field Theory (QFT).

1825 In modern physics, the laws of nature are described by the “action”  $S$ , with the  
1826 imposition of the principle of minimum action. **TODO: cite** The action is the integral  
1827 over the spacetime coordinates of the “Lagrangian density”  $\mathcal{L}$ , or Lagrangian for  
1828 short. The Lagrangian is a function of “fields”; general fields will be called  $\phi(x^\mu)$ ,  
1829 where the indices  $\mu$  run over the space-time coordinates. We can then write the action  
1830  $S$  as

$$S = \int d^4x \mathcal{L}[\phi_i(x^\mu), \partial_\mu \phi_i(x^\mu)] \quad (10.1)$$

1831 where we have an additional summation over  $i$  (of the different fields). Generally,  
1832 we impose the following constraints on the Lagrangian :

1833 1. Translational invariance - The Lagrangian is only a function of the fields  $\phi$  and  
1834 their derivatives  $\partial_\mu \phi$

1835     2. Locality - The Lagrangian is only a function of one point  $x_\mu$  in spacetime.

1836     3. Reality condition - The Lagrangian is real to conserve probability.

1837     4. Lorentz invariance - The Lagrangian is invariant under the Poincarégroup of  
1838       spacetime.

1839     5. Analyticity - The Lagrangian is an analytical function of the fields; this is to  
1840       allow the use of perturbation theory.

1841     6. Invariance and Naturalness - The Lagrangian is invariant under some internal  
1842       symmetry groups; in fact, the Lagrangian will have *all* terms allowed by the  
1843       imposed symmetry groups. **TODO: maybe add in ref here**

1844     7. Renormalizability - The Lagrangian will be renormalizable - in practice, this  
1845       means there will not be terms with more than power 4 in the fields.

1846     The key item from the point of view of this thesis is that of “Invariance and  
1847       Natural”. We impose a set of “symmetries” and then our Lagrangian is the most  
1848       general which is allowed by those symmetries.

## 1849 **Symmetries**

1850 Symmetries can be seen as the fundamental guiding concept of modern physics.  
1851 Symmetries are described by “groups”. **TODO: cite?**. To illustrate the importance  
1852 of symmetries and their mathematical description, groups, we start here with two of  
1853 the simplest and most useful examples :  $\mathbb{Z}_2$  and  $U(1)$ .

### 1854 **$\mathbb{Z}_2$ symmetry**

1855  $\mathbb{Z}_2$ symmetry is the simplest example of a “discrete” symmetry. Consider the most  
1856 general Lagrangian of a single real scalar field  $\phi(x_\mu)$

$$\mathcal{L}_\phi = \frac{1}{2}\partial_\mu\phi\partial^\mu\phi - \frac{m^2}{2}\phi^2 - \frac{\mu}{2\sqrt{2}}\phi^3 - \lambda\phi^4 \quad (10.2)$$

Now we *impose* the symmetry

$$\mathcal{L}(\phi) = \mathcal{L}(-\phi) \quad (10.3)$$

1857 This has the effect of restricting the allowed terms of the Lagrangian. In particular,  
 1858 we can see the term  $\phi^3 \rightarrow -\phi^3$  under the symmetry transformation, and thus must  
 1859 be disallowed by this symmetry. This means under the imposition of this particular  
 1860 symmetry, our Lagrangian should be rewritten as

$$\mathcal{L}_\phi = \frac{1}{2}\partial_\mu\phi\partial^\mu\phi - \frac{m^2}{2}\phi^2 - \lambda\phi^4 \quad (10.4)$$

1861 The effect of this symmetry is that the total number of  $\phi$  particles can only change  
 1862 by even numbers, since the only interaction term  $\lambda\phi^4$  is an even power of the field.  
 1863 This symmetry is often imposed in supersymmetric theories, as we will see in Chapter  
 1864 3.

## 1865 **$U(1)$ symmetry**

1866  $U(1)$  is the simplest example of a continuous (or *Lie*) group. Now consider a theory  
 1867 with a single complex scalar field  $\phi = \text{Re } \phi + i \text{Im } \phi$

$$\mathcal{L}_\phi = \delta_{i,j} \frac{1}{2}\partial_\mu\phi_i\partial^\mu\phi_j - \frac{m^2}{2}\phi_i\phi_j - \frac{\mu}{2\sqrt{2}}\phi_i\phi_j\phi_k\phi_l - \lambda\phi_i\phi_j\phi_k\phi_l \quad (10.5)$$

1868 where  $i, j, k, l = \text{Re}, \text{Im}$ . In this case, we impose the following  $U(1)$  symmetry  
 1869 :  $\phi \rightarrow e^{i\theta}, \phi^* \rightarrow e^{-i\theta}$ . We see immediately that this again disallows the third-order  
 1870 terms, and we can write a theory of a complex scalar field with  $U(1)$  symmetry as

$$\mathcal{L}_\phi = \partial_\mu\phi\partial^\mu\phi^* - \frac{m^2}{2}\phi\phi^* - \lambda(\phi\phi^*)^2 \quad (10.6)$$

1871 **Local symmetries**

1872 The two examples considered above are “global” symmetries in the sense that the  
1873 symmetry transformation does not depends on the spacetime coordinate  $x_\mu$ . We know  
1874 look at local symmetries; in this case, for example with a local  $U(1)$  symmetry, the  
1875 transformation has the form  $\phi(x_\mu) \rightarrow e^{i\theta(x_\mu)}\phi(x_\mu)$ . These symmetries are also known  
1876 as “gauge” symmetries; all symmetries of the Standard Model are gauge symmetries.

There are wide-ranging consequences to the imposition of local symmetries. To begin, we note that the derivative terms of the Lagrangian 10.2 are *not* invariant under a local symmetry transformation

$$\partial_\mu \phi(x_\mu) \rightarrow \partial_\mu(e^{i\theta(x_\mu)}\phi(x_\mu)) = (1 + i\theta(x_\mu))e^{i\theta(x_\mu)}\phi(x_\mu) \quad (10.7)$$

1877 **TODO: GET THIS RIGHT**

1878 This leads us to note that the kinetic terms of the Lagrangian are also not invariant  
1879 under a gauge symmetry. This would lead to a model with no dynamics, which is  
1880 clearly unsatisfactory.

1881 Let us take inspiration from the case of global symmetries. We need to define a  
1882 so-called “covariant” derivative  $D^\mu$  such that

$$D^\mu \phi \rightarrow e^{iq\theta(x^\mu)D^\mu}\phi \quad (10.8)$$

$$D^\mu \phi^* \rightarrow e^{-iq\theta(x^\mu)D^\mu}\phi^* \quad (10.9)$$

$$(10.10)$$

1883 Since  $\phi$  and  $\phi^*$  transforms with the opposite phase, this will lead the invariance  
1884 of the Lagrangian under our local gauge transformation. This  $D^\mu$  is of the following  
1885 form

$$D^\mu = \partial_\mu - igqA^\mu \quad (10.11)$$

1886 where  $A^\mu$  is a vector field we introduce with the transformation law

$$A^\mu \rightarrow A^\mu - \frac{1}{g} \partial_\mu \theta \quad (10.12)$$

1887 and  $g$  is the coupling constant associated to vector field. This vector field  $A^\mu$  is  
1888 also known as a “gauge” field.

1889 Since we need to add all allowed terms to the Lagrangian, we define

$$F^{\mu\nu} = A^\mu A^\nu - A^\nu A^\mu \quad (10.13)$$

1890 and then we must also add the kinetic term :

$$\mathcal{L}_{\text{gauge}} = -\frac{1}{4} F^{\mu\nu} F_{\mu\nu} \quad (10.14)$$

1891 The most general renormalizable Lagrangian with fermion and scalar fields can  
1892 be written in the following form

$$\mathcal{L} = \mathcal{L}_{\text{kin}} + \mathcal{L}_\phi + \mathcal{L}_\psi + \mathcal{L}_{\text{Yukawa}} \quad (10.15)$$

## 1893 Symmetry breaking and the Higgs mechanism

1894 Here we view some examples of symmetry breaking. We investigate breaking of a  
1895 global  $U(1)$  symmetry and a local  $U(1)$  symmetry. The SM will break the electroweak  
1896 symmetry  $SU(2)xU(1)$ , and in Chapter 3 we will see how supersymmetry must also  
1897 be broken.

1898 There are two ideas of symmetry breaking

- 1899 • Explicit symmetry breaking by a small parameter - in this case, we have a small  
1900 parameter which breaks an “approximate” symmetry of our Lagrangian. An  
1901 example would be the theory of the single scalar field 10.2, when  $\mu \ll m^2$  and

1902       $\mu \ll \lambda$ . In this case, we can often ignore the small term when considering  
 1903      low-energy processes.

1904      • Spontaneous symmetry breaking (SSB) - spontaneous symmetry breaking  
 1905      occurs when the Lagrangian is symmetric with respect to a given symmetry  
 1906      transformation, but the ground state of the theory is *not* symmetric with respect  
 1907      to that transformation. This can have some fascinating consequences, as we  
 1908      will see in the following examples

1909      Symmetry breaking a

1910      **U(1) global symmetry breaking**

Consider the theory of a complex scalar field under the  $U(1)$  symmetry, or the transformation

$$\phi \rightarrow e^{i\theta} \phi \quad (10.16)$$

The Lagrangian for this theory is

$$\mathcal{L} = \partial^\mu \phi^\dagger \partial_\mu \phi + \frac{\mu^2}{2} \phi^\dagger \phi + \frac{\lambda}{4} (\phi^\dagger \phi)^2 \quad (10.17)$$

Let us write this theory in terms of two scalar fields,  $h$  and  $\xi$  :  $\phi = (h + i\xi)/\sqrt{2}$ .

The Lagrangian can then be written as

$$\mathcal{L} = \partial^\mu h \partial_\mu h + \partial^\mu \xi d\mu \xi - \frac{\mu^2}{2} (h^2 + \xi^2) - \frac{\lambda}{4} (h^2 + \xi^2)^2 \quad (10.18)$$

First, note that the theory is only stable when  $\lambda > 0$ . To understand the effect of SSB, we now enforce that  $\mu^2 < 0$ , and define  $v^2 = -\mu^2/\lambda$ . We can then write the scalar potential of this theory as :

$$V(\phi) = \lambda(\phi^\dagger \phi - v^2/2)^2 \quad (10.19)$$

Minimizing this equation with respect to  $\phi$ , we can see that the “vacuum expectation value” of the theory is

$$2 < \phi^\dagger \phi > = < h^2 + \xi^2 > = v^2 \quad (10.20)$$

1911        We now reach the “breaking” point of this procedure. In the  $(h, \xi)$  plane, the  
 1912   minima form a circle of radius  $v$ . We are free to choose any of these minima to expand  
 1913   our Lagrangian around; the physics is not affected by this choice. For convenience,  
 1914   choose  $\langle h \rangle = v, \langle \xi^2 \rangle = 0$ .

Now, let us define  $h' = h - v, \xi' = \xi$  with VEVs  $\langle h' \rangle = 0, \langle \xi' \rangle = 0$ . We can  
 then write our spontaneously broken Lagrangian in the form

$$\mathcal{L} = \frac{1}{2}\partial_\mu h'\partial^\mu h' + \frac{1}{2}\partial_\mu \xi'\partial^\mu \xi' - \lambda v^2 h'^2 - \lambda v h'(h'^2 + \xi'^2) - \lambda(h'^2 + \xi'^2)^2 \quad (10.21)$$